Abstract

"Magic Angle Sample Spinning NMR on Biomembranes"

Clemens Glaubitz, St Cross College

D.Phil Thesis, Trinity 1998

In this study, the application of ^{1}H-, ^{2}H- and ^{13}C-Nuclear Magnetic Resonance Spectroscopy to macroscopically oriented lipid membranes, which are subject to rotation about the magic angle in the magnetic field, is demonstrated as a new general method to obtain structural and orientational information for membrane proteins at high spectral resolution and sensitivity.

MAS on oriented samples (MAOSS) is performed, by placing uniformly aligned lipid membranes on solid glass disks placed in standard MAS rotors with the membrane normal parallel to the rotor axis.

In this experimental setup, highly anisotropically mobile membrane components, such as lipids, would actually reorient rapidly about the magic angle. This arrangement causes the homonuclear dipolar coupling between the protons to collapse. Furthermore, slow sample rotation about the magic angle averages remaining residual dipolar coupling, which arises from a certain macroscopic disorder in the sample. Highly resolved proton spectra of oriented DMPC were obtained in that way and the potential for applications to peptides and proteins is discussed.

In contrast, the chemical shift anisotropy of nuclei such as ^{13}C or ^{15}N or the anisotropy of the quadrupole coupling of ^{2}H, can be utilized for studying immobile or motionally restricted membrane components, such as peptides or proteins. Wideline spectra, which are dominated by these interactions decay into a set of spinning sidebands under MAS conditions. Each sideband intensity is a function of the principal elements and the orientation of the interaction tensor. The orientational information is lost in powder samples but can be extracted from sidebands in MAOSS experiments.

Here, the first ^{2}H-MAOSS experiments are shown on oriented bacteriorhodopsin (purple membrane) C(^{2}H)$_3$-labelled at position C_{18} in the retinal. Data analysis, error estimation and angle determination of the C_{18}-C(^{2}H)$_3$ bond vector with respect to the membrane normal from ^{2}H spinning sidebands are discussed.

^{13}C-MAS spectroscopy has been applied to M13 coat protein in DMPC bilayers selectively labelled with two ^{13}C spin pairs in the hydrophobic domain in residues Val-29, Val-30 and Val-29, Val-31. Rotational resonance

experiments on unoriented samples did provide distance constraints, which revealed an α-helical conformation. MAOSS experiments on the same, but oriented samples allowed the measurement of the tilt of the transmembrane helix from the carbonyl sideband pattern.

A simple but efficient way to probe the membrane surface and to control, whether labelled sites in membrane proteins are close to the membrane interface or buried in the hydrophobic core of the lipid bilayer, is demonstrated by observing the effects Lanthanide ions would have on the ^{13}C spectra of DMPC and M13 coat protein reconstituted in DMPC.

Algorithms and simulation software for calculating MAOSS spectra and for analysing rotational resonance magnetisation exchange trajectories are presented.

Acknowledgements

I would like to thank my supervisor Tony Watts for his stimulating and constant support over the past years and for allowing me a vast degree of freedom in my research, including the numerous opportunities to travel and to make contacts within the scientific community.

I am especially grateful to Gerhard Gröbner with whom I enjoyed a stimulating long term cooperation and many brainstorming sessions, as well as to Paul Spooner for his great reservoir of experience and also for keeping the spectrometer "alive".

The supply of bacteriorhodopsin and retinal by James Mason and Ian Burnett was invaluable

I appreciate the rotational resonance work with Phil Williamson on actylcholine and NMR discussions together with Boyan Bonev and David Middleton.

Liz Mitchell is especially acknowledged for her rather efficient administrative management and Peter Fisher for lipid synthesis and amino acid protection.

I am also grateful to Jonathan Sharples and Milos Jovicic for their work during their partII projects.

Finally I like to thank all the current and former members of our group, especially Vikki Addy, Teresa Pinheiro, Clare Whiteway, Zareen Ahmed, Jude Watts, Andy Taylor, Greg Choi, Jonathan Boulter, Anne Ulrich and all the others I met during my time in this lab for all the dynamic exchange of ideas, different views and opinions.

I am grateful, that I had the opportunity to spend some weeks in Malcolm Levitt's laboratory in Stockolm in the initial phase of my D.Phil. research, which was important for the way my work was done. Many thanks also to Xiaolong Feng for the cooperation on some aspects on rotational resonance.

Markus Hemminga, Wageningen, The Netherlands, is acknowledged for initial help with the M13 work.

I am grateful to Jose Areas, Sao Paulo, Brasil for the rather interesting time in his laboratory.

This work was supported by BBSRC and the EU.

St Cross College, Oxford is acknowledged for supporting me with a Unilever Scholarship.

The Rhodes Trust, Oxford is acknowledged for providing me with a C. Rhodes scholarship and travel grants.

Finally, I would like to thank my family and my friends for their constant support over the past years.

Contents

List of Figures

Frequently used Symbols

PAS	principal axis system
MF	molecular reference frame
DF	sample fixed reference frame
RF	rotor fixed reference frame
LF	laboratory frame
Z_P	z-axis of PAS
Z_M	z-axis of MF
Z_R	z-axis of RF
$\Omega_{PL}(\alpha_{PL}, \beta_{PL}, \gamma_{PL})$	Euler angles for rotating PAS into LF
$\Omega_{DL}(\alpha_{DL}, \beta_{DL}, \gamma_{DL})$	Euler angles for rotating DF into LF
$\Omega_{RL}(\omega_r t, \theta, \psi)$	Euler angles for rotating RF into LF
	time dependent under MAS
ω_r	sample spinning rate
$\Omega_{PR}(\alpha_{PR}, \beta_{PR}, \gamma_{PR})$	Euler angles for rotating PAS into RF
$\Omega_{MR}(\alpha_{MR}, \beta_{MR}, \gamma_{MR})$	Euler angles for rotating MF into RF
$\Omega_{DR}(\alpha_{DR}, \beta_{DR}, \gamma_{DR})$	Euler angles for rotating DF into RF
$\Omega_{PM}(\alpha_{PM}, \beta_{PM}, \gamma_{PM})$	Euler angles for rotating PAS into MF
$\Omega_{MD}(\alpha_{MD}, \beta_{MD}, \gamma_{MD})$	Euler angles for rotating MF into DF
$\Delta\beta$	mosaic spread
σ_{iso}	isotropic chemical shift
δ	chemical shift anisotropy
η	asymmetry parameter
$\sigma_{11}, \sigma_{22}, \sigma_{33}$	main elements of interaction tensor in PAS
MAS	magic angle sample spinning
MAOSS	MAS on oriented samples
bR	bacteriorhodopsin
DMPC	dimyristoyl-sn-glycero-3-phosphorylcholine
M13	M13 coat protein

Chapter 1

Introduction

1.1 Biomembranes

The formation of molecular biology in the middle of this century has triggered a scientific revolution which has completely changed our understanding of living systems. Establishing DNA as the genetic information storage material by Hershey and Chase and proposing a molecular double helix model by Watson and Crick has focused many research efforts towards studies of information/structure and structure/function relationships. This last aspect especially applies to cell or membrane biophysics as a primary research aim. In forming a membrane, nature has exploited entropy to enable the separation of living entities from the outside world, while establishing a selective material exchange between both environments. Biomembranes enable the modular design of cells, which was an essential evolutionary step.

The membranes of living cells have a highly complex molecular architecture, and consist of three layers. The glycocalix, which covers the outside, is a 10nm thick macromolecular layer of oligosaccharides. The intracellular side of a membrane extends into the cytoskeleton, a two-dimensional macromolecular network. In the middle, a liquid crystalline lipid/protein layer, as shown in Fig.1.1 for an eukaryotic cell membrane carries a variety of integral or peripheral proteins. In 1972, Singer and Nicolson suggested the "fluid-mosaic-model" [1], which provides the basis of our current understanding of biomembrane structures. The disposition and orientation of proteins in the membrane depends on their hydrophobic and hydrophilic regions (Fig.1.1). Many of them carry the oligosaccharide groups of the glycocalix and their N-terminal projects into the aqueous surrounding, while their C-terminal is usually intracellulary located. The lipids in the membrane form a two-dimensional, amphiphilic liquid crystalline environment which serves as a matrix for the proteins. Both sides of the bilayer are usually different in lipid composition and protein content, giving an asymmetric structure membranes [2].

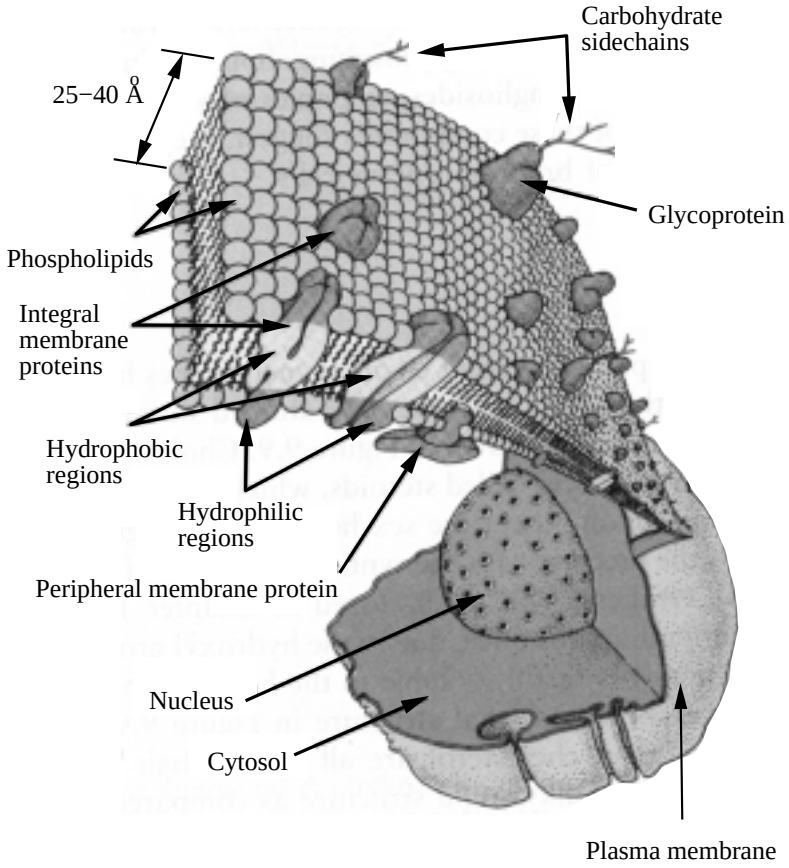

Figure 1.1: Schematic representation of a typical plasma membrane of a eukaryotic cell according to Singer's and Nicolson's fluid mosaic model (adopted from van Holde, Biochemistry). The phospholipid bilayer is about 2.5-4 nm thick and contains cholesterol as well as various proteins. Usually, inner and outer monolayers vary in their lipid composition.

The plasma membrane plays many roles, which can be summarized in four points:

1. Providing a dynamic matrix for enzyme reactions, receptors and molecular recognition for immune response.

2. Forming a diffusion barrier, which controls composition of the cell interior through highly organised transport processes.

3. Forming an electrically isolated layer with arrays of passive and active electrical components.

4. Forming a mechanical structure which influences shape and motion of cells or organelles.

Cell membranes are built up from only a few classes out of the huge variety of chemically distinguishable lipids. Lipids are characterized by charge and size of their headgroups and lengths and number of double bonds in their chains. Considering the many interaction phenomena which can take place between lipids and proteins [3], proteins can be also divided into various groups. Most ion channels and molecular pumps interact predominantly with the hydrophobic core of the bilayer. The anion exchange protein of red blood cells, band III, for example penetrates the bilayer with ca.13 helices [4]. However, peptide hormone receptors, membrane bound antibodies or cell adhesion mediating receptors are anchored by just one hydrophobic stem within the bilayer (e.g. glycophorin). Other proteins are attached to membranes by lipid anchors, such as the α-unit of G-proteins. Finally, soluble proteins may interact strongly with the bilayer surface when containing charged lipids, as shown for cytochrome c [5], myelin basic protein or type II myosin [6].

The two-dimensional character of membranes offers many advantages over a three dimensional assembly [7]. Diffusion controlled processes are much more efficient in lower dimensional space, because the average time τ a reactant needs to reach a target with diameter d in distance r in three dimensions

$$\tau^{(3)} \sim \frac{r^3}{3Dd} \tag{1.1}$$

reduces dramatically in two dimensions:

$$\tau^{(2)} \sim \frac{r^2}{2D} \ln \frac{r}{d} \tag{1.2}$$

where D denotes the diffusion coefficient [8]. Clearly, the probability for "three-partner-processes", such as an enzymatic reaction, is much higher in a two-dimensional rather than three-dimensional space. However, lateral and rotational diffusion of lipids and proteins takes place on various time scales, which

are usually much longer for proteins but can be modified over many orders of magnitudes.

Biological membranes have characteristic mechanical properties which explain a whole range of physiological phenomena, for instance cell movement and membrane fusion. While a fluid membrane allows high mobility of its components, an expansion of its area by just 2% would cause rupture [9].

Investigating the role of particular proteins for the functions of an active membrane is of central importance. In fact, membrane proteins are representing one-third of the information expressed by a genome [10], which underlines the need of better understanding even more. They provide an exciting technological challenge for structure determination, because they are not well-suited to study by the principal high-resolution structural methods, X-ray diffraction and liquid-state NMR. The lipids required for structure and function of membrane proteins interfere with crystallisation or rapid reorientation in solution. To date, only a handful of high-resolution structures have been obtained, for example by X-ray diffraction for the photosynthetic reaction centre of *Rhodopseudomonas viridis* [11] and cytochrome c oxidase [12]. Recently, 0.25 nm X-ray and 0.3 nm electron cryomicroscopic structures of bacteriorhodopsin were reported [13],[14]. The latter approach was pioneered by Henderson and Unwin and requires two-dimensional crystals, which have the advantage that the protein can be embedded in a membrane bilayer. An alternative approach is applying solid-state NMR spectroscopy, which does not require crystals, allows to use a bilayer environment and does not depend on short motional correlation times. New techniques for structure determination will be presented here.

1.2 Solid State NMR Spectroscopy

This section outlines briefly the theoretical foundations of solid state NMR with emphasising especially on those aspects which are needed for the experiments presented here. The first section 1.2.1 discusses lineshapes of I=1/2 and I=1 spin systems. Section 1.2.2 describes how sample rotation at the magic angle effects these spectra and how the spin system can be manipulated even further. The notation throughout this thesis will be in tensorial form to emphasize the anisotropy of interactions in solids.

1.2.1 Solid State NMR Lineshapes of I=1 and I=1/2 Spin Systems

It is necessary to distinguish nuclear spin interaction between external and internal fields of a general spin system I [15]:

$$\mathcal{H} = \mathcal{H}_{ext} + \mathcal{H}_{int} \tag{1.3}$$

$\mathcal{H}_{ext}$ describes the response of the spin system to the static magnetic field $\mathbf{B}_0$ and to radiofrequency pulses $\mathbf{B}_{RF}$, while $\mathcal{H}_{int}$ contains all internal interaction, such as spin-spin coupling, chemical shielding and spin-electron interaction. $\mathcal{H}_{int}$ can be written as a sum of all these interactions $\mathcal{H}_\lambda$:

$$\mathcal{H}_{int} = \sum_\lambda \mathcal{H}_\lambda. \tag{1.4}$$

In the following, only chemical shift, quadrupole and dipole couplings are considered. It is rather convenient to express these tensors in irreducible spherical notation:

$$\mathcal{H}_\lambda = C_\lambda \sum_{k=0}^{2} \sum_{q=-k}^{+k} (-1)^q A_{kq} T_{k-q} \tag{1.5}$$

which has the advantage that separate elements T_{kq} describe the spin operator, and A_{kq} its orientation with respect to the laboratory frame (=$\mathbf{B}_0$). The index λ separates parameters belonging to different interactions, but is dropped in the following in cases of minor importance for the sake of clarity. However, most interactions are related to the molecular structure, so some coordinate transformations from the molecular fixed frame to the laboratory frame will be necessary in later considerations, although important simplifications will be made initially.

Spin interaction become time dependent in strong magnetic fields B_0. If the field is so strong that $\|\mathcal{H}_{ext}\| \gg \|\mathcal{H}_{int}\|$, then only the secular part of $\mathcal{H}_{int}$ contributes in first order to the spectrum, i.e. $\mathcal{H}_{int}$ splits into two parts:

$$\mathcal{H}_{int} = \mathcal{H}'_{int} + \mathcal{H}''_{int} \tag{1.6}$$

The secular, time-independent part commutes with $\mathcal{H}_{ext}$ ($[\mathcal{H}_{ext}, \mathcal{H}'_{int}] = 0$) while the non-secular part does not commute ($[\mathcal{H}_{ext}, \mathcal{H}''_{int}] \neq 0$).

Eqn.1.5 can now be simplified, by considering that $[\mathrm{I}_z,\mathrm{T}_{kq}]=\mathrm{qT}_{kq}$ does not vanish, except for q=0 [15],[16].

$$\mathcal{H}'_\lambda = C_\lambda \left(A_{00}T_{00} + A_{10}T_{10} + A_{20}T_{20}\right) \tag{1.7}$$

For simplicity, $\mathcal{H}_\lambda$ will be used for $\mathcal{H}'_\lambda$ in the following. The angle dependency of the NMR spectra with respect to the laboratory frame defined by $\mathbf{B_0}$ is contained in $\mathbf{A_{kq}}$ in irreducible spherical form. However, many NMR interactions are defined with respect to the crystal frame, for the example of quadrupole coupling, the principal axis system is defined along the X-^{2}H bond (=z-axis), so it would make sense to consider using cartesian coordinates.

If $\mathbf{A}_{\alpha\beta}(\alpha\beta$=x,y,z) is the cartesian representation of a tensor $\mathbf{a}_{qk}$ in irreducible spherical notation, the following relations apply:

$$
\begin{aligned}
a_{00} &= -\frac{1}{\sqrt{3}}\left(A_{xx}+A_{yy}+A_{zz}\right) \\
a_{10} &= -\frac{i}{\sqrt{2}}\left(A_{xy}-A_{yx}\right) \\
a_{1\pm1} &= -\frac{1}{2}\left(A_{zx}-A_{xz}\pm i\left(A_{zy}-A_{yz}\right)\right) \\
a_{20} &= \frac{1}{\sqrt{6}}\left(3A_{zz}-\left(A_{xx}+A_{yy}+A_{zz}\right)\right) \\
a_{2\pm1} &= \mp\frac{1}{2}\left(A_{xz}+A_{zx}\pm i\left(A_{yx}+A_{zy}\right)\right) \\
a_{2\pm2} &= \frac{1}{2}\left(A_{xx}-A_{yy}\pm i\left(A_{xy}+A_{yx}\right)\right)
\end{aligned}
\tag{1.8}
$$

If $\mathbf{A}_{\alpha\beta}(\alpha\beta$=x,y,z) is actually an axial symmetric tensor defined in its principal axis system, i.e. with vanishing off-diagonal elements ($A_{\alpha\beta}$=$A_{\beta\alpha}$=0, $\alpha \neq \beta$) then the relations 1.8 simplify and a_{10}, $a_{1\pm1}$,$a_{2\pm1}$ vanish.

It is now necessary to rotate the interaction tensor from the native principal axis system into the laboratory frame in order to satisfy Eqn.1.7. The hierarchy and notation of reference frames used here is illustrated and defined in Fig.1.2.

The rotation itself is performed easily by applying Wigner rotation matrices $D^{(k)}_{q'q}$[17]:

$$A_{k0} = \sum_{q=-k}^{+k} D^{(k)}_{q0}(\Omega_{PL})a_{kq} \tag{1.9}$$

The angles $\Omega_{PL} = (\alpha_{PL}, \beta_{PL}, \gamma_{PL})$ are Euler angles, which are defined by the following three steps:

(a) rotation about z-axis through α_{PL} $(0 \leq \alpha_{PL} \leq 2\pi)$,

(b) rotation about new y_1 axis through β_{PL} $(0 \leq \beta_{PL} \leq \pi)$,

(c) rotation about new z_2 axis through γ_{PL} $(0 \leq \gamma_{PL} \leq 2\pi)$ [17].

The appropriate explicit expressions for the relevant matrix elements are given as:

$$D^{(0)}_{00} = 1 \tag{1.10}$$

$$D^{(2)}_{00} = \frac{1}{2}\left(3\cos^2\beta_{PL}-1\right) \tag{1.11}$$

$$D^{(2)}_{\pm20} = \frac{1}{2}\sqrt{\frac{3}{2}}\sin^2\beta_{PL}\left(\cos 2\alpha_{PL} \mp i\sin 2\alpha_{PL}\right) \tag{1.12}$$

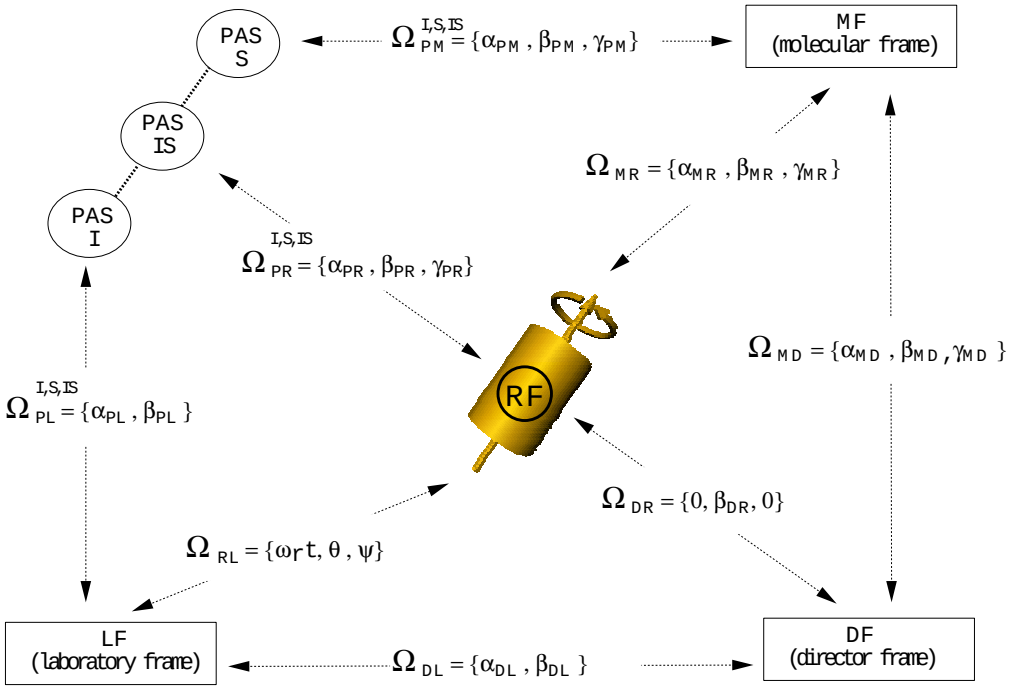

Figure 1.2: Angles and reference frames used here with the main focus on MAS. PAS is the principal axis system, MF the molecular fixed frames, DF a director system depending in the sample geometry (e.g. oriented membrane), RF the rotor frame and LF the laboratory frame defined by B_0. The rotation from RF into LF is time-dependent. Here, rotations by means of Euler angles are defined by the following three steps: (1.) rotation about z-axis through α ($0 \leq \alpha \leq 2\pi$), (2.) rotation about new y_1 axis through β ($0 \leq \beta \leq \pi$), (3) rotation about new z_2 axis through γ ($0 \leq \gamma \leq 2\pi$).

Using the Eqn.1.8,1.9 and 1.10-1.12, the secular Hamiltonian 1.7 can now be written as:

$$\mathcal{H}_\lambda = C_\lambda \begin{pmatrix} a_{00}T_{00} + \frac{1}{2}\left(3\cos^2\beta_{PL} - 1\right) a_{20}T_{20} \\ +\sqrt{\frac{3}{2}}\sin^2\beta_{PL}\cos 2\alpha_{PL} a_{2\pm2}T_{20} \end{pmatrix} \tag{1.13}$$

Table 1.1 gives explicit expressions for the tensor elements appearing in Eqn.1.13 for the three most important interactions:

1. The **chemical shielding tensor** in its PAS is diagonal, with the isotropic chemical shift defined as $\sigma_{iso} = (A_{xx} + A_{yy} + A_{zz})/3$, while the chemical shift anisotropy is given by $\delta = A_{zz} - \sigma_{iso}$. The tensor asymmetry parameter is $\eta = (A_{yy} - A_{xx})/(A_{zz} - \sigma_{iso})$. Using expressions from Tab.1.1, the Hamiltonian can be written as:

$$\mathcal{H}_{CS} = \gamma I_z B_0 \left(\sigma_{iso} + \frac{1}{2}\delta\left(3\cos^2\beta_{PL} - 1 - \eta\sin^2\beta_{PL}\cos 2\alpha_{PL}\right)\right) \tag{1.14}$$

2. By analogy, the **quadrupole interaction**, with the quadrupole coupling constant eq, is expressed by:

$$\mathcal{H}_Q = \frac{e^2qQ\left(3I_z^2 - 2\right)}{4\hbar}\left(3\cos^2\beta_{PL} - 1 - \eta\sin^2\beta_{PL}\cos 2\alpha_{PL}\right) \tag{1.15}$$

3. Considering now two spin-1/2 nuclei I and S which have the same gyromagnetic ratio and which interact via **dipolar coupling (**homonuclear case**)**. The interaction tensor is symmetrical (A_{xy}=A_{yx} etc.), its trace and the asymmetry parameter $\eta = 0$ vanish. With r_{IS} being the magnitude of the internuclear vector between both spins, the following is obtained:

$$\mathcal{H}_{IS} = \frac{\gamma_I\gamma_S\hbar}{2r_{IS}^3}\left(3\cos^2\beta_{PL} - 1\right)\left(3I_zS_z - \mathbf{I}\cdot\mathbf{S}\right) \tag{1.16}$$

In the following only $\mathcal{H}_{CS}$ and $\mathcal{H}_Q$ are considered. With m_I=$\pm$1/2 in $\mathcal{H}_{CS}$ and m_I=-1,0,1 in $\mathcal{H}_Q$, the transition frequencies for chemical shift and quadrupole interaction are given by:

$$\omega_{CS}(\alpha_{PL},\beta_{PL}) = \gamma B_0\left\{\sigma_{iso} + \frac{1}{2}\delta\left(3\cos^2\beta_{PL} - 1 - \eta\sin^2\beta_{PL}\cos 2\alpha_{PL}\right)\right\} \tag{1.17}$$

$$\omega_Q(\alpha_{PL},\beta_{PL}) = \pm\frac{3}{8}\frac{e^2qQ}{\hbar}\left(3\cos^2\beta_{PL} - 1 - \eta\sin^2\beta_{PL}\cos 2\alpha_{PL}\right) \tag{1.18}$$

The Euler angles α_{PL}, β_{PL} describe the orientation of the interaction tensor to the laboratory frame. An average over all orientations needs to be performed in case of polycrystalline samples. The free induction decay is given by:

$$S_{CS}(t) = \frac{1}{8\pi^2}\int_0^{\pi}\sin\beta_{PL}d\beta_{PL}\int_0^{2\pi}d\alpha_{PL}\exp\left(-i[\omega_{CS}(\alpha_{PL},\beta_{PL})t]\right) \quad (1.19)$$

$$S_Q(t) = \frac{1}{8\pi^2}\int_0^{\pi}\sin\beta_{PL}d\beta_{PL}\int_0^{2\pi}d\alpha_{PL}\left(\cos[\omega_Q(\alpha_{PL},\beta_{PL})t]\right) \quad (1.20)$$

Lineshapes for single crystals at various orientations and for polycrystalline samples are shown Fig.1.3 for chemical shift as well as for quadrupole interaction. The I=1 quadrupole powder spectrum is a typical Pake pattern, which is the sum of two I=1/2 spectra, corresponding to both possible transitions.

	Chemical Shift	Quadrupole	Dipole-Dipole
T_{00}	$-\frac{1}{\sqrt{3}}I_zB_0$	0	0
T_{20}	$\sqrt{\frac{2}{3}}I_zB_0$	$\frac{1}{\sqrt{6}}(3I_z^2-I(I+1))$	$\frac{1}{\sqrt{6}}(3I_zS_z-\mathbf{I}\cdot\mathbf{S})$
a_{00}	$-\sqrt{3}\sigma_{iso}$	0	0
a_{20}	$\sqrt{\frac{3}{2}}\delta$	$\sqrt{\frac{3}{2}}eq$	$\sqrt{\frac{3}{2}}\frac{\gamma_I\gamma_S\hbar}{r_{IS}^3}$
$a_{2\pm2}$	$-\frac{1}{2}\eta\delta$	$-\frac{1}{2}\eta eq$	0
C^{λ}	γ	$\frac{eQ}{2I(2I-1)\hbar}$	2

Table 1.1: Explicit tensor elements for chemical shift, quadrupole and dipole-dipole interaction.

1.2.2 NMR of Rotating Solids: Magic Angle Sample Spinning

The problem faced in a real experimental situation is already illustrated in Fig.1.3. Powder spectra of anisotropic interactions are rather broad, i.e. it is difficult to distinguish various magnetic non-equivalent nuclei in one sample. In principle, these different sites could be resolved in single crystals, which would however limit the applicability of solid state NMR to rather specific compounds only. A possible solution was shown by Andrew [18] and Lowe [19], who demonstrated that the spin systems can be easily manipulated towards a better resolution by rotating a sample about an axis which is tilted by an angle θ with respect to the magnetic field $\mathbf{B}_0$. In this situation, the Hamiltonian becomes time-dependent, which can be described by time-dependent coordinate transformations. Using the high-field approximation introduced above (Eqn.1.7), $\mathcal{H}_\lambda$ is given to:

$$\mathcal{H}_\lambda = C_\lambda\left(A_{00}(t)T_{00}+A_{10}(t)T_{10}+A_{20}(t)T_{20}\right) \quad (1.21)$$

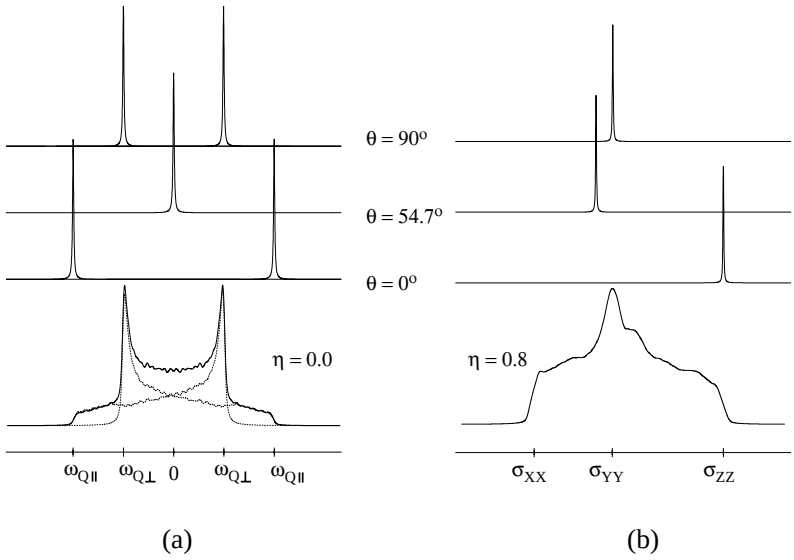

Figure 1.3: Simulated spectra for I=1 (a) and I=1/2 (b) spin system at different orientation $\Omega_{PL}\{0, \beta_{PL}, 0\}$ with respect to the laboratory frame. The powder spectra were obtained by averaging over α_{PL} and β_{PL} . The dotted lines in the quadrupolar powder pattern (Pake doublet) illustrate both transitions for I=1 spin systems.

As discussed before, $A_{00}(t)T_{00}$ is invariant under rotation and $A_{10}(t)T_{10}$ does not contribute to the spectrum in the first order, so only $A_{20}(t)$ needs to undergo a rotation from the principal axis system $(\alpha_{PR}, \beta_{PR}, \gamma_{PR})$ into the rotor frame and from there into the laboratory frame defined by $\mathbf{B}_0$. This last rotation actually introduces the time dependence due to sample spinning. By rotating the rotor frame into the laboratory frame by $(\omega_r t + \varphi_0, \theta, \psi)$, where ω_r defines the spinning speed, the expression for both rotations is:

$$A_{20}(t) = \sum_{q=-2}^{+2} \sum_{q'=-2}^{+2} D^{(2)}_{qq'}(\alpha_{PR}, \beta_{PR}, \gamma_{PR}) D^{(2)}_{q'0}(\omega_r t + \varphi_0, \theta, \psi) a_{2q} \tag{1.22}$$

Hamiltonian and transition frequency for the chemical shift of a spin-1/2 system can now be written in analogy to 1.14 and 1.17:

$$\begin{aligned} \mathcal{H}_{CS} &= \gamma I_z B_0 \sigma_{iso} + \\ &\quad \gamma I_z B_0 \delta \frac{1}{2}\left(3\cos^2\theta - 1\right)\left(\frac{1}{2}\left(3\cos^2\beta_{PR} - 1\right) - \frac{\eta}{2}\sin^2\beta_{PR}\cos 2\alpha_{PR}\right) + \\ &\quad \gamma I_z B_0 \delta \Psi(t) \end{aligned} \tag{1.23}$$

$$\begin{aligned} \omega_{CS} &= \gamma B_0 \sigma_{iso} + \\ &\quad \gamma B_0 \delta \frac{1}{2}\left(3\cos^2\theta - 1\right)\left(\frac{1}{2}\left(3\cos^2\beta_{PR} - 1\right) - \frac{\eta}{2}\sin^2\beta_{PR}\cos 2\alpha_{PR}\right) + \\ &\quad \gamma B_0 \delta \Psi(t) \end{aligned} \tag{1.24}$$

where $\Psi(t)$ is obtained by writing expression 1.22 explicitly:

$$\begin{aligned} \Psi(t) &= C_1 \cos(\omega_r t) + S_1 \sin(\omega_r t) + C_2 \cos(2\omega_r t) + S_2 \sin(2\omega_r t) \\ C_1 &= \frac{1}{2}\sin 2\theta \sin\beta_{PR} \left\{ \begin{array}{c} \cos\beta_{PR}\left(\eta\cos 2\gamma_{PR} - 3\right)\cos\alpha_{PR} \\ -\eta\sin 2\gamma_{PR}\sin\alpha_{PR} \end{array} \right\} \\ S_1 &= \frac{1}{2}\sin 2\theta \sin\beta_{PR} \left\{ \begin{array}{c} \cos\beta_{PR}\left(3 - \eta\cos 2\gamma_{PR}\right)\sin\alpha_{PR} \\ -\eta\sin 2\gamma_{PR}\cos\alpha_{PR} \end{array} \right\} \\ C_2 &= \frac{1}{2}\sin^2\theta \left\{ \begin{array}{c} \left[\frac{3}{2}\sin^2\beta_{PR} + (\eta/2)\cos 2\gamma_{PR}\left(1 + \cos^2\beta_{PR}\right)\right]\cos 2\alpha_{PR} \\ -\eta\cos\beta_{PR}\sin 2\gamma_{PR}\sin 2\alpha_{PR} \end{array} \right\} \\ S_2 &= \frac{1}{2}\sin^2\theta \left\{ \begin{array}{c} -\left[\frac{3}{2}\sin^2\beta_{PR} + (\eta/2)\cos 2\gamma_{PR}\left(1 + \cos^2\beta_{PR}\right)\right]\sin 2\alpha_{PR} \\ -\eta\cos\beta_{PR}\sin 2\gamma_{PR}\cos 2\alpha_{PR} \end{array} \right\} \end{aligned} \tag{1.25}$$

It can be seen that $\Psi(t)$ has a periodicity of ω_r and $2\omega_r$. The free induction decay of a polycrystalline sample can now be calculated by performing a powder averaging over a certain period of time [20]:

$$S_{CS}(t) = \frac{1}{8\pi^2} \int_0^{2\pi} \int_0^{\pi} \int_0^{2\pi} \exp\left[i\Phi(\alpha_{PR}, \beta_{PR}, \gamma_{PR}, t)\right] d\alpha_{PR} \sin\beta_{PR} d\beta_{PR} d\gamma_{PR} \quad (1.26)$$

where $\Phi(\alpha_{PR}, \beta_{PR}, \gamma_{PR}, t)$ is the phase angle describing the evolution of the magnetisation vector under sample rotation:

$$\begin{aligned} \Phi(\alpha_{PR}, \beta_{PR}, \gamma_{PR}, t) &= \int_0^t \omega_{CS}(\alpha_{PR}, \beta_{PR}, \gamma_{PR}, t')dt' \quad (1.27) \\ &= \gamma B_0 \sigma_{iso} t + \\ &\quad \gamma B_0 \delta t \left(\frac{3\cos^2\theta - 1}{2}\right) \begin{pmatrix} \frac{\left(3\cos^2\beta_{PR} - 1\right)}{2} \\ -\frac{\eta}{2}\sin^2\beta_{PR}\cos 2\alpha_{PR} \end{pmatrix} + \\ &\quad \gamma B_0 \frac{\delta}{\omega_r} \begin{pmatrix} C_1 \sin\omega_r t - S_1 \cos\omega_r t \\ +\frac{C_2}{2}\sin 2\omega_r t - \frac{S_2}{2}\cos 2\omega_r t \end{pmatrix} - \Phi_0 \end{aligned}$$

The chemical shift anisotropy is scaled with δ/ω_r. For modest spinning speeds, i.e. $\delta/\omega_r \geq 1$ rotor echoes are observed in the time domain signal or sidebands separated by ω_r in the Fourier transformed spectrum (Fig.1.4). An expression for the sideband intensity I_N can be derived by calculating first the FID of a site in a single crystallite, which is given by:

$$S_{CS}(\alpha_{PR}, \beta_{PR}, \gamma_{PR}, t) = \exp\left[i\Phi(\alpha_{PR}, \beta_{PR}, \gamma_{PR}, t)\right] \quad (1.28)$$

Rotations about the rotor axis Z_R are described by γ_{PR} as well as ω_rt, so that both can be replaced by the sum $\gamma_{PR} + \omega_r$t. The FID can now be rewritten with the phase angle $\Phi = \Phi_1(w_r t) - \Phi_0$ as:

$$\begin{aligned} S_{CS}(\alpha_{PR}, \beta_{PR}, \gamma_{PR}, t) &= \exp\left[i\Phi_1(\alpha_{PR}, \beta_{PR}, \gamma_{PR} + \omega_r t)\right] \exp\left[-i\Phi_0\right] \\ &= f(\alpha_{PR}, \beta_{PR}, \gamma_{PR} + \omega_r t) f^*(\alpha_{PR}, \beta_{PR}, \gamma_{PR}) \quad (1.29) \end{aligned}$$

The signal is periodic with $t_r = 2\pi/\omega_r$. Sideband intensities can only appear at $\omega = N\omega_r$. Their intensities are obtained by Fourier transforming S_{CS} over one rotor period:

$$I_N(\alpha_{PR}, \beta_{PR}, \gamma_{PR}) = \int_0^{t_r} \frac{dt}{t_r} f(\gamma_{PR} + \omega_r t) f^*(\gamma_{PR}) \exp\left[-i\omega_r N t\right] \quad (1.30)$$

One rotor period can actually be expressed as a rotation by 2π about the rotor axis and using the substitution $\gamma' = \gamma_{PR} + \omega_r t$:

$$
\begin{aligned}
I_N(\alpha_{PR},\beta_{PR},\gamma_{PR}) &= f^*(\gamma_{PR})\int_0^{2\pi}\frac{d\gamma'}{2\pi}f(\gamma'_{PR})\exp\left[-i\gamma' N\right]\exp\left[i\gamma_{PR}N\right] \\
&= f^*(\gamma_{PR})\exp\left[i\gamma_{PR}N\right]\int_0^{2\pi}\frac{d\gamma'}{2\pi}f(\alpha_{PR},\beta_{PR},\gamma'_{PR})\exp\left[-i\gamma' N\right] \\
&= f^*(\gamma_{PR})\exp\left[i\gamma_{PR}N\right]F_N(\alpha_{PR},\beta_{PR}) \qquad (1.31)
\end{aligned}
$$

The functions f(γ_{PR}) and $F_N(\alpha_{PR},\beta_{PR})$ were introduced, because they are used throughout the literature [15, 20, 21]. I_N is usually complex, giving rise to positive and negative sidebands (Fig.1.4,[20]). A powder average has to be performed over Ω_{PR} in order to calculate sideband intensities from polycrystalline samples. In these cases, the intensities I_N are always positive and only depend on δ and η which has been used for calculating these parameters from MAS spectra. Maricq and Waugh suggested a moment analysis [20] while Herzfeld and Berger developed a graphical method, which uses relative sideband intensities [22].

So far, only slow spinning speeds have been discussed, but it has been shown that anisotropic interactions are scaled with $1/\omega_r$ (Eqn.1.27). In a regime where the spinning speed is large, $\Phi(t)$ (Eqn.1.27) will lose its oscillating terms. By choosing now an angle θ:

$$\theta = \arccos\frac{1}{\sqrt{3}} = 54.7356...^o \qquad (1.32)$$

only the isotropic chemical shift would be left in Eqn.1.27. For this particular situation, $\mathcal{H}_\lambda$ simplifies to:

$$\overline{\mathcal{H}}_\lambda = C_\lambda\left(A_{00}T_{00} + \frac{1}{2}\left(3\cos^2\theta - 1\right)A_{20}T_{20}\right) \qquad (1.33)$$

In the case of dipole-dipole or quadrupole interactions, A_{00} vanishes (Tab.1.1) and fast sample rotation could remove these interactions completely. The result is an isotropically averaged Hamiltonian appropriate to a liquid.

However, it is not always practicable to achieve spinning speeds which exceed these interactions. For that reason, two cases have to be considered, which where classified as "homogeneous" and "inhomogeneous" by Maricq and Waugh [20]. The Hamiltonian for i spins with chemical shift interactions only is commuting with itself ($[\mathcal{H}^i_{CS}(t),\mathcal{H}^i_{CS}(t')] = 0$), and is called "inhomogeneous". Eqn.1.23 becomes at the magic angle:

$$\mathcal{H}^i_{CS} = \gamma^i I^i_z B_0 \sigma^i_{iso} + \gamma^i I^i_z B_0 \delta^i \Psi^i(t) \qquad (1.34)$$

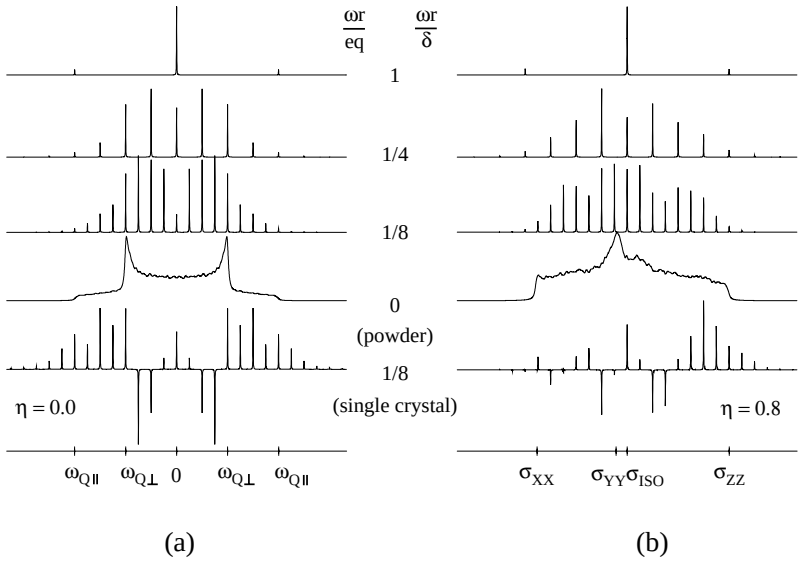

Figure 1.4: The effect of sample rotation on the spectra of I=1 (a) and I=1/2 spin systems (b) at different relative spinning speeds. All spectra are scaled to the same intensity. MAS spectra of single crystals exhibit dispersive and absorptive sidebands, while powder spectra are always positive. The site in the single crystal in this example simulation has an orientation $\Omega_{PR}\{0,45,0\}$ with respect to the rotor frame.

and spinning sidebands are observed, as discussed before. The same does not apply for homonuclear dipolar couplings. The Hamiltonian for the dipolar coupling between spins i and j

$$\mathcal{H}_D^{ij} = \frac{\gamma_i \gamma_j \hbar}{r_{ij}^3}(3I_{zi}I_{zj} - \mathbf{I_i}\cdot\mathbf{I_j})\Psi^{ij}(t) \tag{1.35}$$

does not commute for $(3I_iI_j - \mathbf{I_i}\cdot\mathbf{I_j})$ for spin pairs ij and their orientation-dependent pre-factor $\Psi^{ij}(t)$ are in general different. In this situation, the spectrum would be hardly effected by MAS. However, in many experimental situations, the Hamiltonian appears to be inhomogeneous.

1.2.3 ^{1}H-Decoupling

The heteronuclear dipolar coupling between nuclei of low abundance such as ^{13}C or ^{15}N with their neighbouring protons is much too strong to be averaged just by sample spinning at the magic angle, but a solution was found by additional spin manipulation in the form of double resonance experiments [23]. If I stands for ^{1}H and S for the low-γ nucleus under consideration, then simple continuous wave irradiation of I causes rapid saturation of the I spin multiplet. This means that the spin system evolves under an effective Hamiltonian comprising only the Zeeman term for spin S, which is now decoupled. Fig.1.5 shows an example for a powder sample of glycine. The decoupling efficiency can be improved remarkably by using advanced pulse schemes such as Lee-Goldberg decoupling [24].

1.2.4 Cross Polarisation

Despite achieving high resolution by MAS and ^{1}H decoupling, a sensitivity problem still remains for studying low-γ nuclei such as ^{13}C or ^{15}N. Natural abundance and relative sensitivity of ^{13}C is only 1.108% and 1.59×10^{-2} (compared to ^{1}H) and for ^{15}N 0.37% and 1.04×10^{-3}, respectively. However, the presence of strong dipolar couplings between these rare nuclei and abundant protons can be exploited to provide a signal-enhancement. This cross polarisation experiment requires three steps [25]:

1. The spin temperature of the abundant ^{1}H-spin reservoir is lowered by applying a $90^o x$ pulse.

2. Polarisation transfer from the abundant I-spin reservoir to the rare S-spin reservoir takes place by matching the precession frequencies of I and S (Hartmann-Hahn condition): $\gamma_I B_{1I} = \gamma_S B_{1S}$. This is achieved by a spin-lock field applied simultaneously to I and S.

3. S-spins are observed but the spin lock field is maintained on the I spins during detection in order to prevent effects from heteronuclear dipolar coupling.

The signal enhancement of spin I is proportional to γ_I/γ_S (four times for $^1H/^{13}C$). A further advantage is that the spin-lattice relaxation time T_1 of protons is considerably smaller than for ^{13}C, i.e. the delay time between multiple scans can be chosen to be shorter. It is not even necessary to wait for the ^1H spin reservoir to re-polarize, since not all magnetisation is transferred, resulting in a further increase in sensitivity by accumulating more signal in less time. A more detailed description can be found elsewhere [15].

Even better sensitivity enhancement has been achieved recently by dynamic nuclear polarisation, in which magnetisation of unpaired electrons is transferred to coupled nuclear spins by microwave irradiation [26].

1.2.5 Recoupling-Rotational Resonance

The dipolar coupling between nuclei in specific sites in solids is an important structural parameter due to its r^{-3} distance dependence, but magic angle sample spinning, which is necessary to obtain well resolved spectra, also reduces the dipolar coupling remarkably. Andrew and co-workers in the 60's [27, 28], observed that at certain spinning speeds the resonance lines of abundant nuclei with different chemical shifts are dipolar broadened and an enhanced Zeeman magnetisation takes place. This phenomenon has been called rotational resonance (RR). Raleigh found similar effects in diluted pairs of like spins [29]. The use of rotational resonance for molecular structure determination has been suggested and demonstrated for a number of rather complex molecular systems, which has enabled the development of a general theory of homonuclear spin pair systems under MAS conditions by Levitt and co-workers [30].

The sample, containing a dipolar coupled pair of like spin nuclei, is set spinning at a rate $n\omega_r$ (n=1,2,3) which equals the frequency difference between the isotropic chemical shifts of both spins. At that rate, lines are broadening and split into doublets, which is illustrated for [1-2-^{13}C]-glycine in Fig.1.5. The dipolar coupling is reintroduced at these spinning speeds and can now be used for distance determination, either by analysing the lineshape, or by measuring Zeeman magnetisation exchange between both sites.

Spinning speed sensitivity and restriction to an isolated spin pair only made the development of broadband recoupling techniques necessary, for example DRAMA (dipolar recovery at the magic angle)[31], RFDR (radiofrequency driven recoupling) [32], MELODRAMA [33] or C7 [34] and for heteronuclear recoupling REDOR (rotational echo double resonance) [35].

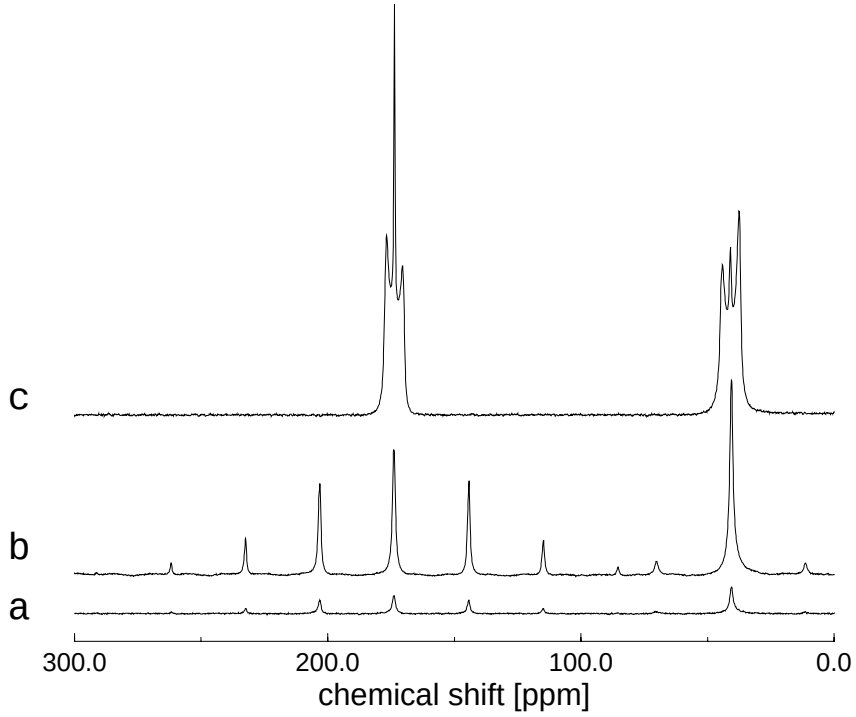

Figure 1.5: 100.63 MHz ^{13}C-MAS spectra of a polycrystalline 1:7 mole/mole mixture of [1,2-^{13}C]-glycine and unlabelled glycine under proton decoupling (a), using cross polarisation (b) (both at a spinning rate of ω_r=3500 Hz), and at n=1 rotational resonance at ω_r=13354 Hz (c).

1.3 NMR Spectroscopy of Biomembranes

Structural studies of biomembranes, especially membrane-bound proteins and peptides, by NMR, have undergone a remarkable development in recent years [36]. Liquid state NMR can be applied to membrane proteins solubilized in micelles. Here, only solid state NMR is considered in detail, which involves two different approaches, static NMR on uniformly aligned samples [37], and Magic Angle Sample Spinning (MAS) NMR applied to unoriented samples, as recently reviewed by Smith et al. [38]. From the structural point of view, the two central questions to be resolved are the protein secondary structure in the membrane, and the molecular orientation with respect to the membrane [37]. The central technical difficulties are to achieve a sufficiently high spectral resolution for the nuclei of interest (^{1}H, ^{13}C, ^{15}N), to utilize dipolar and J-couplings for obtaining structural constraints, and information about the orientation of specific sites in the peptide or protein with respect to the bilayer [39].

1.3.1 Membrane Proteins in Micelles

The correlation time problem, which exists due to immobilized or slowly reorienting membrane proteins, must be overcome when applying high resolution NMR techniques. The problem can be solved by solubilizing proteins in high lipid concentration to obtain small micelles with only one protein, which would reorient quickly and isotropically. High fields, high temperature and isotopic labelling are necessary to obtain useful spectral resolution. Besides various applications to peptides of up to 50 residues [40], recent advances have been made by studying isotopically labelled native bacteriorhodopsin in detergent micelles. NOEs within the chromophore were reported [41]. Due to the correlation time problem, this approach might be limited to molecules smaller than 30-40 kDa.

1.3.2 Static Solid State NMR: Membrane Proteins in Bilayers

It was demonstrated in the introduction to static solid state NMR, that the signal observed from a second rank tensor interaction depends on its orientation Ω_{PL} with respect to the laboratory frame (Eqn.1.17). Sharp resonance lines can be obtained from sites in single crystals (Fig.1.3). This effect has been used extensively for studying macroscopically aligned membranes, by utilizing the orientational dependent anisotropies of either quadrupole interaction (^{2}H), of chemical shielding tensors (^{13}C, ^{15}N, ^{31}P) and of the dipolar couplings (^{15}N-^{1}H). For example, the orientation of ^{2}H labelled chromophores in bacteriorhodopsin [42] and bovine rhodoposin [43] were determined as well as orientation and structure of gramicidin [44] and other helical peptides [45]. Oriented membrane proteins can

be either prepared by aligning them in bilayers on glass disks [37],[46], or by using bicelles [47]. Using bicelles became a more generally accessible method with the discovery that by adding lanthanide ions, their director axis orients parallel to $\mathbf{B}_0$[48],[49]. The clear potential of this approach is in acquiring molecular orientation with respect to the membrane director frame as well as structural constraints. A remarkable resolution has been achieved in cases where the sample is extremely well oriented. The possibility to obtaining completely resolved ^{15}N spectra of fully labelled peptides were recently shown for the fd-coat protein [50]. Precise resonance assignment in multiple or uniformly labelled proteins still remains a challenge, because each resonance depends on tensor size and orientation, which would make assuming a molecular geometry necessary prior to full spectral assignment.

1.3.3 Magic Angle Sample Spinning: Membrane Proteins in Bilayers

In contrast to static NMR on oriented membranes, MAS spectroscopy does not require uniformly aligned samples in order to achieve a good spectral resolution (Fig.1.4). However, working with unoriented membrane systems means losing a general sample reference frame and also the angle dependence of second rank tensor interaction. Additionally, dipolar coupling, which is needed to obtain distance constraints, is averaged under sample spinning and has to be reintroduced by dipolar recoupling techniques.

MAS has been used mainly for two classes of problems, namely for structure and interaction of membrane bound peptides and for conformation of ligands bound to large complexes. Current MAS techniques still fail to produce a large matrix of distance constraints, but selective protein backbone labelling allows specific distance or torsional angle measurements for establishing a local secondary structure [38]. Usually, ^{13}Cα-^{13}C=O or ^{15}N-^{13}Cα spin pairs are used. MAS proved to be particularly useful for conformational studies of ligands bound to membrane proteins. Examples involve the observation of glucose bound to the galactose-H^+ symport protein in E.coli by Spooner et al. [51], of an inhibitor bound to gastric H^+/K^+ *ATPase* [52] and of acetylcholine bound to the acetylcholine receptor [53]. Distance and torsion angle measurements between ^{13}C labelled positions in bovine rhodopsin have been obtained by applying rotational resonance and C7 [54].

Although the general perspective of MAS towards complete structural resolution of labelled membrane proteins is still ambivalent, as discussed in a statistical analysis by Tycko [39], good progress has been made in development and application of broadband recoupling techniques and efficient homonuclear decoupling [24], which are essential for multiple labelling.

MAS NMR has become an effective approach for probing structure and mecha-

nism of membrane proteins by distance and torsion angle measurements (0.65-1.1 nm for ^{13}C-^{13}C and ^{13}C-^{19}F) as well as by studying chemical shifts.

1.3.4 Magic Angle Sample Spinning on Oriented Membrane Bilayers

It has been said, that orientation with respect to the membrane director frame can not be measured by MAS, although it would be rather tempting to find a way to perform MAS spectroscopy on uniformly aligned membranes. Deviations from perfect alignment, which are common for large proteins such as rhodopsin in bilayers, could make static NMR a difficult task [43], while MAS would always produce well resolved resonance lines. MAS spectra of single crystals, as shown in Fig.1.4, illustrate already what might be expected. Orientational information is contained in spinning sidebands which appear about the isotropic central line. Here, a new basic MAS experiment is suggested, which would allow orientations of second rank tensors with respect to the director frame to be extracted. In the following, the abbreviation MAOSS (magic angle oriented sample spinning) will refer to this type of experiment in contrast to MAS on unoriented material. As shown in Fig.1.6, biomembranes can be uniformly aligned on thin glass discs [46, 55] which are mounted into a MAS rotor so that the membrane normal is parallel to the rotor axis. Tensor orientations can now be obtained by analysing spinning sideband patterns of sites in slowly tumbling or immobile membrane proteins. However, mobile membrane components, such as lipids, would rotate about the magic angle ($\tau_c \sim 10^{-10}$ sec), which averages the strong dipolar ^{1}H-^{1}H couplings and allows a high ^{1}H resolution.

Proton-MAS on oriented membranes will be discussed in Chapter 2, while Chapter 3 outlines the analysis of MAOSS sideband patterns from inhomogeneous interactions. Chapter 4 demonstrates the application of ^{2}H-MAS to oriented bacteriorhodopsin. Chapters 5 and 6 will introduce and demonstrate the use of rotational resonance MAS, MAOSS and lanthanide ions for the study of membrane bound peptides, with the M13 coat protein.

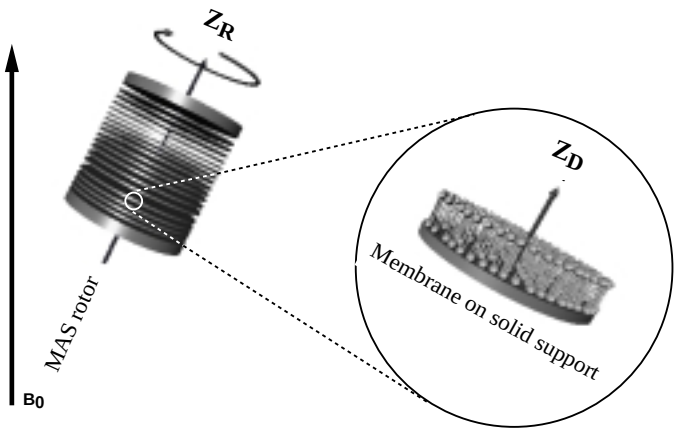

Figure 1.6: Main principle for MAOSS experiments: Membranes are uniformly aligned on thin, precisely cut glass disks, stacked on top of each other and mounted into a standard MAS rotor. The membrane normal Z_D is parallel to the rotor axis Z_R.

Chapter 2

Resolution Enhancement through Molecular Dynamics: ^{1}H MAS on Oriented Lipid Multilayers

Abstract

The spectral linewidth in ^{1}H spectra of multi-lamellar lipid dispersions is dominated by the dipolar coupling. The highly anisotropic intermolecular motions of membrane components, such as rotational diffusion about the lipid long axis ($\tau_c \simeq 10^{-10}$ sec), can be utilized for averaging dipolar interactions by placing uniformly aligned lipid multilayer with the membrane normal at the magic angle. Each lipid molecule rotates about the magic angle and additional macroscopic sample rotation averages orientation defects. The dramatic resolution improvement for protons which is achieved in a lipid sample at only 220 Hz spinning speed in a 9.4 T field is slightly better than any published data to date using ultra-high fields (up to 17.6 T) and high-speed spinning (14 kHz). Here, the first ^{1}H spectra of uniformly aligned dimyristoylphosphatidylcholine (DMPC) bilayers are presented. ^{1}H resolution enhancement for the aromatic region of the M13 coat protein reconstituted into DMPC bilayers and general potential and possible perspectives of this technique are discussed.

2.1 Introduction

It has been discussed in the general introduction to solid-state NMR in Chapter 1, that the dipolar coupling is described by a traceless and symmetrical second rank tensor. The Hamiltonian for an isolated homonuclear spin pair can now be written, according to Eqn.1.16 as :

$$\mathcal{H}_D = \frac{\gamma_{1H}^2 \hbar}{2r_{12}^3} \left(3\cos^2 \beta_{PL} - 1\right) \left(3I_{1Z}I_{2Z} - \mathbf{I}_1\mathbf{I}_2\right) \tag{2.1}$$

where β_{PL} denotes the Euler angle [17] needed to rotate the dipolar tensor from its principal axis system into the laboratory frame (α_{PL} can be set to zero due to the symmetry of the dipolar tensor and γ_{PL} can be neglected in the secular part of the Hamiltonian, see Fig.1.2.). The gyromagnetic ratio of protons is $\gamma_{1H} = 26.75 \times 10^7 As/kg$ and r_{12} is the magnitude of the vector connecting both spins. By performing a powder average and neglecting all other interactions, a Pake pattern with a splitting corresponding to the dipolar coupling is obtained. Since the dipolar interaction is a through space interaction, the coupling between all proton spins in the sample has to be considered:

$$\mathcal{H}_D = \sum_{i>j} \frac{\gamma_{1H}^2 \hbar}{2r_{ij}^3} \left(3\cos^2 \beta_{PL}^{ij} - 1\right) \left(3I_{iZ}I_{jZ} - \mathbf{I}_i\mathbf{I}_j\right) \tag{2.2}$$

which gives a network of couplings, in which all spins are involved, i.e. manipulating one spin would mean manipulating the whole spin network. The resulting spectrum is no longer a superposition of independent lines (inhomogeneous case) but is homogeneously broadened [15]. The description of the modulation of such a spectrum by MAS is difficult to handle. However, it has been found experimentally, that under MAS conditions a sideband pattern forms. The resonance lines are broadened according to the ratio of dipolar coupling to spinning speed ω_D/ω_r [18],[19]. Approximated simulations can be performed by making use of the strong distance dependence of dipolar couplings, i.e. by only considering adjacent spins. The protons in a methylene group can now be treated as an isolated two-spin-system and remaining multi-spin couplings can be included in the form of a broadening function [56, 57, 58].

Due to this strongly coupled network of spins, protons are experimentally difficult to use in solid-state NMR. Their large dipolar couplings of up to 36 kHz are exceeding normally available MAS spinning speeds ($\sim$ 25 kHz) which would be necessary to obtain a sufficient averaging and hence resolution. However, utilising protons for biological solid-state NMR is rather attractive since in solution NMR dipolar and J-couplings of protons mainly deliver the structural information which is normally obtained from selective labelling with low γ nuclei (^{13}C, ^{15}N) in solid-state NMR. Being able to achieve a sufficient ^{1}H resolution in biological membranes would then permit the application of well developed solution state NMR techniques. Additionally, the signal/noise problem which occurs by selective labelling in biological material, which cannot normally be provided in large quantities, would be overcome. This approach is supported by the fact that many membrane components are highly mobile in a motional regime in which the dipolar coupling tensor would be pre-averaged. The first ^{1}H MAS spectra of lipids were published by Oldfield and co-workers [59, 60, 61] and a number of

attempts have been undertaken to improve the proton resolution in solid-state NMR of biomembranes [62, 63, 64, 65, 66, 67], mainly by applying ultra high magnetic fields or by ultra-fast MAS spinning. It has been possible to resolve lipid and some peptide resonances. However, the resolution enhancement one would expect from high field / high speed MAS has so far not been achieved [62]. Here a new approach is presented and discussed, which might help to overcome these problems.

As shown in Fig.1.6 in Chapter 1, biomembranes can be uniformly aligned on thin glass discs [46, 55] which are mounted into a MAS rotor. If the membrane normal is parallel to the rotor axis, lipids would rotate about the magic angle with a correlation time of $\tau_c \simeq 10^{-10}$ sec causing the strong dipolar ^{1}H-^{1}H couplings to collapse. Additional sample rotation can average orientational defects, which would remove residual dipolar ^{1}H-^{1}H couplings and allows a high ^{1}H resolution (see Fig.2.1).

2.2 Materials and Methods

Round, 0.06-0.08 mm thin glass plates with a diameter of 5.4 mm (Marienfelde GmbH, Germany) were cleaned in nitric acid and methanol/ethanol and subsequently dried under a stream of nitrogen gas. The disc diameter was chosen to fit precisely into a standard Bruker 7 mm MAS rotor (RotoTec GmbH, Germany). The M13 coat protein was synthesized using standard solid-phase FMOC chemistry (NSR Centre, Nijmegen, The Netherlands); Asp was replaced with Asn. DMPC (dimyristoylphosphatidylcholine) was purchased from Sigma, UK and used without further purification. To orient protein and lipids on the glass plates, protein and DMPC were co-dissolved in trifluoroacetic acid (Aldrich, UK) and chloroform (BDH) in a lipid to protein mole ratio of 15:1 and spread as one 10 μl drop onto the glass disks which were then thoroughly dried with a stream of nitrogen. Each drop contained 0.2 mg material and special care has been taken to ensure that the solvent covers the disk surface completely. After adding all material, samples were exposed to high vacuum for 12 hours and hydrated by adding 0.25 μl D_2O (Aldrich) directly to each sample followed by an empty, clean disk on top. The same procedures were used for pure DMPC samples, however no TFA was added. The prepared sample "sandwiches" were allowed to equilibrate in a hydration chamber for 48 hours at 93% relative humidity (over-saturated KNO_3/D_2O solution) and 310 K. Glass plates (25) were placed on top of each other and mounted carefully into a 7 mm MAS rotor using a specifically designed tool (see Appendix A). Each MAS rotor contained 5-10mg material.

Special KelF inserts on top and bottom guaranteed a fixed and stable position of each disc. An amount of 5 μl D_2O was added to the rotor before closing it with a standard non-venting KelF cap. For comparison with random distributions, multilamellar dispersion of M13 in its α-oligomeric form were prepared by

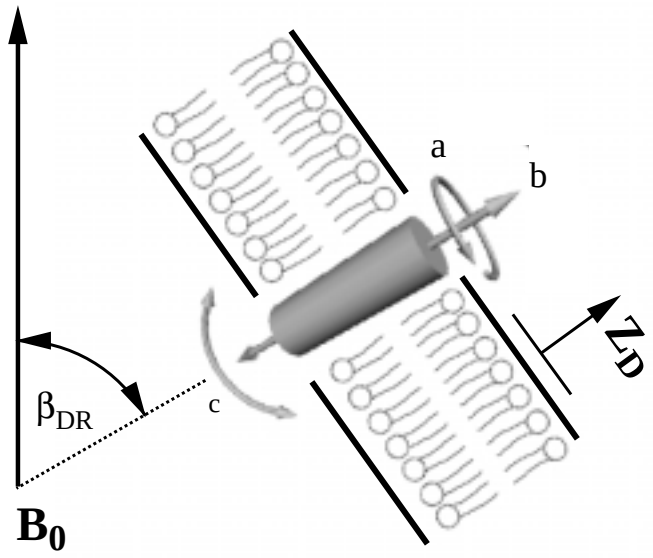

Figure 2.1: The various dynamic processes for lipids in multilayers are mainly dominated by fast rotational diffusion about the molecular long axis (a), with slow, collective motions, which modulate the bilayer normal $\mathbf{Z_D}$ (b,c) also occuring. By orienting a perfectly alligned lipid multilayer with the membrane normal $\mathbf{Z_D}$ at the magic angle β_{DR}=54.7^o, each molecule would actually rotate ($\tau_c \simeq 10^{-10}$ sec) about the magic angle and so ^{1}H-^{1}H dipolar coupling (40kHz) would vanish.

reconstitution into DMPC as described previously [68].
All spectra were recorded at 400.13 MHz for ^{1}H using a Bruker MSL 400 and double resonance 7mm and 4 mm MAS probes (Bruker, Germany). Typical $\pi/2$ pulse-lengths were 6 μs. The spinning speed was controlled within a range of ± 3 Hz. An oscilloscope was used to control the rotor stability at low spinning rates. Static phosphorus NMR suggests a mosaic spread of $\pm 3^o$ for the lipids in the sample.
The stability of sample orientation under spinning conditions was checked after each spinning experiment by comparison of static ^{1}H and ^{31}P spectra.

2.3 Results

The static ^{1}H spectrum of a multilamellar dispersion of DMPC/D_2O in its fluid (Lα) phase at 318 K is shown in Fig.2.2a. By uniformly aligning DMPC bilayers on glass disks with the membrane normal at the magic angle, as illustrated in Fig.2.1, a dramatic line width reduction from about 20 ppm to 6 ppm, which is just the chemical shift dispersion, is achieved (Fig.2.2b). This effect has been illustrated before by Smith et al. [55], where static ^{1}H spectra at the magic angle were used for estimating the amount of water in the samples. If the sample is set spinning, a dramatic spectral resolution is observed at a speed as slow as 220 Hz (Fig.2.2c). This spectrum is plotted on an expanded horizontal scale from 6.0 to 0.0 ppm below Fig.2.2c. A resonance assignment has been obtained from published literature [59],[64] and is given in Table 2.1 together with the full width at half maximum for each relevant resonance. Spinning sidebands, which are not removed at this speed are labelled with arrows in Fig.2.2. The linewidth ranges from 29 Hz for the CH_2 resonance to only 9 Hz for the $N(CH_3)_3$ head group. This resolution is slightly better than all published data so far using solid-state NMR techniques on biomembrane systems. The first reports of the application of MAS to biomembranes showed linewidths of 40 to 60 Hz at 11.7 T [59],[60]. Some improvements have been made by ultra-fast spinning of up to $\omega_r = 14000$ Hz, as shown by Davis et al. [62], where the linewidths were between 13 and 34 Hz (8.455 T). Pampel and Volke reported 20 Hz linewidth for the most narrow lines using a ultra-high field of 17.6 T and 8000 Hz spinning speed for their MAS studies [65].

The applicability of this method to membrane-bound peptides is illustrated in Fig.2.3. The M13 coat protein, a 50mer membrane-bound peptide has been reconstituted (see Materials and Methods) into DMPC in order to carry out standard MAS studies at 318 K and a spinning rate of $\omega_r = 10000$ Hz (Fig.2.3a) and Fig.2.3b is a vertical expansion of the aromatic region from 6.0 to 9.0 ppm of this spectrum. The signal arises from the amino acids Phe-11, Tyr-21, Tyr-24 and Trp-26, Phe-42, Phe-45. A oriented sample of M13 embedded in DMPC bilayers was prepared for MAOSS experiments. Fig.2.3c shows the expansion of

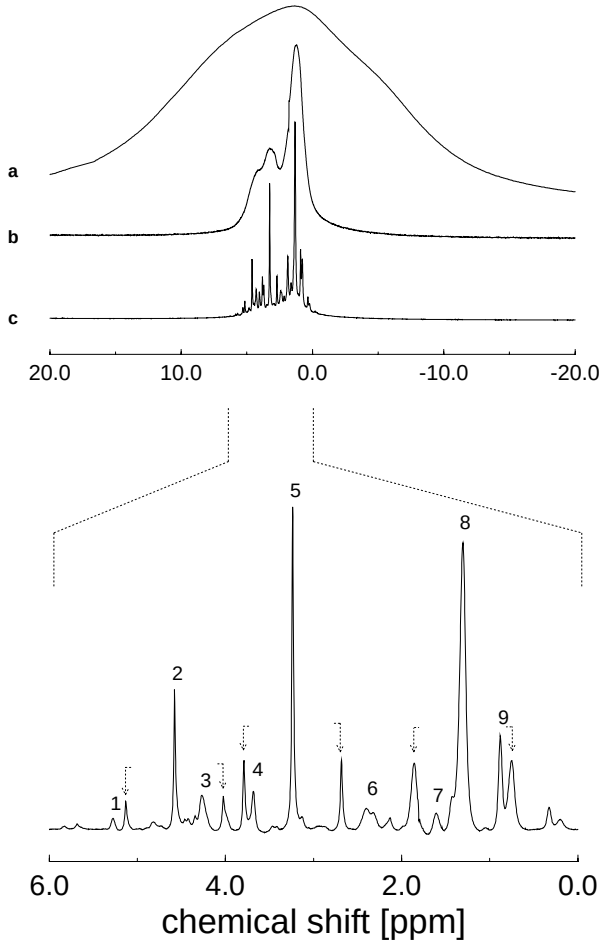

Figure 2.2: 400.13 MHz proton spectra of uniformly aligned **(b, c)** and randomly distributed **(a)** DMPC in D_2O at the magic angle and at T = 318 K. All resonances are already resolved at 220 Hz spinning speed. Static, random distribution **(a),** static, sample orientation as in Fig.1 **(b),** same as **(b)** but at 220 Hz spinning speed **(c)**. Spectrum **(c)** is shown below on an expanded horizontal scale (for resonance assignment and linewidth see Table 1). Sidebands are labelled by arrows. An exponential linebroadening of 1 Hz was applied. 128 scans were acquired with a recycle delay of 2 sec.

Peak	Group Assignment	linewidth $\Delta\nu_{1/2}[Hz]$
1	CH	16
2	HDO	9
3	α-CH_2	29
4	β-CH_2	20
5	γ-$N(CH_3)_3$	9
6	$CH_2\underline{CH_2}COO$	25/16
7	$\underline{CH_2}CH_2COO$	30
8	$(CH_2)_n$	29
9	CH_3	19

Table 2.1: Assignment of proton resonances for DMPC with linewidth obtained by magic angle oriented sample spinning (MAOSS).

the aromatic region obtained from a oriented sample at $\omega_r = 3000$ Hz. The protein/lipid mole ratio in both cases was between 1:15 and 1:20. Some resonances can be resolved in the oriented sample (Fig.2.3c), which can not be seen using high-speed MAS (Fig.2.3b).

2.4 Discussion

2.4.1 Dipolar Coupling

In order to understand the considerable ^{1}H resolution enhancement observed in MAOSS experiments, we have to consider the special dynamic situation in lipid membranes, as well as the macroscopic sample geometry as illustrated in Fig.2.1. As discussed in the introduction section, dipolar interactions would vanish under highspeed MAS conditions. However, in lipid membranes, three motional modes can be found [69]: internal motions (trans-gauche isomerisation, $\tau_j \sim 10^{-11}$ sec), intermolecular motions (rotational diffusion about long axis $\tau_{R\|} \sim 10^{-10}$ sec, and "wobbling" of long axis $\tau_{R\perp} \sim 10^{-9}$ sec) and collective motions where the whole membrane undergoes undulations [70],[71] ($10^{-3}\ldots10^{-6}$ sec). As suggested by Davis [62], placing oriented membranes in their fluid phase with all local membrane normals at the magic angle would produce considerable ^{1}H resolution enhancement in biomembranes, since the membrane normal is the axis of symmetry of the highly anisotropic intermolecular motions, and all dipolar couplings would be projected onto this axis and therefore vanish. This situation is illustrated in Fig.2.2b, where a dramatic line-narrowing is achieved, but no lines can be resolved, which is probably the reason, why this approach was not pursued and more effort went into using ultra-high speeds and high fields when exploiting protons for biomembrane studies [62, 63, 65, 67]. However, the main

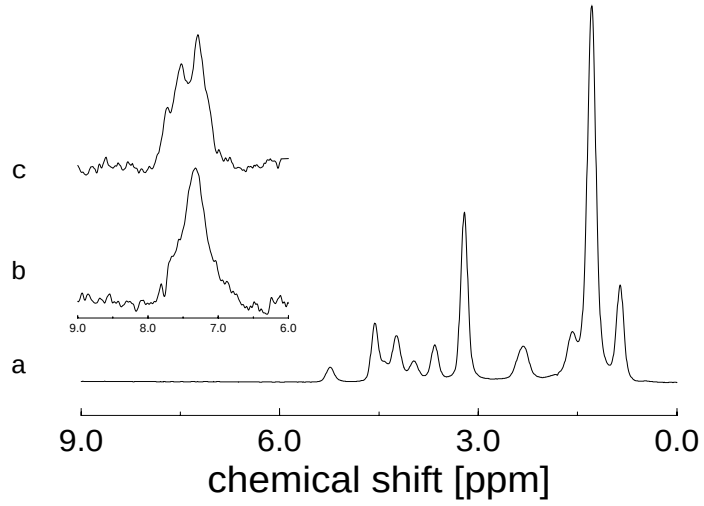

Figure 2.3: ^{1}H MAS spectrum of a "powder-type" sample of DMPC containing 2mg M13 coat protein at a lipid/protein ratio of 15:1 under similar conditions as Fig.2 but at a spinning rate of 10000 Hz **(a)**. The inset shows a comparison of the aromatic region of M13 obtained under high speed MAS condition **(b)** and with oriented sample spinning **(c)**. An exponential linebroadening of 10 Hz was applied. 5000 scans were acquired with a recycle delay of 2 sec.

cause for the residual line-broadening in Fig.2.2b is due to deviation from perfect uniform alignment. In a perfectly oriented membrane (mosaic spread $\Delta\beta = 0^o$), every single lipid molecule would rotate with a long axis correlation time of 10^{-10} sec about the magic angle. In this situation, no dipolar broadening would be expected. However, in the real experimental situation, it is impossible to prepare oriented membrane multi-layers of this sufficiently high quality and low mosaic spread with $\Delta\beta = \pm$1-3^o being the best which can normally be achieved routinely [55] (see Fig.2.4).

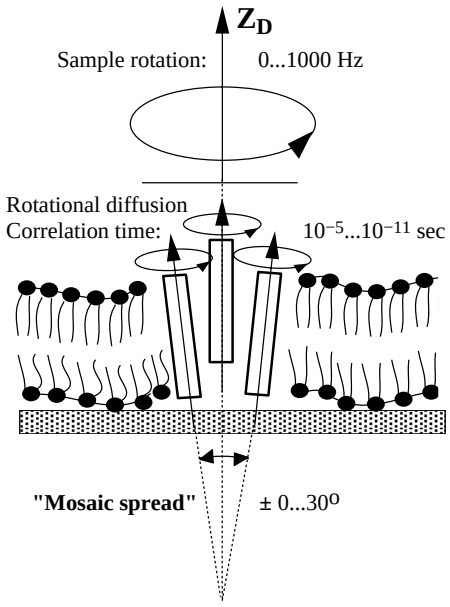

Figure 2.4: Orientational defects ("mosaic spread" $\Delta\beta = \pm 0...30^o$) cause deviations of each molecular rotation axis $\mathbf{Z_M}$ from the bilayer normal $\mathbf{Z_D}$ and so from the magic angle. However, the mosaic spread can be easily averaged by additional slow macroscopic sample rotation about the magic angle.

For a quantification of the observed effects, only the methylene groups in the lipid acyl chain are considered in the following. Both protons are strongly coupled (r_{12}=0.17 nm, $b_{II}/2\pi$= 24400 Hz), so that in first order a two spin approximation for the simulation of ^{1}H-MAS spectra can be applied [58]. Using $\Delta\beta$ and $S^{mol}_{CH_2}$, the segmental order parameter, the Hamiltonian 2.1 can be modified taking mosaic spread and dynamics into account:

$$\langle \mathcal{H}_D \rangle = \frac{\gamma_{1H}^2 \hbar}{2r_{12}^3} \left(3\cos^2(\beta_{PL} - \Delta\beta) - 1\right) (3I_{1Z}I_{2Z} - \mathbf{I}_1\mathbf{I}_2) \times S^{mol}_{CH_2} \qquad (2.3)$$

All anisotropic interactions are scaled with $S_{CH_2}^{mol} \sim 0.4...0.5$ [72],[73]. The size of the chemical shift tensor is approximately $\sigma_{11} = -4$ ppm, $\sigma_{22} = 0$ ppm, $\sigma_{33} = 4$ ppm, and is symmetrically oriented along the CH bond [15], while the dipolar coupling tensor is symmetrical ($\eta = 0$) with its z-axis along the internuclear connecting vector (see Fig.2.5). Simulations were performed in Floquet space (15x15) using the programme described in Appendix B. The mosaic spread was included with a spherical weighting function. Contributions from the chemical shift anisotropy were neglected, since they were 15 times smaller than the dipolar coupling. All interactions are projected onto the lipid long axis $\mathbf{Z_M}$, which is simulated by setting all coordinate transformations from the principal axis systems into the molecular reference frame to $\Omega_{PM}^{II,CS} = \{0, 0, 0\}$. Spectrum (a) in Fig.2.5 shows the expected Pake pattern for an unoriented, dipolar coupled spin pair. The spectrum narrows dramatically in the oriented system with a mosaic spread of $\Delta\beta = \pm 4^o$ (b_1) and even more at $\Delta\beta = \pm 1^o$ (b_2). Finally, resonance lines can be resolved by slow sample spinning at 220 Hz (c), which agrees well with the experimental findings. The comparison between experimental and simulated data in Fig.2.5 shows, that also correct sideband intensities were obtained, which means that the assumptions made above were correct. These sideband intensities arise from very small residual dipolar couplings, which illustrates that a highly efficient MAS averaging process - provided by molecular dynamics in the GHz range - takes place.

2.4.2 Slow Motions

The dynamics in lipid membranes is rather complex and covers time scales from 10^{-3} to 10^{-10} sec [74]. Here, it has been demonstrated how to utilise rotational diffusion for resolution ^{1}H enhancement. Apart from dipolar coupling and chemical shift anisotropy, especially slow and intermediate time scale motions in the frequency range of 10^{-3} to 10^{-6} sec in lipids were identified by Davis [62] as another essential cause for line-broadening. The contribution of an intermediate time scale motion with correlation times τ_c to the linewidth of a MAS resonance line at a speed of ω_r, has been discussed by Maricq and Waugh [20], and can be estimated by [75, 62]:

$$\frac{1}{T_2^{rot}} = \frac{\Delta M_2}{3\pi}\left(\frac{2\tau_c}{1+(\omega_r\tau_c)^2} + \frac{\tau_c}{1+4(\omega_r\tau_c)^2}\right) \tag{2.4}$$

where ΔM_2 is the dipolar second moment being modulated by dynamic processes. These low frequency fluctuations would cause additional line broadening. However, fluctuations in the orientation of the local bilayer normal, for example in form of undulations of the bilayer surface are mechanically suppressed in macroscopically oriented multi-layers. The motional freedom along the bilayer normal is restricted due to the solid support and due to the small interbilayer space caused by the absence of a large amount of free water (see Fig.2.5).

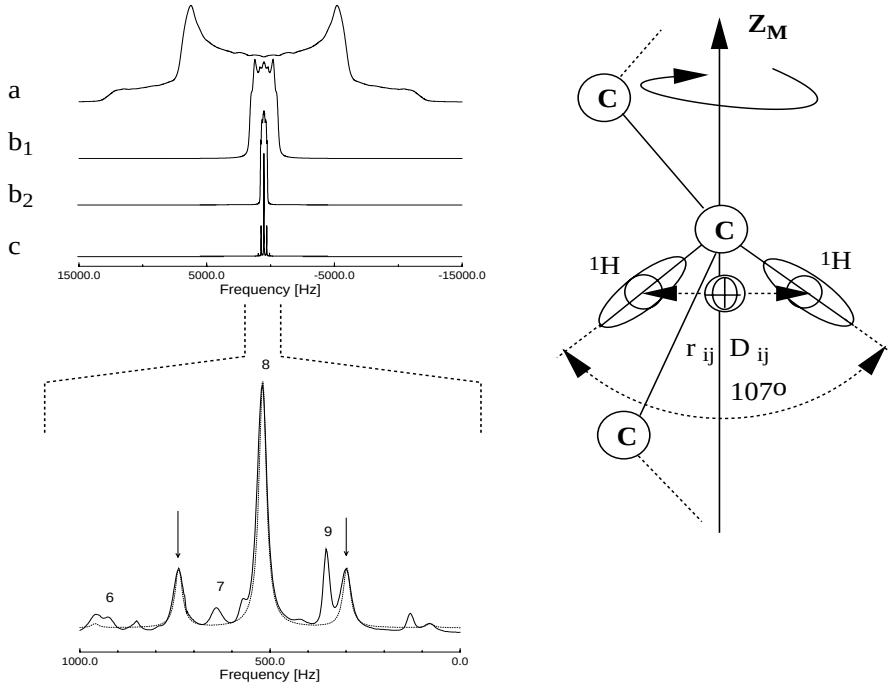

Figure 2.5: Two-spin simulation of ^{1}H spectra for a -CH_2- group in the lipid chain for the static and unoriented case (a), static and oriented with a mosaic spread of $\Delta\beta = \pm 4^o$ (b_1), $\Delta\beta = \pm 1^o$ (b_2) and at 220 Hz spinning speed and $\pm 1^o$(c). The expanded plot overlays the simulated and experimentally obtained -CH_2- resonance.

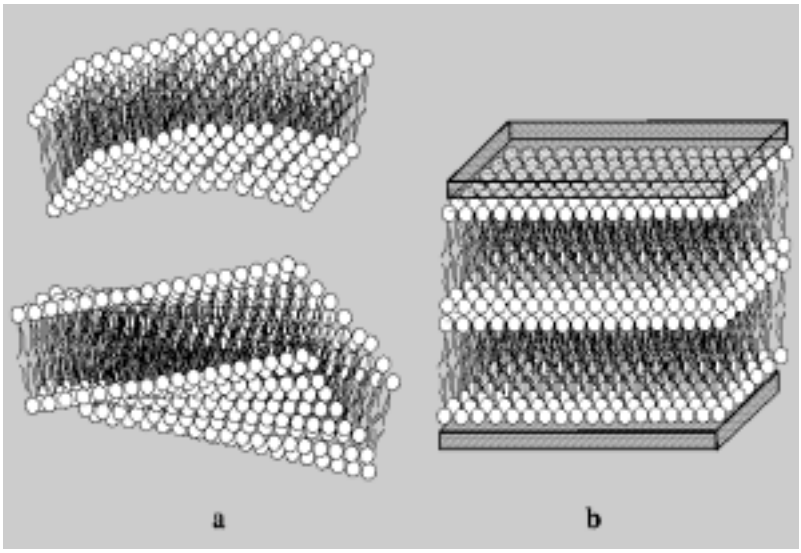

Figure 2.6: Slow, collective motions (a) in multilamellar lipid dispersions cause additional linebroadening due to T_2 relaxation effects. These motions are mechanically restricted in oriented bilayers on a solid substratum (b).

The method presented here uses rotational diffusion (in the GHz range) for averaging dipolar couplings together with macroscopic sample spinning ($\sim$ 1 kHz) for averaging orientational defects while at the same time low frequency dynamics (undulations), which would cause additional line-broadening, are suppressed.

Even higher proton resolution can be achieved using MAOSS by applying higher fields, homonuclear decoupling techniques [24] and by improving the spinning and shimming properties of the MAS rotors. Shimming especially becomes critical in the experiment with a linewidth for γ-N$(CH_3)_3$ of 9 Hz where the best proton resolution which can be achieved with solvents with the MAS probe used here was 7 Hz. It has been discussed by Pampel and Volke [65], that the sample geometry is crucial for a narrow linewidth due to the shimming properties of MAS probes [76]. Spinning speed instabilities can also cause additional linebroadening.

To demonstrate the applicability to membrane embedded proteins and peptides the 50 amino acid long M13 coat protein has been studied in a first attempt to apply MAOSS to larger systems. M13 has the primary sequence N-AEGDD PAKAA FNSLQ ASATE YIGYA WAMVV VIVGA TIGIK LFKKF TSKAS-C. It exists in the filamentous bacteriophage as a cytoplasmic protein, as a structural element and as an integral membrane protein at different stages of the phage life cycle. Residues 21-39 form the hydrophobic core. M13 is an interesting test case, since it can be well oriented and is well characterized [40, 68, 77, 78, 79, 80]. Also, Opella and co-workers have carried out extensive and detailed multi-nuclear

solution and solid-state NMR on the coat protein of the very similar phage fd [81, 82, 83, 84]. M13 differs in only one residue from the fd coat protein. As described in the results section, some spectral structures in the aromatic region can be resolved by MAS at 3000 Hz on oriented M13 samples which could not be resolved by spinning a multi-lamellar dispersion at 10000 Hz (Fig.2.3). However, M13 does not undergo rapid reorientations in a membrane [85, 79, 84, 86],but, as in oriented lipid samples, slow motions are suppressed, which helps to achieve a resolution enhancement. Also, it has been shown that the sidechains of aromatic residues are relatively flexible. Sykes and co-workers [86] studied M13 coat protein reconstituted into phospholipid vesicles and found by ^{19}F NMR, that the aromatic rings in ^{19}F-labelled residues Tyr-21, Tyr-24 and Phe-11, Phe-42 and Phe-45 rotate freely about the C_β-Cγ bond by $\sim 4\times10^8$ s^{-1}while a "wobbling" about C_α-C_β with $\sim 2\times10^8$ s^{-1}is restricted within a range of 75^o-90^o . The high mobility determined is in good agreement with ^{1}H and ^{13}C studies of the aromatic residues of fd coat protein by Cross and Opella [83]. These reorientations would project ^{1}H-^{1}H dipolar couplings onto the axis of symmetry and could finally be averaged by MAS. A similar case to the situation in fluid oriented lipids would occur if the aromatic ring rotates about the magic angle, which would require that the C_β-Cγ bond vector lies parallel to the membrane normal. However, the average orientation of this vector is not known. As discussed earlier, the dynamic situation is not different from a multilamellar dispersion except that slow motions are suppressed. It is rather difficult and beyond the scope of this study to assign any resonances in Fig.2.3c to aromatic groups because each group features a different, and highly anisotropic motion which is reflected in the lineshape. There is also a strong pH dependence for the isotropic chemical shifts of these groups which could influence the lineshape [83]. However, the fact that an improvement in resolution could be achieved underlines how slow motions can broaden ^{1}H MAS lines from biomembranes.

A much more favourable case would be the application of this method to peptides or protein fragments which undergo fast long axis reorientations. All points made about lipids would apply here and a good proton resolution is expected.

2.4.3 Sample Stability

As discussed before, a high mobility of membrane components is necessary for the success of a ^{1}H-MAOSS experiment, which gives rise to some concern regarding sample stability under conditions of MAS. The sample orientation under spinning conditions was checked after each spinning experiment by comparison of static ^{1}H and ^{31}P spectra, which were recorded before and after spinning. Even after some hours spinning, no linebroadening could be observed which gives rise to the conclusion that the lipid/protein samples are stably aligned on the glass discs in the rotor. Static proton spectra oriented at the magic angle should be sensitive to changes in the alignment due to linebroadening caused by resid-

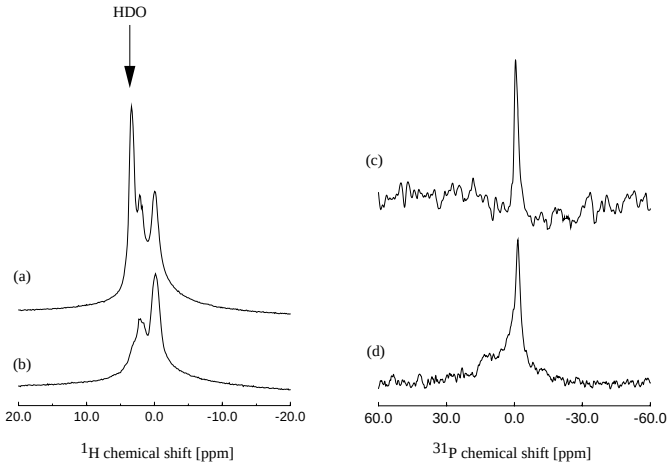

Figure 2.7: Static ^{1}H and ^{31}P spectra of oriented DMPC multilayers at T=300K before (a,c) and after 4 hours sample rotation (b,d). The ^{1}H linewidth did not increase, but changes in the degree of hydration have been monitored (arrow) for ^{1}H (b). For ^{31}P, some unoriented components can be seen (d). No changes occur, when the sample is frozen during sample rotation.

ual dipolar coupling of poorly or unoriented membrane components (Eqn.2.3). Fig.2.7 compares static ^{1}H and ^{31}P spectra of oriented DMPC hydrated with H_2O/D_2O prior and after 4 hours spinning at 1000 Hz at room temperature. Although the intensity of the water peak decreases, which indicates de-hydration, the overall spectrum is not essentially broadened, i.e. the membrane is relatively stable aligned on its solid support. This surprising stability can be explained by considering the forces, which actually apply. A lipid located at the disc edge (r_{disk}=2.7mm, $M_{lipid}=1.16 \times 10^{-24}$kg) would experience a centrifugal force $F_c = mr\omega^2 = 3.09 \times 10^{-18}$ N at 5000 Hz spinning speed.

The effect this centrifugation would have can be estimated by considering the elastic properties of model membranes. The response of the bilayer surface A to an isotropic tension T (here centrifugal force), is specified by the isothermal modulus of surface compressibility[9]:

$$K_A = A\left(\frac{\partial T}{\partial A}\right)_T \tag{2.5}$$

with typical values of $K_A = 0.14$ N/m. Accordingly, the bulk area compressibility modulus for a bilayer thickness of $d_t = 4$ nm is $K_A/d_t = 3 \times 10^{-7}$ N/m^2 [9]. This means, that a single lipid of 2 nm length and 0.5 nm^2 cross sectional

area would need to experience a lateral force of $5 \times 10^{-11} N$ to be removed from the bilayer. This force is much larger than the applied centrifugal force and explains the observed sample stability together with effects of surface roughness and cohesion/adhesion interaction between the membrane and the glass surface.

In an experimental situation however, many thousands of bilayers are placed on top of each other, which causes some instabilities, since interaction between bilayers are relatively weak. Experience shows that a better sample stability is achieved for thinner sample layers.

Stability issues as well as de-hydration effects can be overcome efficiently by sample freezing, which is also useful for studying anisotropic interactions, as discussed in the following chapters.

2.5 Conclusions

The applicability of ^{1}H-MAS to uniformly aligned biomembranes has been demonstrated. By placing the sample with the membrane normal parallel to the rotor axis, molecular long axis rotations occur about the magic angle, with correlation times ranging from 10^{-10} sec for lipids [69] to 10^{-5} sec for some large proteins such as rhodopsin [87], which could enhance the MAS averaging process and so produce dramatic resolution improvement. This is in some way a two-dimensional anisotropic equivalent to liquid-state NMR where molecular motions are essential for obtaining sufficient resolution. The suppression of slow collective motions (10^{-3}-10^{-6} sec) in oriented membranes is of additional help, since it has been shown to be one reason for unexpected low resolution in high speed MAS experiments. These two last points offer the opportunity to obtain proton NMR spectra from peptides and protein fragments with sufficient resolution in order to start structural studies.

In order to use all of these advantages at a full scale, some technical improvements have to be made. For example using thinner glass discs would allow positioning the whole sample volume in the middle of the rotor to achieve better shimming properties and higher B_1 homogeneity. Combinations with homonuclear decoupling techniques can also be expected to contribute to an increase in spectral resolution.

Chapter 3

MAS Spinning Sidebands from low-abundant Nuclei in Oriented Systems: Simulations and Examples

Abstract

Spinning sidebands can be observed in MAS spectra governed by inhomogeneous interactions such as chemical shift or quadrupole coupling, if the spinning speed is not exceeding the anisotropy of these tensors. In ordered systems, such as oriented membranes, sideband intensities can be utilized for determining tilt angles or orientation distribution functions. The advantage of using MAS rather than static NMR for studying ordered systems is mainly found in a remarkable increase in higher sensitivity and spectral resolution. Here, the special physical and geometrical situation in uniformly aligned membranes is analysed for deriving an algorithm to simulate orientational dependent spinning sideband pattern.

The determination of the tilt angle of lipid acyl chains in dimyristoylphosphatidylcholine (DMPC) bilayers in the gel phase from a ^{13}C MAOSS sideband pattern illustrates the applicability of this approach.

3.1 Theoretical Background

3.1.1 MAS on Oriented Membranes

The application of MAS to ordered or partially ordered solids has been used successfully for studying the degree of order in polymers [21] or for investigating the orientational distribution function of the ^{31}P chemical shift tensor in DNA fibres [88]. The major advantage of investigating order phenomena by MAS rather

than static NMR, is a much higher spectral sensitivity and resolution, which makes it especially attractive for systems with a lower degree of order and/or many different sites, such as a large protein in a lipid bilayer. It is necessary to discuss the variety of macroscopic and microscopic orientational distributions in ordered membranes in order to be able to extract structural information from NMR spectra. Since a rather detailed analysis of distributions for static ^{2}H-NMR on lipid membranes has been published by Seelig [73], only the points needed to understand the specific situation of a MAOSS experiment, as illustrated in Fig.1.6, will be discussed below.

The sample fixed coordinate system DF is identical with the rotor system RF, i.e. the rotor axis is parallel to the membrane normal ($\beta_{DR} = 0^o$, see Fig.1.2 and Fig.1.6). The oriented membrane itself is a transverse isotropic system. The z-axis Z_M of the molecular frame and the z-axis Z_P of the principal axis system of the NMR interaction in Fig.3.1 are uniaxially distributed about the membrane normal Z_D. This double uniaxiality has direct consequences for the MAS signal. Under conditions of sample spinning, all values of γ_{PR}, which describes rotation of the NMR interaction about the rotor axis, would have the same probability. The expression for the calculation of sideband intensities $I_N(\alpha_{PR}, \beta_{PR}, \gamma_{PR})$ (Eqn.1.30) can now be simplified by integrating over γ_{PR} [21]:

$$\begin{aligned} I_N(\alpha_{PR}, \beta_{PR}) &= \int_0^{2\pi} \frac{d\gamma_{PR}}{2\pi} I_N(\alpha_{PR}, \beta_{PR}, \gamma_{PR}) \qquad (3.1) \\ &= \int_0^{2\pi} \frac{d\gamma_{PR}}{2\pi} f^*(\alpha_{PR}, \beta_{PR}, \gamma_{PR}) e^{i\gamma_{PR}N} F_N(\alpha_{PR}, \beta_{PR}, \gamma_{PR}) \end{aligned}$$

which simplifies by using the definition for F_N from Chapter 1 to:

$$I_N(\alpha_{PR}, \beta_{PR}) = F_N(\alpha_{PR}, \beta_{PR}) F_N^*(\alpha_{PR}, \beta_{PR}) \qquad (3.2)$$

This means I_N is always a real number and so only absorptive sidebands will be observed. It has been pointed out that this is true for any sample which is subject to unsynchronized, random data acquisition [21].

Since both coordinate systems, PAS and MF, are uniaxially distributed about the rotor axis, some further considerations have to be made. The set of Euler angles Ω_{PR} needed to rotate an interaction tensor from its PAS into the rotor frame RF, can actually be described as an addition of two rotations, namely from the PAS onto the molecular fixed frame MF and from there into the membrane fixed coordinate system DF (see Fig.1.2 for definitions).

The molecular frame can be defined by assigning its z axis Z_M to the helix or lipid chain long axis, while the orientation of the PAS depends usually on the type of interaction and the chemical groups involved. For deuterium for example, the

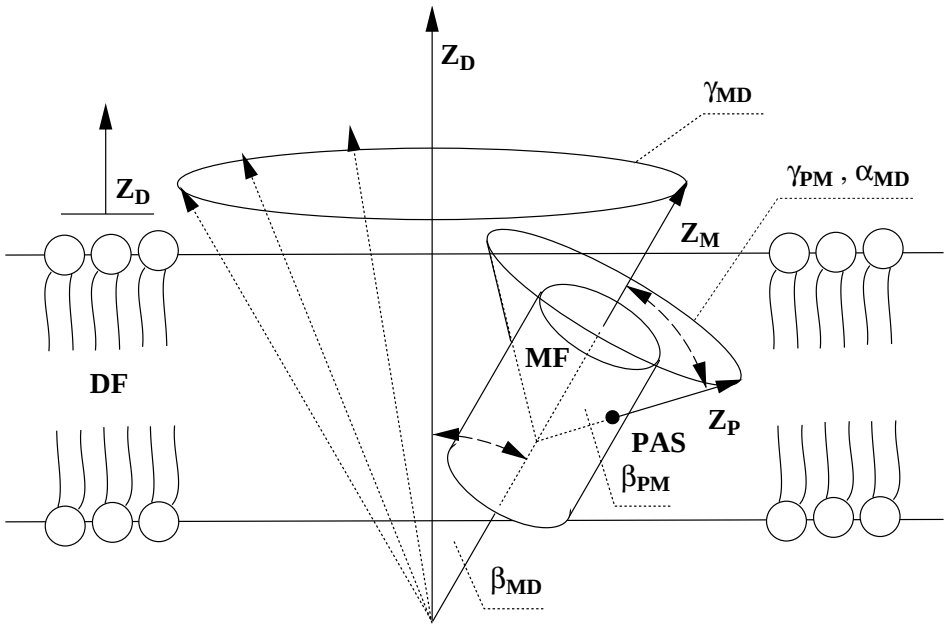

Figure 3.1: Distribution of molecular long axis Z_M and z-axis of PAS Z_P about membrane normal Z_D. Both distributions are uniaxial but not identical. The angles α_{MD} and γ_{PM} describe rotations about the same axis.

z-axis Z_P is along the C-^{2}H bond. As illustrated in Fig.3.1, the angles γ_{PM} and α_{MD} describe rotations about the same axis Z_M, which is the final z-axis while rotating from PAS to MF and at the same time the initial z-axis for the rotation from MF to DF. Finally, only one rotation about Z_M by an angle $\gamma_{PM}+\alpha_{MD}$ takes place, which allows a null point to be chosen, with either $\gamma_{PM} = 0$ or $\alpha_{MD} = 0$. Here, $\gamma_{PM} = 0$ will be used. To account for the two uniaxial distributions of PAS and MF with respect to membrane normal, averages over γ_{PM} or α_{MD} and γ_{MD} have to be performed. Since DF is identical to RF, all rotations below will now refer directly to the rotor frame rather than to the sample fixed coordinate system. Eqn.3.2 is valid for any set of Euler angles which rotate a molecule fixed coordinate system into the rotor frame, but for clarity, complete integral expressions will be given here:

$$I_N(\alpha_{PM}, \beta_{PM}, \beta_{MR}) = \int_0^{2\pi} \frac{d\alpha_{MR}}{2\pi} \int_0^{2\pi} \frac{d\gamma_{MR}}{2\pi} I_N(\alpha_{PM}, \beta_{PM}, 0, \alpha_{MR}, \beta_{MR}, \gamma_{MR}) \tag{3.3}$$

Additionally, a certain distribution of the molecular long axis Z_M with respect to the sample director Z_D has to be assumed, since it is not possible to prepare perfectly aligned proteins or lipids [46]. This degree of disorder, for which the term "mosaic spread" has been used in the literature, is best described by a Gaussian orientation distribution function of β_{MR} (same as β_{MD} in Fig.3.1):

$$ODF_{MR}(\beta_{MR}) = \frac{1}{2\pi} \exp\left[-\frac{1}{2}\frac{\beta_{MR} - \beta^0_{MR}}{\Delta\beta}\right] \tag{3.4}$$

where $\Delta\beta$ is actually the width (e.g. mosaic spread $\Delta\beta = \pm 10^o$) and β^0_{MR} the centre of the distribution. A weighting function for β_{MR} has to be introduced when simulating these distributions by planar-random averaging, because of a higher density of orientations in the pole regions. For full powder simulations, normally $p_{MR}(\beta_{MR}) = \sin\beta_{MR}$ is used. However, for describing the assumed Gaussian distribution correctly, weighting factors have to be calculated by integrating ODF_{MR} over the range of the mosaic spread. The integral over a Gaussian is known as the error function erf:

$$p_{MR}(\beta_{MR}) = \mathrm{erf}(\beta_{MR}) = \frac{2}{\sqrt{\pi}} \int_0^{\beta_{MR}} \exp\left[-t^2\right] dt \tag{3.5}$$

It is sufficient to consider for all angles β a range of $[0,\pi/2[$ since the nature of second rank tensor interaction does not allow to distinguish between β and $180^o - \beta$. For this interval, both weighting functions $\sin(\beta)$ and $\mathrm{erf}(\beta)$ are similar, as the Taylor series expansion about $\beta = 0$ illustrates:

$$\mathrm{erf}(\beta) = \beta - \frac{1}{3}\beta^3 + \frac{1}{10}\beta^5 + O(\beta) \tag{3.6}$$

$$\sin(\beta) = \beta - \frac{1}{6}\beta^3 + \frac{1}{120}\beta^5 + O(\beta) \tag{3.7}$$

which means, that it is safe in the most cases to weight sub-spectra by $\mathrm{p}_{MR}(\beta_{MR}) = \sin\beta_{MR}$. The intensity of a MAS sideband at position $\mathrm{N}\omega_r$ with respect to the centre line is now a function of two Euler angles describing the orientation of the NMR interaction tensor with respect to the molecular frame, the tilt of the molecular frame z-axis with respect to the rotor axis and the width of the distribution of molecular frame axes:

$$\begin{aligned} I_N(\alpha_{PM},\beta_{PM},\beta_{MR},\Delta\beta) &= K\int_0^{2\pi} d\alpha_{MR}\int_0^{2\pi} d\gamma_{MR}\int_{\beta_{MR}-\Delta\beta}^{\beta_{MR}+\Delta\beta} d\beta_{MR} \\ &\quad \times p_{MR}(\beta_{MR}) I_N(\alpha_{PM},\beta_{PM},\alpha_{MR},\beta_{MR},\gamma_{MR}) \end{aligned} \tag{3.8}$$

where K is a normalizing constant. A summary of all necessary reference frame rotations is shown in Fig.3.2. All averages are combined with the rotation from the molecular frame into the rotor frame, which is of advantage for numerical simulations.

If the orientation of the interaction tensor with respect to the molecular frame is known, e.g. in case of ^{2}H or ^{15}N labels in the protein backbone, MAOSS experiments can be used to determine the orientation of molecules with respect to the membrane. Alternatively, if $\mathrm{ODF}_{MR}(\beta_{MR})$ is known, orientational information about the tensor with respect to the molecule can be extracted, which is of importance for studying structure and orientation of ligands bound to membrane proteins. The orientational distribution function $\mathrm{ODF}_{PM}(\beta_{PM})$ for the latter case is a sharp, single line (δ-function), if there is no conformational disorder. For symmetrical tensors such as ^{2}H, α_{PM} can be arbitrarily chosen ($\eta = 0$). Some example simulations are given in Fig.3.3 for different orientations Ω_{PM} with constant $\mathrm{ODF}_{MR}(\beta_{MR})$ as well as for a fixed orientations and variable mosaic spread.

3.1.2 MAS Simulation by Floquet Theory

Numerical simulations of MAS spectra were performed using the NMR C++ library GAMMA and its built-in Floquet operator formalism [89],[90]. Floquet theory has been demonstrated to be very useful for analysing periodically time-dependent problems [91], which makes it a perfect tool for describing NMR experiments on rotating solids [58],[92],[93]. The major advantage is that it allows

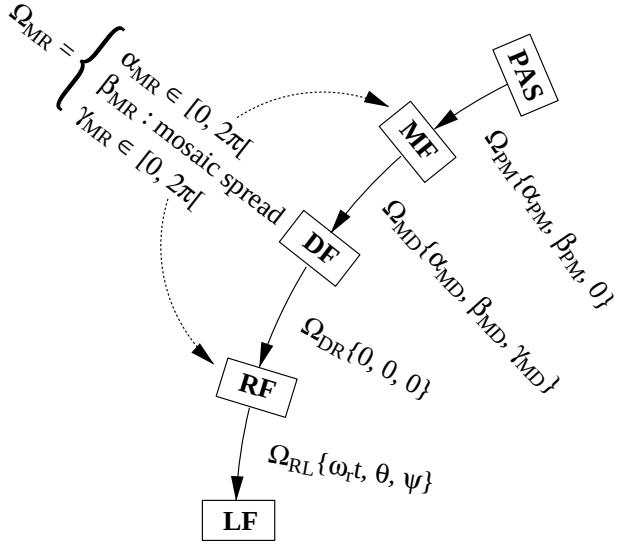

Figure 3.2: Summary of rotations and averages for simulating MAS spectra of NMR interaction for the special situation of oriented membranes. All averaging steps can be shifted into the rotation MF->RF. Here, the rotor frame RF and the sample fixed frame DF are identical.

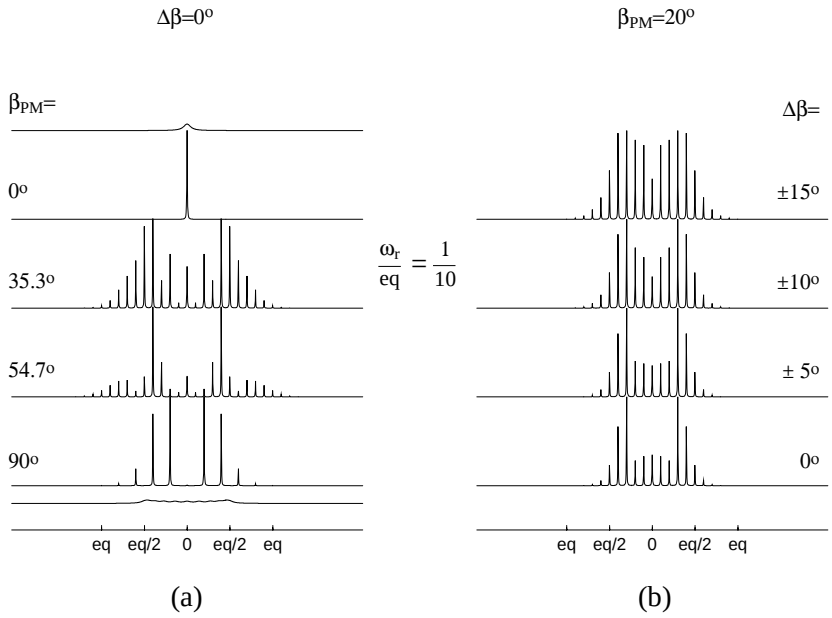

Figure 3.3: Simulations of ^{2}H-MAS spectra for different orientations of the quadrupole coupling tensor with respect to the molecular frame (a) and for different mosaic spread distributions (b). The rotation MF->RF was chosen to be $\Omega_{MR}(0, 0 \pm \Delta\beta, 0)$. The deuterium quadrupolar coupling tensor is symmetrical ($\eta = 0$), so that α_{PM} can be set to any value. Calculations were performed for a relative spinning speed ω_r/eq=0.1. All spectra are scaled to the same intensity, except the static spectra above and below $\beta_{PM} = 0^o$ and 90^o: These spectra have the same integral intensity as the MAS spectra for the same orientation and illustrate the increase in the signal/noise ratio one can expect by performing MAS experiments on oriented systems.

the description of the full time-dependence of a periodically time-dependent system, for example calculating the full sideband pattern in case of sample-spinning experiments. The time dependence can be overcome by transforming the time-dependent Hamiltonian into an infinite dimensional Hilbert space, called Floquet space. The Hamiltonian is now time-independent, but of infinite dimension, which can however be truncated for numerical computations. In many cases a 15x15 matrix is sufficient for simulations.

A time-independent Floquet space operator A_F which corresponds to the time-dependent Hilbert space operator A(t),

$$A(t) = \sum_{n=-\infty}^{n=+\infty} A_n \exp\left[in\omega t\right] \tag{3.9}$$

is defined by

$$A_F = \sum_{n,m=-\infty}^{n=+\infty} |n > A_{n-m} < m| \tag{3.10}$$

A matrix representation is constructed by inserting the non-zero operators A_n into the n-th side diagonal of A_F:

$$A_F = \begin{pmatrix} & & & m=0 & & & \\ & \vdots & \vdots & \vdots & \vdots & \vdots & \\ \cdots & A_0 & A_1 & A_2 & A_3 & A_4 & \cdots \\ \cdots & A_{-1} & A_0 & A_1 & A_2 & A_3 & \cdots \\ \cdots & A_{-2} & A_{-1} & A_0 & A_1 & A_2 & \cdots \\ \cdots & A_{-3} & A_{-2} & A_{-1} & A_0 & A_1 & \cdots \\ \cdots & A_{-4} & A_{-3} & A_{-2} & A_{-1} & A_0 & \cdots \\ & \vdots & \vdots & \vdots & \vdots & \vdots & \end{pmatrix} \quad n=0 \tag{3.11}$$

Floquet space representations for all Hilbert space operators can be constructed in that way [93].

For the case of MAS spectroscopy, i.e. single axis sample rotation, the Hamiltonian in the principal axis systems PAS is related to the laboratory frame LF by two intermediate transformations Ω_{PR} and Ω_{RL} (see Fig.1.2, Fig.3.2). According to the definitions above, the Fourier expansion of the Hamiltonian

$$\mathcal{H}(\Omega_{PR}, t) = \sum_{n=-\infty}^{n=+\infty} \mathcal{H}_n(\Omega_{PR}) \exp\left[in\omega_r t\right] \tag{3.12}$$

leads to the Floquet representation

$$\mathcal{H}_{\mathcal{F}}(\Omega_{PR}) = \sum_{n,m=-\infty}^{n=+\infty} |n > \mathcal{H}_{n-m}(\Omega_{PR}) < m| \tag{3.13}$$

The solution of the equation of motion is now given as:

$$\begin{aligned}\sigma_F(\Omega_{PR}, t_0 + t') &= \exp[-i(\mathcal{H}_{\mathcal{F}}(\Omega_{PR}) + \mathcal{W}_{\mathcal{F}}^{\omega_r})t'] \times \\ &\quad \sigma_F(\Omega_{PR}, t_0) \times \\ &\quad \exp[i(\mathcal{H}_{\mathcal{F}}(\Omega_{PR}) + \mathcal{W}_{\mathcal{F}}^{\omega_r})t']\end{aligned} \tag{3.14}$$

where $\mathcal{W}_{\mathcal{F}}^{\omega_r}$ is the frequency displacement operator with ω_r being the sample spinning speed:

$$\mathcal{W}_{\mathcal{F}}^{\omega_r} = \sum_n |n > n\omega_r < n| \tag{3.15}$$

Although $\mathcal{H}_{\mathcal{F}}$ is the correct form of the Hilbert space Hamiltonian in Floquet space, the modified operator $\mathcal{H}_{\mathcal{F}}(\Omega_{PR}) + \mathcal{W}_{\mathcal{F}}^{\omega_r}$ is usually designated as the Floquet Hamiltonian [93] which is given in its matrix representation as:

$$\mathcal{H}_{\mathcal{F}} + \mathcal{W}_{\mathcal{F}}^{\omega_r} = \begin{pmatrix} & & & m=0 & & & \\ & \vdots & \vdots & \vdots & \vdots & \vdots & \\ \cdots & \mathcal{H}_0 + 2\omega_r & \mathcal{H}_1 & \mathcal{H}_2 & \mathcal{H}_3 & \mathcal{H}_4 & \cdots \\ \cdots & \mathcal{H}_{-1} & \mathcal{H}_0 + \omega_r & \mathcal{H}_1 & \mathcal{H}_2 & \mathcal{H}_3 & \cdots \\ \cdots & \mathcal{H}_{-2} & \mathcal{H}_{-1} & \mathcal{H}_0 & \mathcal{H}_1 & \mathcal{H}_2 & \cdots \\ \cdots & \mathcal{H}_{-3} & \mathcal{H}_{-2} & \mathcal{H}_{-1} & \mathcal{H}_0 - \omega_r & \mathcal{H}_1 & \cdots \\ \cdots & \mathcal{H}_{-4} & \mathcal{H}_{-3} & \mathcal{H}_{-2} & \mathcal{H}_{-1} & \mathcal{H}_0 - 2\omega_r & \cdots \\ & \vdots & \vdots & \vdots & \vdots & \vdots & \end{pmatrix} \begin{matrix} \\ \\ \\ \\ \\ \\ \\ \end{matrix} \begin{matrix} \\ \\ \\ \\ \\ \\ n=0 \\ \end{matrix} \tag{3.16}$$

By transforming detection operator $D_F(t)$ into Floquet space and with Eqn.3.14, the NMR signal is found as [94]:

$$S(\Omega_{PR}, t) = Tr\{D_F(t)\sigma_F(\Omega_{PR}, t)\} \tag{3.17}$$

Integrations over the Euler angles have to be performed for simulating isotropic or partially ordered samples (see. Fig.3.2). Detailed descriptions and theoretical foundations can be found elsewhere [93]. The source code for the simulations used here can be found in Appendix B.

3.2 Experimental Example

3.2.1 Results

In the following, two examples will demonstrate the application of MAS on oriented membranes for sideband analysis. ^{13}C spinning sidebands from CH_2 tensors in the lipid acyl chain of DMPC are used to determine the chain's tilt angle,

while ^{31}P NMR on DMPC multilayers with different director axis orientations β_{DR} verifies the principle feasibility of sample orientations $\beta_{DR} \neq 0^o$, in the MAS rotor, which might be of importance for future studies. Sample preparation and experiments were performed as described in Chapter 2.

^{13}C: A Molecular Example

Fig.3.4 illustrates the effect of orientation dependent spinning sidebands for an example, where the molecule itself is tilted with respect to the bilayer normal, and so to the rotor frame. It has been shown by a number of spectroscopic methods such as EPR or X-ray scattering, that hydrocarbon chains in phospholipids, such as DMPC, are tilted from 0^o to 30^o with respect to the membrane normal while undergoing a phase transition from the liquid-crystalline to the gel-phase [95],[96]. This behaviour is a good test case to demonstrate the applicability of MAOSS experiments to determine molecular orientation. Fig. 3.4a and b show static spectra of oriented DMPC in the Lα (318K) and Lβ phase (280K). The corresponding spectra at a spinning rate ω_r= 1080 Hz are plotted on top of these spectra, horizontally expanded from 12 to 65 ppm in Fig.3.4c and Fig.3.4d. A peak assignment is given in the figure legend (obtained from [97]). The intensity of the methylene resonance (C_4-C_{11}) decreases while undergoing the phase transition and two strong sideband intensities (+1,-1) appear. Since the whole chain is tilted, all resonances are affected, which is the reason that the C_2, C_3, C_{12} and C_{13} resonances are losing intensity and their sidebands become too weak to be detected. The linewidth for the MAS resonance lines increases with the phase transition from 1.1 ppm in the Lα phase bilayers to 1.3 ppm in the Lβ phase bilayers and the methylene resonance (C_4-C_{11}) is shifted by 2 ppm downfield. Computer simulations (see below) overlay Fig. 3.4c and Fig. 3.4d.

^{31}P: A "Mechanical" Example

The easiest example to demonstrate orientational dependent sideband patterns in oriented lipid membranes is shown Fig.3.5. Static ^{31}P spectra are compared with those obtained at ω_r=1000 Hz spinning speed for a multilamellar dispersion of DMPC (Fig.3.5a), and oriented DMPC samples with the membrane normal parallel (Fig.3.5b) and perpendicular (Fig.3.5c) to the rotor axis. The two different orientations were achieved by placing glass discs parallel and perpendicular to the symmetry axis of the MAS rotor. The isotropic line is labelled in each spectrum. The experiments were performed with the lipids in their fluid (Lα) phase. The static spectra of oriented samples suggest a mosaic spread of $\Delta\beta$=$\pm 4^o$ and the linewidth in these spectra is $\Delta\nu_{1/2}$=3 ppm, while isotropic line and spinning sidebands of the corresponding MAS spectra are narrowed to 1 ppm. The differences in the signal/noise between multilamellar dispersion and oriented samples is due to the fact that only five glass disks, each carrying 0.1mg material, were

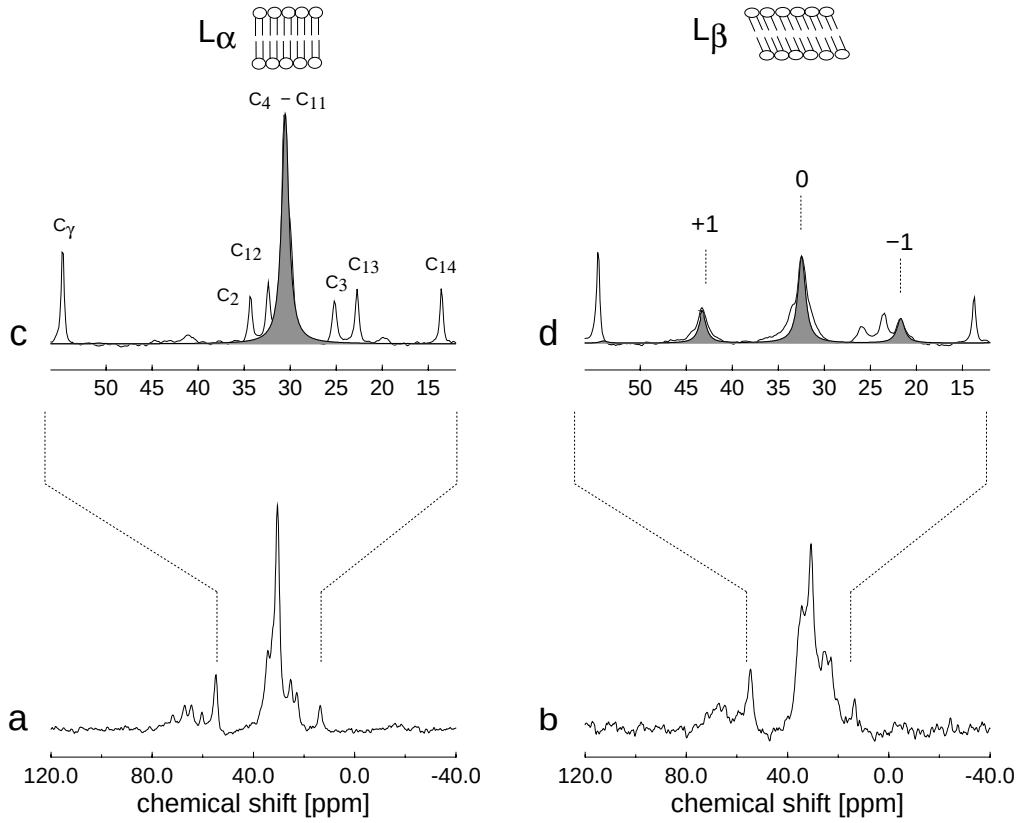

Figure 3.4: ^{13} C NMR spectra of uniformly aligned DMPC with the membrane normal parallel to the rotor axis. The acyl chains in DMPC are tilted from 0^o to 30^o while undergoing a phase transition from the Lα to the Lβ phase which is reflected in a change of the sideband pattern of the methylene group (C_4 - C_{11} in spectrum **(c)**). Static spectrum at T = 318K (Lα) **(a)**, **s**tatic spectrum at T = 280K (Lβ) **(b),** same as **(a)** but at ω_r = 1080 Hz (c), same as (b) but at ω_r = 1080 Hz (d).The shaded peaks are computer simulations for the two different orientations. Resonances C_2- C_{14} in spectrum (c) are from the fatty acyl chains and Cγ from choline-Cγ in the polar head group (assignment from [97]). 4096 scans were acquired with a recycle delay of 2 sec. The chemical shift is scaled with respect to TMS.

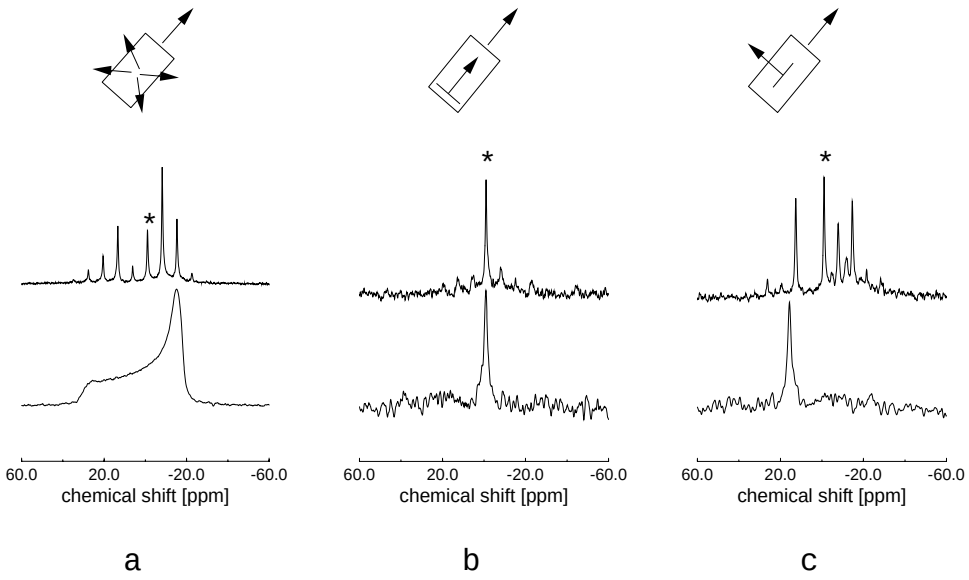

Figure 3.5: ^{31}P NMR spectra of DMPC at 318K with different orientational distributions. All MAS spectra (upper spectra) were recorded at ω_r = 1000 Hz. Static (lower spectra) and MAS spectra of DMPC with a random orientational distribution ("powder") **(a)**, static and MAS spectra of DMPC with the membrane normal parallel **(b)** and perpendicular **(c)** to the rotor axis. 2048 scans were acquired with a recycle delay of 2 sec. The chemical shift is scaled with respect to phosphoric acid.

used for these experiments. The sideband pattern changes dramatically by tilting the membrane normal mechanically from a parallel to perpendicular position with respect to the MAS rotor axis. The sideband pattern in Fig.3.5 a is the superposition of all possible orientations ("powder").

3.2.2 Discussion

^{13}C: The Molecular Example

The tilt of the lipid chains in the Lβ (gel) phase with respect to the bilayer normal is well established [95]. Fig.3.4 shows a dramatic change in the ^{13}C MAOSS sideband pattern, for the lipid when above and below the fluid Lα and gel Lβ phase transition. In order to be able to extract the chain tilt angle, the changes in the dynamic situation which would be reflected in a different chemical shift anisotropy need to be considered. The chemical shift anisotropy and asymmetry parameter from sideband intensities of low speed spectra of multi-lamellar dispersions of DMPC in both phases (spectra not shown), have been determined

for the Lα $\{\delta = 1000$ Hz$, \eta = 0.7\}$ and for the Lβ $\{\delta = 1750$ Hz$, \eta = 0.7\}$ phases. For the methylene ^{13}C chemical shift tensor from n-$C_{20}H_{42}$ crystals $\omega_{aniso} = 1800$ Hz and $\eta = 0.66$ has been found [98]. The overall correlation time as determined by ^{2}H NMR by Weisz et al. [69] changes from $\tau_{\|} = 10^{-10}$ sec for Lα to $\tau_{\|} = 10^{-7} - 10^{-6}$ sec in Lβ, which explains the slight broadening of the MAS resonance lines (Eq. 2.4 in Chapter 2 applies here as well). Fig.3.6 defines the reference frames which are used to define the rotation of the ^{13}C chemical shift tensor (CST) of methylene into the rotor fixed coordinate system. The principal axis system PAS of the CST coincides with the vector joining both protons from the same CH_2 unit (**x**), the bi-sector of the H-C-H bond in the plane of these atoms (**y**) and the chain direction (**z**) [98],[99]. Therefore, the set of Euler angles needed to perform a rotation from the **PAS** into the molecular reference frame **MF** is $\{\alpha_{PM} = 0, \beta_{PM} = 0, \gamma_{PM} = 0\}$. A second set of Euler angles relates **MF** to the rotor fixed coordinate system **RF** which is identical with the bilayer system, that is, the membrane normal is parallel to the rotor axis. As discussed before, the bilayer exhibits transverse isotropy, since it is macroscopically and microscopically uniaxial. The only free angle is β_{MR} which describes the tilt of the chain to the membrane normal and for the spectral simulations averages over α_{MR} and γ_{MR} have to be performed.

In order to make sure that the appearance of sidebands in Fig. 3.4d is not caused only by the increased chemical shift anisotropy, sideband intensities from low speed spectra of multi-lamellar dispersions can be compared with those from oriented samples. In the gel phase, the intensity of sideband **+1** increases from 0.17 in the powder to 0.36 in the oriented system and **-1** increases from 0.09 to 0.18 (relative area intensities to the normalized isotropic line). In the fluid phase however, intensities decrease slightly from 0.06 to 0.05 and 0.02 to 0.013 for **+1** and **-1** in powder and oriented system, respectively. These differences are due to the macroscopic order in the sample. Lineshape simulations have been performed for both data in Fig.3.4c and 3.4d and the best fits are shown over the experimental data. Fig.3.7 shows a series of calculations for the tilt angle $\beta_{MR} = 25^o \ldots 35^o$ in steps of 1^o for a data set corresponding to the Lβ phase. At $\beta_{MR} = 0^o$, sideband intensities would nearly vanish and the isotropic line only could be observed. Taking mosaic spread and signal/noise into account a molecular tilt of $\beta_{MR} = 33^o \pm 6^o$ is obtained, which is a reasonable result compared to the published tilt of 30^o [95].

This experiment shows that the orientation of membrane components can be measured with the MAOSS method, and by applying sophisticated multi-dimensional sideband separation techniques, the orientational distribution functions of more complex systems such as peptides or proteins can be potentially studied [21].

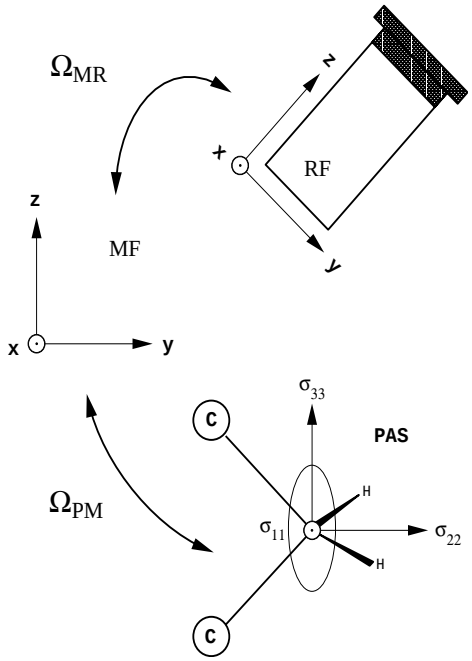

Figure 3.6: Hierarchy of reference frames used for data analysis: The molecule fixed coordinate system (MF) has been chosen to be identical with the principal axis system (PAS) for the chemical shift tensor of the methylenes C_4 - C_{11} (Fig.3.4) with the z axis being the chain direction. A set of three Euler angles describes the transformation Ω_{MR} from MF into the rotor fixed system RF which is identical with the membrane system.

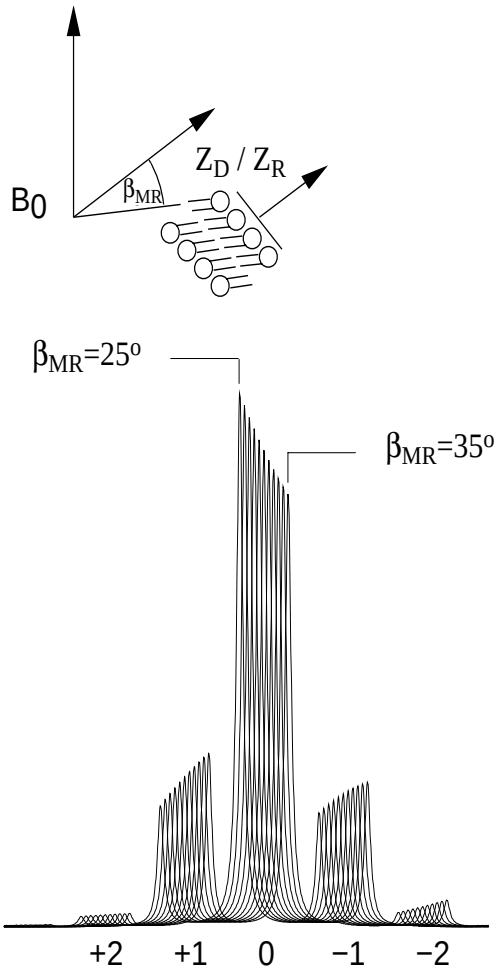

Figure 3.7: Computer simulation as shown in Fig.3.4 for a range of different tilt angles β_{MR} from 25^o to 35^o in 1^o steps. Sideband intensities vanish for β_{MR}=0^o.

^{31}P: The "Mechanical" Example

Placing the membrane normal parallel to the rotor axis has a number of advantages over a perpendicular setup. A much better sample filling factor can be achieved by placing disks on top of each other into a round MAS rotor, and the mechanical spinning properties are easier to control in such a symmetrical sample alignment.

However, it is important to show that in principle other sample director orientations are experimentally possible as well. The assumption made before, that all angles γ_{PR} would have the same probability, is no longer valid if $\beta_{DR} \neq 0^o$, because the sample would not be transverse isotropic about the rotor axis. A number of studies have addressed this situation using rotor synchronised two-dimensional MAS spectroscopy mainly for polymer studies and also DNA fibres [21],[88],[100]. These experiments represent a rather direct approach to study the degree of order, although direct analysis in terms of individual angles is difficult and a moment expansion has to be applied [21].

The work presented here uses exclusively unsynchronized sampling and $\beta_{DR} = 0^o$ with the analysis discussed before, but future applications will include synchronized-MAS 2D experiments.

3.3 Conclusions-Future Perspective

The theoretical foundations and experimental examples for MAS applications to uniformly aligned biomembranes using low-γ nuclei ^{13}C and ^{31}P has been demonstrated. The advantage of this method over static NMR spectroscopy on oriented membranes is founded in the fact that deviations from perfect macroscopic orientation ("mosaic spread"), which would prevent well resolved spectra, can be averaged by spinning at low speeds ($<$ 1 KHz). The orientational information which can be obtained from MAS on samples with a powder-type distribution, is limited to relative orientations of tensors with respect to each other, for example in the form of torsional and dihedral angles [101, 102, 103]. However, in this new approach, additional information about orientation with respect to the bilayer normal can be obtained from analysing the spinning sideband patterns. Problems to be addressed are either the orientation for proteins with respect to the membrane or the orientation of certain chemical groups, e.g. ligands, with respect to the protein can be measured. Both cases are discussed in the next chapters for ^{2}H MAS spectroscopy on oriented bacteriorhodopsin and ^{13}C MAS on oriented M13 coat protein.

Chapter 4

Deuterium-MAS Spectroscopy on [18-CD_3]-Retinal in Oriented Bacteriorhodopsin

Abstract

Deuterium MAS spectroscopy is introduced as a new tool for obtaining orientation information of functional groups in membrane proteins, which is illustrated by an application to [18-CD_3]-retinal in oriented bacteriorhodopsin. The main advantage of this approach is a great spectral sensitivity, which allows to obtain reliable data from lower deuterium concentrations compared to static wideline NMR. A detailed data and error analysis has been performed. It is shown, that the problem of tilt angle ambiguities by ^{2}H-NMR, can be solved by spectral intensity simulations and by analysing MAS spectra at different spinning speeds. The angle between the C5-C18 bond vector Z_P and the protein main axis Z_M was determined to $\beta_{PM} = 36^\circ \pm 5^\circ$.

4.1 Bacteriorhodopsin

Bacteriorhodopsin is an excellent test system for the methodological NMR work presented here, due to its stability, orientation properties and availability. In the following, it will be shown, that the orientation of functional groups with respect to the membrane/protein normal can be determined by ^{2}H MAOSS experiments.

Below, an introduction to bR is given, before some aspects of ^{2}H MAS as well as data analysis and results are discussed.

4.1.1 Bacteriorhodopsin Structure

Bacteriorhodopsin was discovered and identified as a light-driven proton pump from the archeobacterium *Halobacterium salinarium* in the early 1970s [104] and is an important model system for membrane protein structure, since it demonstrates fundamental principles :

- How can light energy be directly transformed into chemical energy?
- How can membranes be used for energy conservation?
- How are ions transported against a concentration gradient?

In addition, the structural similarity of bR relates it to membrane-bound G-coupled receptors such as rhodopsin, which make up 10% of the humane genome sequence [105].

Native bR forms trimers in a two-dimensional hexagonal array in the plasma membrane [106], which is called purple membrane due to the characteristic colour. It consists of 248 residues in a single polypeptide chain and has a molecular weight of 26 kDa. The amino acid sequence is shown in Fig.4.1 [107]. Using light energy, bR transports protons out of the cell, thereby creating a gradient, which drives ATP synthesis, flagella rotation and secondary transport processes.

The first three-dimensional structural model of bR as shown in Fig.4.1 was based on cryo-electron diffraction studies with a resolution of 0.27 nm $\times$ 1.0 nm [108]. Bacteriorhodopsin consists of seven hydrophobic α-helices, connected by hydrophilic loops and the N-terminus on the extracellular side. Retinal is covalently bound via a protonated Schiff base to Lys_{216} and buried in between the seven helices.

By preparing 20-40 μm small microcrystallites in lipid cubic phases and by applying newly developed synchrotron microbeams, it has been possible recently to solve the structure of bR by X-ray diffraction to a resolution of 0.25 nm in the dark adapted state [13]. This structure confirms in principle the previously established model, although corrections in the loops and residues involved in the proton channel have been necessary.

It should be also mentioned, that bacteriorhodopsin is a promising candidate for protein-based optoelectronics due to the phenomena connected to the bR photocycle such as ion transport, charge displacement and colour changes and outstanding protein stability. Especially the latter property attracted much attention for use in dynamic holography [109]

4.1.2 The Photocycle and Proton Translocation

Bacteriorhodopsin exists in the dark in two convertible forms, bR_{560} and K_{625}, which are in thermal equilibrium and contain *all-trans* and (13-*cis,* 15-*syn)* reti-

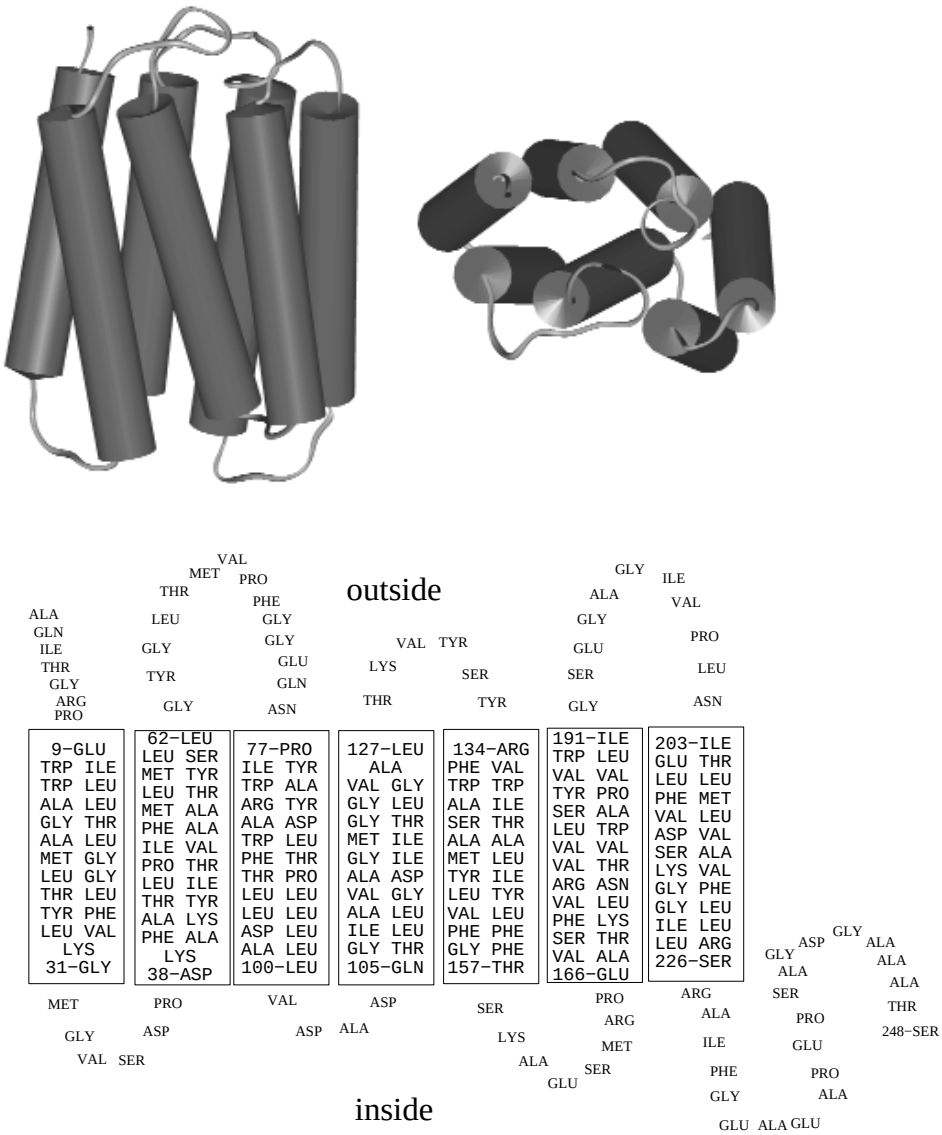

Figure 4.1: Amino acid sequence and suggested secondary structure of bacteriorhodopsin (retinal not shown).

nal, respectively. Absorption of light by bR_{560} initiates a photocycle that includes a series of intermediates identified by time-resolved visible spectroscopy (see Fig.4.2). Coupled with this photocycle is the transport of protons from the cytoplasm to the extracellular solution. The planar protonated *all-trans* retinal isomerizes on the femtosecond timescale following the absorption of light into the 13-*cis* conformation to form the K_{625} intermediate, which relaxes via some steps into L_{550}. Simultaneously during the L_{550} to M_{412} transition, one proton gets transferred from the retinal Schiff base to Asp-85 and one proton is released at the extracellular side. A re-protonation of the Schiff base takes place in the M_{412} to N_{550} transition and a proton is taken up from the intracellular side during N_{550} to O_{640}, which finally relaxes to bR_{560}, and completes the photocycle after about 30 ms at room temperature. All intermediate states can be trapped at low temperatures, which has been used for studies by solid state NMR [42],[110],[111],[112].

As illustrated in Fig.4.2, the translocation of protons is coupled with the protonation/de-protonation of the retinal Schiff base. Using site directed mutagenesis, several residues have been identified as playing an essential role for the proton transport [105],[113] and there is general agreement, that Asp-96 is the internal proton donor and Asp-85,Asp-212 and Arg-82 would all effect the proton release. However, Asp-96 is located about 1 nm from the Schiff base [13], which is too large for a single proton transfer step. Various models are still under debate, but water might play a role in that process [13],[105].

The NMR studies presented here were performed on bR_{560} with *all-trans* retinal with a deuterated methyl group at position C18 (see Figs.4.4). The aim was to determine the angle between the C5-C18 bond and the membrane normal Z_D by ^2H MAS. The membrane normal is assumed to be identical with the protein long axis Z_M,. which can be defined as the average vector of all seven helix long axes.

4.2 Deuterium MAS

Lineshapes of deuteron-wideline spectra are highly sensitive to molecular order and the type and time scale of molecular motion, a property which has been used extensively for studying biomembranes [73]. Questions such as lipid and protein dynamics [69],[114], lipid-protein interaction [115],[116] and membrane protein structures [42],[117],[118] were addressed using deuterons. However, the signal sensitivity of wide-line spectra can be rather low, since static solid-state spectra of disordered samples can be as broad as 200 kHz. Much better sensitivity can be achieved by magic-angle spinning, which would average the dipole-dipole coupling among deuterons as well as the chemical shift, so that only quadrupole interaction remains, which is refocused in spinning sidebands. The sensitivity advantage is illustrated in Fig.4.3a-c for a polycrystalline sample of alanine-d_3.

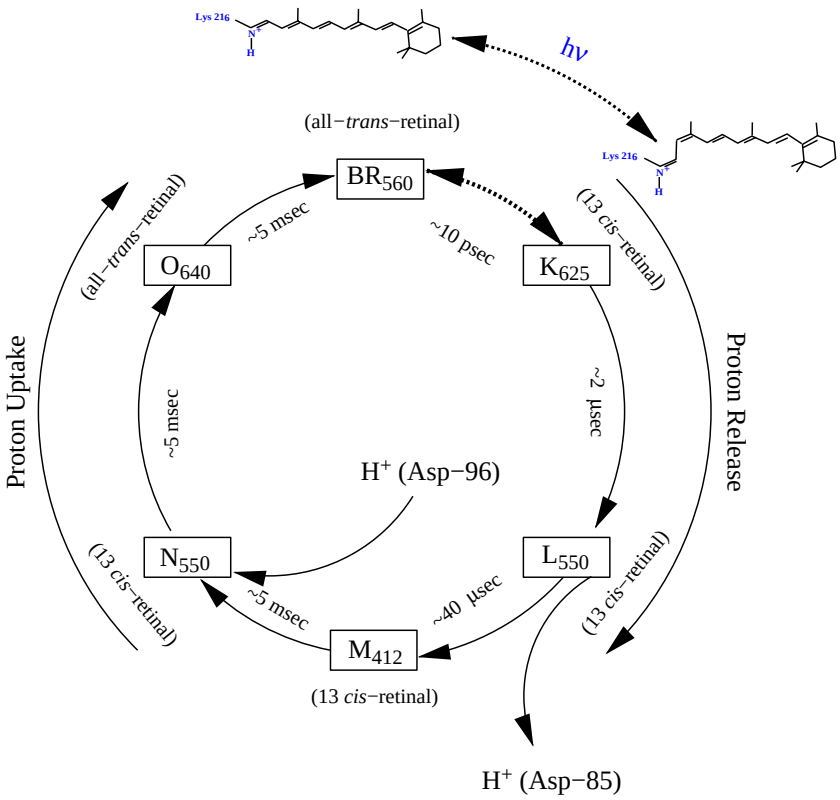

Figure 4.2: Intermediates in the bacteriorhodopsin photocycle: A proton is released from the protonated Schiff base and transferred to Asp-85. The resulting unprotonated Schiff base intermediate M is reprotonated by Asp-96, which takes up a proton from the cytoplasm.

The same number of scans was used for all spinning speeds and the signal-to-noise increases by up to a factor of 30. However, deuterium MAS has not been used extensively, maybe due to its slightly more complicated analysis compared to static experiments. Here, we will demonstrate, that ^{2}H MAS on oriented systems allows orientational information, even for systems with low deuterium concentration, to be extracted.

The earliest example of ^{2}H MAS aimed to resolve the chemical shifts of deuterons by rotor-synchronised sampling [119]. Other applications focused on observations of natural abundance and resolving inequivalent sites [120],[121] as well as computational aspects for determining quadrupole coupling constant and asymmetry parameter [122],[123]. Static experiments, such as deuterium two-dimensional exchange, were adapted to MAS conditions [124] and recently, aspects of proton decoupling and cross-polarisation were investigated [125]. The potential advantages of ^{2}H-MAS can be summarized in the following points [122]:

- significant sensitivity enhancement
- in principle sites with different chemical shifts can be observed
- a greater range of dynamic processes can be studied by MAS, since the linewidth of MAS sidebands is influenced by dynamics in the range of the spinning speed [15], while at the same time information about fast and slow dynamics can be extracted as in the static case

The static lineshape for deuterium has been introduced and discussed in the introduction in Chapter 1. Both spin-1 transition frequencies are calculated according to Eqn.1.18 which yields the absolute value of the difference as measurable quantity:

$$\Delta\omega_Q = \frac{3}{4}\frac{e^2qQ}{\hbar}\left(\frac{3\cos^2\beta_{PL}-1}{2} - \frac{1}{2}\eta\sin^2\beta_{PL}\cos 2\alpha_{PL}\right) \tag{4.1}$$

The quadrupole coupling constant $e^2qQ/2\pi\hbar$ is used to characterize the strength of the quadrupolar coupling and is for aliphatic C-^{2}H in the order of 170kHz.

An order parameter concept has been introduced in the literature for the study of lipids and liquid crystals in order to describe rapid fluctuations of C–D bond vectors around the director axis. Since these motions are fast on the ^{2}H NMR time scale, $\Delta\omega_Q$ has to be replaced by its time average, described by three order parameters [73]:

$$\Delta\omega_Q = \frac{3}{4}\frac{e^2qQ}{\hbar}\left(\frac{3\overline{\cos^2\beta_{PL}}-1}{2} - \frac{1}{2}\eta\overline{\sin^2\beta_{PL}\cos 2\alpha_{PL}}\right) \tag{4.2}$$

$$= \frac{3}{4}\frac{e^2qQ}{\hbar}\left(S_{33} - \frac{1}{2}\eta\left(S_{11}-S_{22}\right)\right) \tag{4.3}$$

However, no use will be made of this concept in the following, because intensities rather than frequencies are discussed, and additionally the labelled site in bacteriorhodopsin is motionally rather restricted.

The situation of sample spinning is now considered. Due to the symmetry of the electric field gradient tensor, expressions for ω_Q as well as the MAS coefficients C_1,S_1,C_2,S_2, as introduced in Chapter 1, simplify dramatically to

$$\omega_Q = \pm\frac{3}{4}\frac{e^2qQ}{\hbar}\left(\frac{(3\cos^2\theta-1)}{2}\frac{(3\cos^2\beta_{PR}-1)}{2}+\Psi(t)\right) \tag{4.4}$$

where $\Psi(t)$ with C_1,S_1,C_2,S_2 is defined below:

$$\Psi(t) = C_1\cos(\omega_r t) + S_1\sin(\omega_r t) + C_2\cos(2\omega_r t) + S_2\sin(2\omega_r t) \tag{4.5}$$

$$\begin{aligned} C_1 &= -3/4\sin 2\theta\sin 2\beta_{PR} \\ S_1 &= 0 \\ C_2 &= +3/4\sin^2\theta\sin^2\beta_{PR} \\ S_2 &= 0 \end{aligned}$$

According to the discussions in Chapter 3 (Eqn.3.2), the intensity of a spinning sideband I_N with θ being the magic angle, is now calculated by:

$$I_N(\beta_{PR}) = |F_N(\beta_{PR})|^2 \tag{4.6}$$

with

$$F_N(\beta_{PR}) = \int_0^{2\pi}\frac{d(\omega_r t)}{2\pi}\exp\left[i\left(C_1\sin(\omega_r t)+\frac{1}{2}C_2\sin(2\omega_r t)-N\omega_r t\right)\right] \tag{4.7}$$

Including double cylinder symmetry and mosaic spread and coordinate transformation from PAS to MF and from MF to RF, one obtains a formal expression as in Eqn.3.8 for I_N :

$$\begin{aligned} I_N(\beta_{PM},\beta_{MR},\Delta\beta) &= K\int_0^{2\pi}d\alpha_{MR}\int_0^{2\pi}d\gamma_{MR}\int_{\beta_{MR}-\Delta\beta}^{\beta_{MR}+\Delta\beta}d\beta_{MR} \\ &\quad\times p_{MR}(\beta_{MR})I_N(\beta_{PM},\alpha_{MR},\beta_{MR},\gamma_{MR}) \end{aligned} \tag{4.8}$$

All simulations were performed using the software described in Appendix B, in the same way as for spin-1/2 by replacing the chemical shift anisotropy with

the quadrupole coupling constant and by setting the isotropic chemical shift to zero. Spectra were symmetrized to account for both transitions $m_I = \pm 1$.

By orienting samples on solid supports, orientational information from deuterium MAS spectra can be obtained, which will be demonstrated by using ordered samples of bacteriorhodopsin, regenerated with the deuterium labelled ligand retinal. The retinal was synthesized with a deuterated methyl group attached to carbon C18 as illustrated in Fig.4.4. Due to the fast methyl group rotation, the whole system can be treated as one spin-1 with an averaged quadrupole coupling constant. The z-axis Z_P of the PAS is defined by the bond vector connecting the carbons C5-C18. It will be shown in the following how the orientation of this vector with respect to the molecular long axis Z_M can be obtained.

4.3 Materials and Methods

4.3.1 Sample Preparation

A sample of bacteriorhodopsin with ^{2}H-labelled retinal was kindly provided by Ian Burnett and James Mason, Biomembrane Structure Unit, Oxford University.

[18-^{2}H]-Retinal, deuterated at the methyl group at position C18 (see Fig.4.4), was regenerated into retinal deficient bacteriorhodopsin according to published procedures [126]. The retinal deficient strain *JW5, Halobacteria salinarium* was grown in the dark in a peptone based medium (250 g NaCl, 20g $MgSO_4$, 10g Oxoid Bacteriological Peptone, 3g Na_3Citrate, 2g KCl in 1 litre) at 105 rpm flask rotation and 37^{o}C. When growth slowed, 6mg *all-trans* retinal, dissolved in 2ml ethanol, was added over two days to each litre of culture. Purple membrane was isolated according to the method of Oesterhelt and Stoeckenius [127]. Cells were harvested through centrifugation (700 rpm for 15 min at 4^{o}C). The pellets were resuspended in 250ml basal salt (medium without peptone). DNAase 1 (0.9 μl) was added to prevent the development of excessive viscosity. The cells were dialysed (12 hours) against two litres of sodium chloride solution (0.1M). The dialysate was washed three times with 0.1M NaCl and then once more with distilled water. Final purification was performed using a 25-45% sucrose gradient (18 hours at 25000 rpm). On average 12mg of bacteriorhodopsin was obtained per litre of culture.

4.3.2 Sample Orientation

Purified purple membrane was washed with and resuspended in deuterium depleted water. The sample was spread evenly over 80, round, 0.07 mm thin glass disks with a diameter of 5.4 mm (Marienfelde GmbH). An amount of 0.2 mg protein in 25 μl was applied to each disk. Uniaxial films with good orientation of the purple membrane patches parallel to the sample director were produced by

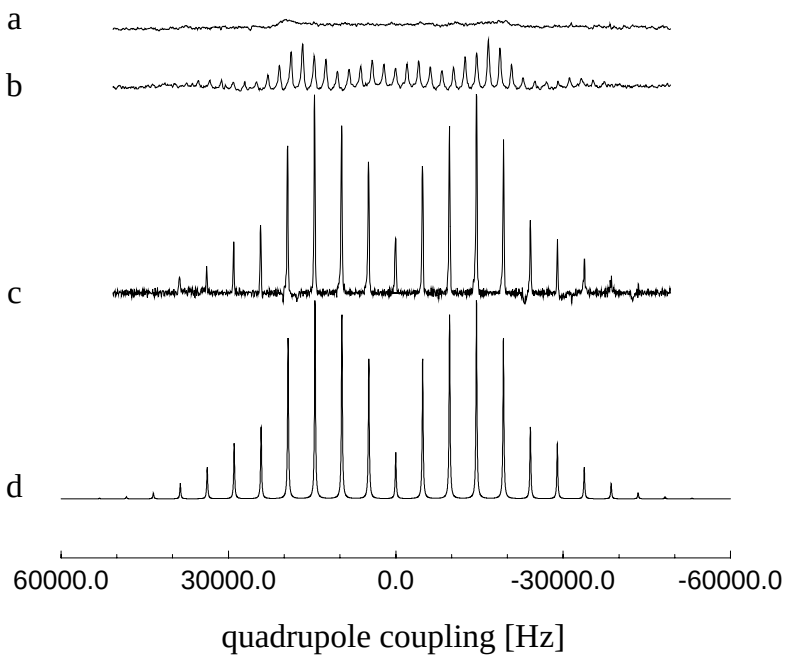

Figure 4.3: ^{2}H MAS spectra at different spinning speeds of a polycrystalline sample of alanine-d_3 : ω_r= 0 Hz (a), ω_r= 2000 Hz (b), ω_r= 5000 Hz (c), computer simulation for ω_r= 5000 Hz and eq=39kHz. The S/N increases from the static case to ω_r= 5000 Hz by a factor of 30.

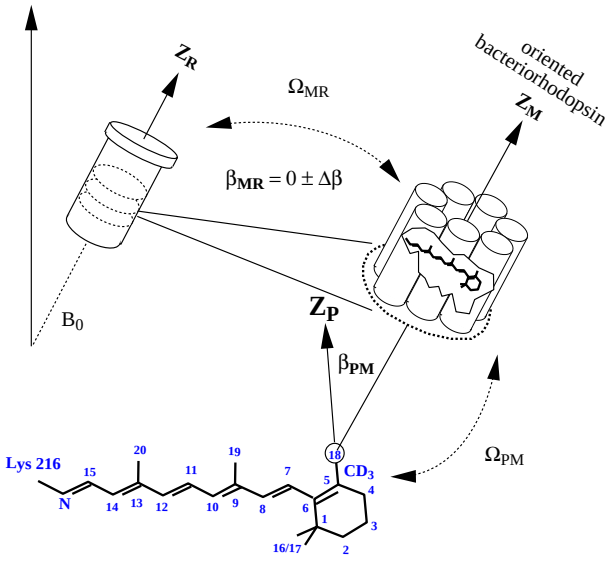

Figure 4.4: Reference frames for ^{2}H MAOSS on bacteriorhodopsin. The retinal carried a CD_3 group at position C18. The z-axis Z_P of the principal axis system is defined by the C_5-C_{18} bond vector, while the molecular frame is assumed to be identical with the membrane/rotor frame, except some variations $\Delta\beta$ caused by the mosaic spread. The molecular axis Z_M can be visualised as the average vector of all seven helical long axes in bR.

controlled evaporation of the bulk water at 85% relative air humidity and 4^oC over a period of 48 hours. A second application produced a final concentration of 0.4 mg protein per plate. The optimum between maximal protein concentration and best orientation was found by comparing different disks by polarized light microscopy. The glass plates had previously been cleaned in nitric acid and methanol/ethanol and dried under a stream of nitrogen gas. Finally, the disks were placed on top of each other and mounted into a MAS rotor using the tools described in Appendix A. Special KelF inserts on top and bottom guaranteed a fixed and stable position of the disk stack under spinning conditions. An unoriented sample was prepared by drying bR pellets on glass plates, scratching the protein film off and placing it in the MAS rotor.

4.3.3 NMR Experiments

All NMR experiments were performed at 61 MHz for ^{2}H on a BRUKER MSL 400 and double resonance 7mm MAS probes. A recycle delay of 500 ms was used. Simple one pulse experiments without proton decoupling were performed. Methyl groups are self decoupled due to their fast molecular reorientation. A $\pi/2$ pulse was typically 6μsec. An oscilloscope and a home-built speed controller were used to control and stabilise the spinning speed within a range of $\pm 3Hz$. Experiments were performed at 210 K and 250 K and at spinning speeds of up to 5000Hz. Between 100,000 and 400,000 scans were acquired with a recycle delay time of 300ms. Spectra were zerofilled with 4K points, Fourier transformed and carefully phase corrected. An exponential linebroadening of 100 Hz was applied. Finally, spectra were symmetrized to account for some remaining asymmetry.

4.4 Results and Data Analysis

^{2}H MAS spectra of oriented and unoriented bacteriorhodopsin were recorded at 250 K at 4950 Hz spinning speed and 210 K with 4040 Hz spinning rate. The analysis of the unoriented spectra reveals a quadrupole coupling constant of 39 kHz, which is identical to published values for the CD_3 group at the same position [128] and gives rise to the assumption, that no unusual dynamic takes place except the fast methyl group rotation.

Angle information about the tilt of the C5-C8 bond vector can be extracted from the oriented spectra in Figs.4.5,4.6 by evaluating the observed sideband intensities in terms of the expressions derived before (Eqn.4.8 and Chapter 3).

4.4.1 Angle Determination

In order to analyse the ^{2}H MAOSS spectra obtained from [18-CD_3] retinal in bacteriorhodopsin, a χ^2 merit function

$$\chi^2 = \sum_{i=1}^{N} \left(\frac{g_i^{\exp} - g_i^{sim}(\beta_{PM})}{\sigma_i} \right)^2 \tag{4.9}$$

has been minimized in dependence of the tilt angle β_{PM}. Here, $g_i^{\exp}$ is the intensity at the i-th point of the experimental spectrum, while $g_i^{sim}(\beta_{PM})$ is a simulated intensity. The experimental error σ_i in our case is actually the accuracy, with which a spectral peak intensity can be measured, i.e. the signal-to-noise ratio [94]

$$\frac{S}{\sigma_N} = \frac{\text{peak amplitude}}{\text{r.m.s. noise amplitude}} \tag{4.10}$$

determines this precision. Here, the r.m.s. noise amplitude is used as experimental error and has been measured to be ca.10% of the maximum intensity. However, the location of sidebands is completely determined by the sample spinning speed ω_r , while their intensity is a function of tensor size, orientation, spinning speed and distance from the central line, as discussed before. Additionally, the sideband pattern is symmetric about the central line I_0 due to the spin-1 nature of deuterium. For these reasons, it is sufficient to fit only a finite number of integral sideband intensities, which follows the lines originally proposed by Hertzfeld and Berger for analysing powder MAS sideband pattern [22]. The merit function is now modified to

$$\chi^2 = \sum_{N=0}^{8} \left(\frac{\mathrm{I_N^{exp}\text{-}I_N^{sim}}(\beta_{PM})}{\Delta \mathrm{I_N^{exp}}} \right)^2 \tag{4.11}$$

and plotted versus β_{PM} in Figs.4.5,4.6. For the experiments at T=210 K, a global minimum is found for $\beta_{PM} = 36^\circ$ (Fig.4.6), while the same analysis for the experiments performed at T=250 returns a value of $\beta_{PM} = 27^\circ$ with another minimum at 7°. Some local extreme values do exist as well. Their origin is discussed below. The function for χ^2 was minimized for different mosaic spread values $\Delta\beta$ in order to evaluate their influence to the fitting result. Figs.4.5 and 4.6 illustrate, that the minima are not shifted but broadened by increasing the degree of disorder in the system. To verify our findings, a χ^2 minimization was performed on a synthetic data set, which corresponds to $\beta_{PM} = 27^\circ$ and a mosaic spread of $\Delta\beta = \pm 8^\circ$ in Fig.4.5 and which reproduced the global and all local minima, except the one at $\beta_{PM} = 7^\circ$.

4.4.2 The Symmetry Problem and the Ambiguity of Tilt Angles by ^{2}H-NMR

A potential drawback of static deuterium solid-state NMR for structure determination has been the spectral symmetry due to the spin-1 character of deuterons.

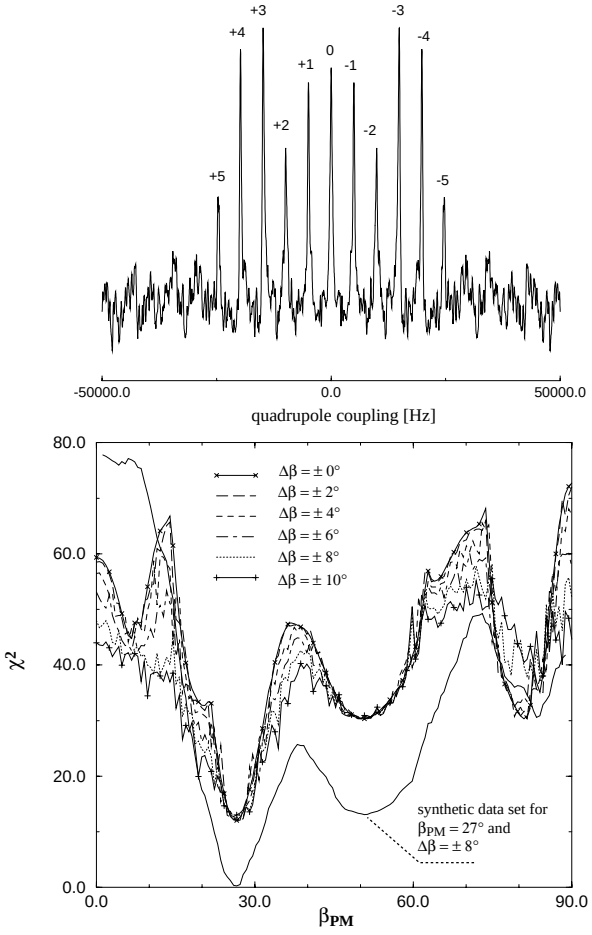

Figure 4.5: χ^2 analysis of ^{2}H MAS spectra of oriented bR, recorded at T=250K and ω_r=4950Hz: integral intensities of sidebands I_0 to I_8 were simulated as a function of tensor orientation and fitted to the experimental data. The best fit is obtained for β_{PM}=27°. The larger the mosaic spread, the broader is the distribution about the minimum value. An additional contribution to the spectrum is found at β_{PM}=7°, which is not reproduced by the synthetic data set.

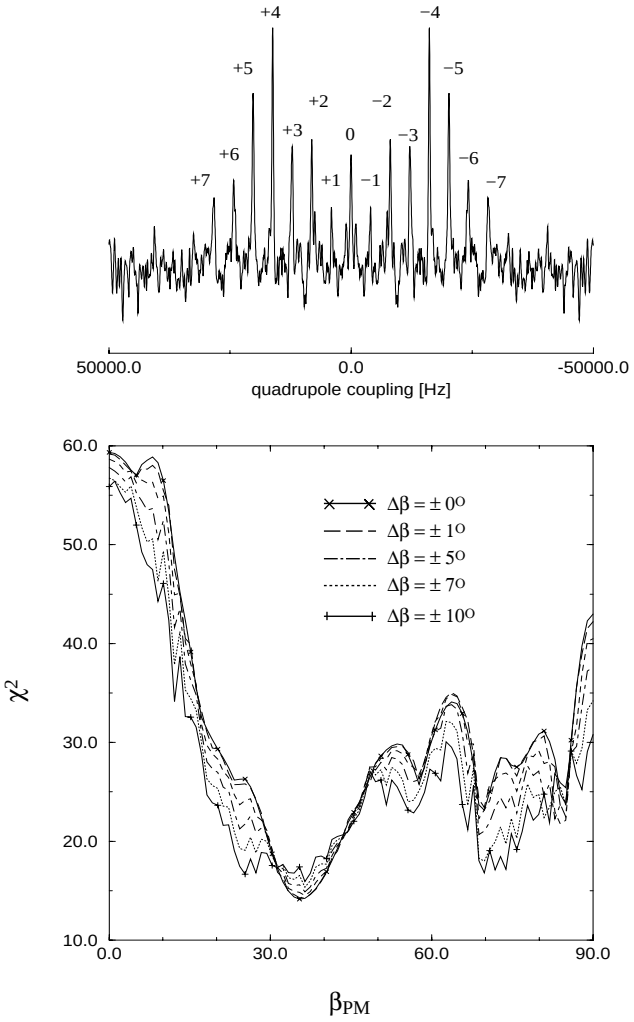

Figure 4.6: χ^2 analysis of ^{2}H MAS spectra of oriented BR recorded at T=210K and ω_r=4040Hz: integral intensities of sidebands I_0 to I_8 were simulated as a function of tensor orientation and fitted to the experimental data. The best fit is obtained for β_{PM}=36°.

Only the absolute splitting in the Pake doublet (see Fig.1.3.) can be measured, but no decision can be made about which part of the spectrum was created by which transition. This has consequences for studying deuterated sites in oriented membranes. A measured quadrupole splitting can be related to two angles. Eqn.4.4 can be modified for the non-sample-spinning case by setting ω_r= 0 Hz and so we obtain for the quadrupole splitting:

$$\Delta\omega_Q(\theta,\beta_{PR}) = \frac{3}{8}\frac{e^2qQ}{\hbar}\begin{pmatrix} |(3\cos^2\theta-1)(3\cos^2\beta_{PR}-1)|+ \\ |3\sin 2\theta\sin 2\beta_{PR}|+ \\ \left|3\sin^2\theta\sin^2\beta_{PR}\right| \end{pmatrix} \tag{4.12}$$

Fig.4.7a illustrates how $\Delta\omega_Q$ is modulated by the orientation of the membrane normal with respect to the magnetic field (θ) and by the tilt of the C-D bond vector with respect to the membrane normal (β_{PR}). If the membrane normal Z_D is parallel to the magnetic field, i.e. $\theta = 0°$, a symmetry would occur about $\beta_{PR} = 54.7°$. In this situation, the C-D bond vector and so the PAS z-axis would be oriented at the magic angle and the quadrupole splitting would collapse. Consequently, the same situation would arise by a perpendicular orientation $\theta = 90°$, where the singularity is found at $\beta_{PR} = 90° - 54.7° = 35.3°$. It has been suggested and demonstrated to use these different symmetry properties to determine the correct angle [129].

Fig.4.7a also shows the special situation under consideration here, namely orienting the membrane normal at the magic angle. The quadrupole splitting would collapse, if the C-D bond vector is parallel to the membrane normal, but increase rapidly by tilting the bond vector. A symmetry occurs about $\beta_{PR} = 54.7°$. If the sample is now spun in the magnetic field, the distribution of $\Delta\omega_Q$ over β_{PR} experiences an additional modulation with $\cos(\omega_r t)$ and $\cos(2\omega_r t)$ according to:

$$\Delta\omega_Q(\theta,\beta_{PR},\omega_r t) = \frac{3}{8}\frac{e^2qQ}{\hbar}\begin{pmatrix} |(3\cos^2\theta-1)(3\cos^2\beta_{PR}-1)|+ \\ |3\sin 2\theta\sin 2\beta_{PR}\cos(\omega_r t)|+ \\ \left|3\sin^2\theta\sin^2\beta_{PR}\cos(2\omega_r t)\right| \end{pmatrix} \tag{4.13}$$

which explains qualitatively the finding of local minima in Fig.4.5. The sideband intensities would reflect this symmetry, but in a more complex manner, since they depend also on the distribution geometry of the deuterons in the sample (Eqn.4.8).

It is important to note, that for the case of non-spinning as well as spinning experiments, quadrupole splitting and spectral intensity, i.e. lineshape, are depending on the tensor orientation, which means that simulating and fitting the spectral lineshape for one membrane orientation in the magnetic field is sufficient for determining the tilt angle. Of course, this does not apply to liquid crystalline

lipids, which always produce two sharp signals instead of a complex lineshape, because they are not transversely isotropic [73].

In the case of MAS NMR all lineshape information is refocused in spinning sidebands I_N separated by $\pm N\omega_r$, i.e. all information is contained in the intensity of these sidebands and the χ^2 analysis of the experimental data permits a clear distinction between global and local minima. Additionally, a lineshape fit on synthetic data derived from the global minimum at $\beta_{PR} = 27°$ reproduces clearly the observed local side minima (Fig.4.5). However, there might be situations in which this procedure requires additional constraints, e.g. if the studied molecule exists in the sample in two different conformations, which could give similar χ^2 values for two different orientations β_{PR}. Spinning experiments at different angles, θ, are not very useful in this case, but MAS experiments at different spinning speeds could provide the necessary information, since the symmetry of $\Delta\omega_Q(\beta_{PR})$ depends on ω_r. Computer simulations for two different orientations, $\beta_{PR} = 20°$ and $\beta_{PR} = 80°$ for three different relative spinning speeds were performed and are shown in Fig.4.7b. While the fitting procedure would return for all spinning speeds the same best fit, all local minima are shifted remarkably, which allows their identification as mirror images of the required angle.

A similar case for highly mobile oriented molecules such as chloroform oriented in nematic liquid crystals has been discussed by Kumar et al.[130]. They concluded, that in principle the sign of the quadrupole splitting can be determined from the spinning sideband pattern, although in case of deuterium, an additional interaction is needed, such as the J-coupling from a ^{13}C-^{2}H group.

4.4.3 Error Analysis

It is rather important for new methodological work to identify potential error sources and to quantify the uncertainties of the fitting parameters. In the special case of ^{2}H MAS, the only free parameter is β_{PM} for which an error has to be estimated.

The position of MAS sidebands in the spectrum is completely described by the sample spinning speed, so only their intensities have to be considered, which is associated with an error due to the signal-to-noise ratio. Here, the r.m.s. noise amplitude $\sigma_N = 10\%$ was used as an error for the intensity at a certain point in the spectrum.

The best fit for both results in Figs.4.5 and 4.6 gave values of $\chi^2 \sim 12.0$. The goodness of this fit can be evaluated by calculating the χ^2 probability

$$P(\chi^2, N-m) = \int_{\chi^2}^{\infty} \frac{2^{-(N-m)/2}}{\Gamma((N-m)/2)} \chi'^{(N-m-2)} e^{-\chi'^2/2} d\chi'^2 \qquad (4.14)$$

where N and m are the numbers of data points and free parameters. Here, eight integral sideband intensities were taken into account, while only one free

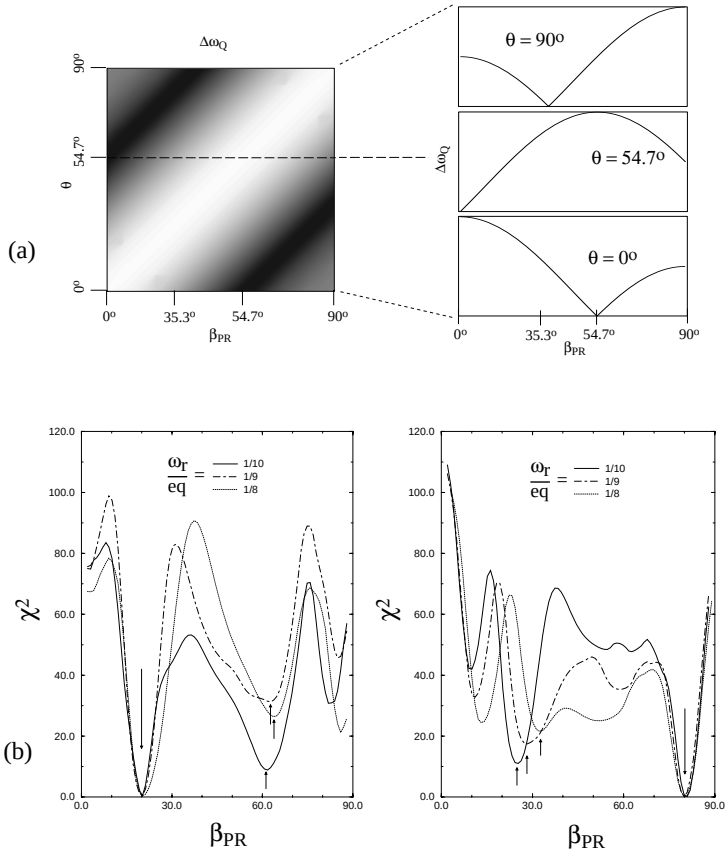

Figure 4.7: The quadrupole splitting $\Delta\omega_Q$ as a function of θ and β_{PR} can have a two fold symmetry, which would require additional experiments for precise angle determination (a). However, a spectral analysis, as described here allows this problem to be overcome. Additionally, potential ambiguities can be resolved at different MAS spinning speeds: local minima arising from symmetry artefacts would shift their position, while true minima remain at fixed positions (b).

parameter was allowed, so we obtain P=10%, which an acceptable result [131]. However, it is difficult to give an direct error estimate since β_{PM} modulates the sideband intensities in a non-linear way. To overcome this problem, Monte Carlo simulations of some synthetic data sets were performed, i.e. data points in a simulated spectrum corresponding to the best fit value, were randomly changed in their intensity. A χ^2 minimization was performed, which resulted in a distribution of the best fit value of β_{PM} with a width of $\pm 2^\circ$.

Another error source is the quality of orientation in the sample. It is shown in Figs.4.5 and 4.6 , that the χ^2minimum gets broader with increasing mosaic spread, for which MC simulations yield an additional error of $\pm 3^\circ$ for a mosaic spread of $\Delta\beta = \pm 8^\circ$.

Finally, contributions from natural abundance have to be estimated. Deuterium has a natural abundance of 0.015%. Considering, that on average, each amino acid contains 7 protons, we would find per bacteriorhodopsin molecule with its 248 residues about 0.26 deuterons. These 0.26 deuterons should contribute by ca. 11.5% to the signal from the CD_3 group in the retinal. The quadrupole coupling of deuterons in different chemical groups such as CH_3, CH_2, CH, NH and H_2O can vary over a broad range, so some groups might contribute to the CD_3 spectrum more than others. Taking only CD_3 groups into account would result in a 2-3% contribution. In fact, the difference between the ^{2}H MAOSS spectrum and the best fit simulation, as shown in Fig.4.8, has an integral intensity of 2.5% of the experimental spectrum, which matches the natural abundance contribution rather well. The effect of natural abundance background was simulated by randomly varying individual sideband intensities at constant signal-to-noise, which gave an uncertainty of $\pm 1^\circ$.

Summarizing, it can be stated, that the experimental error for determining the tilt angle β_{PM} increases with decreasing signal-to-noise, increasing mosaic spread and increasing natural abundance background. The uncertainty induced by the mosaic spread has the largest influence on the error. Additionally, the precision of the quadrupole coupling constant and the asymmetry parameter are of direct importance. A variation of ± 1 kHz in the quadrupole coupling constant would cause an angle variation of $\pm 1^\circ$. However, both parameters can be determined to a high precision.

Therefore, the angle obtained at T=210K, $\beta_{PM}=36^\circ$, has to be considered with a maximal error of $\pm 5^\circ$, while the tilt at T=250K is $\beta_{PM}=27^\circ \pm 6^\circ$.

4.5 Discussion

The orientations of the C5-C18 bond vector, as well as for C9-C19 and C13-C20 have been determined previously by various methods for the dark adapted state of bR. Static solid state NMR gave angles of $37^\circ \pm 1^\circ, 40 \pm 1^\circ$ and $32 \pm 1^\circ$ [132], while the latest X-ray structure claims 32°, 34° and 10°[13] for C18,C19 and

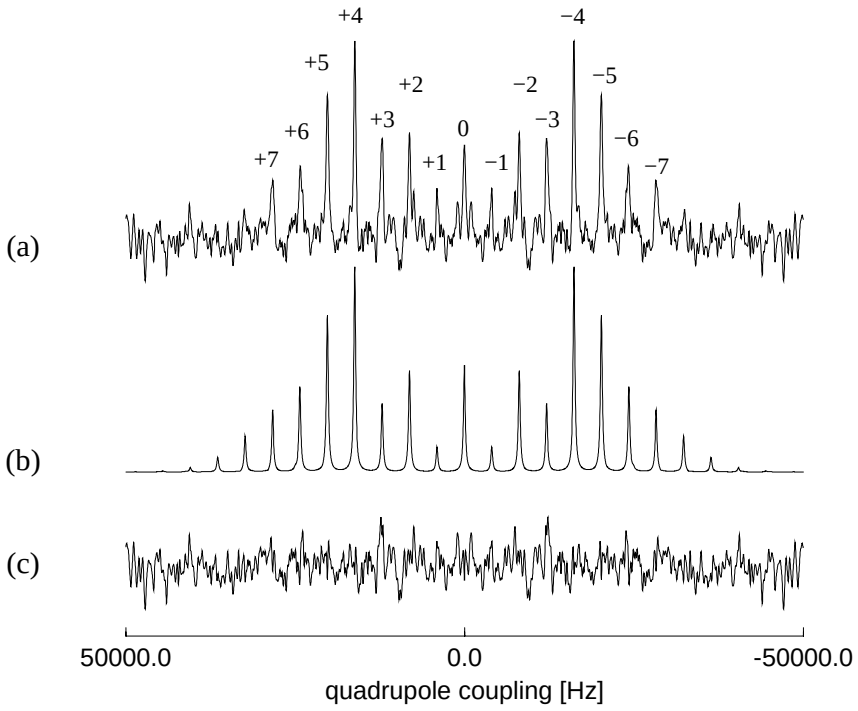

Figure 4.8: Comparison between experimental ^{2}H MAOSS spectrum of bR (a), the best fit simulation (b) and the difference between both (c). The integral intensity of the difference spectrum is about 3% of the experimental spectrum, which corresponds well to the expected natural abundance contribution.

C20 respectively. The angle information for the EM model, returned 38.6°, 29.3° and 16.1°, which was however obtained indirectly by fitting retinal back into the proposed bR structure[133]. No error estimations were given. There is general agreement in the interpretation of these data, that the structure of retinal in bR is distorted.

The angle β_{PM}=36° ± 5° obtained here at T=210K is in excellent agreement, with the results from the static wideline NMR experiments, which were obtained under similar experimental conditions [132]. However resolution and sensitivity are greatly improved in the MAOSS experiment. The resolution is good enough the observe clearly a shift of the central MAS resonance line with respect to D_2O, corresponding to the chemical shift of CD_3 and the significant enhancement of the signal-to-noise ratio allows a rather precise data analysis.

There are various possible explanations for the different angle of β_{PM}=27° ± 6° obtained at T=250K. The NMR experiments were performed in the dark and at a temperature of -20°C. It has to be assumed, that bR exists in both intermediate forms bR_{560} and K_{625} in thermal equilibrium, because the used temperature is not low enough to trap bR at K_{625} after illumination [111]. The ratio between both states would be between 2:1 and 1:1 [134], i.e. the observed ^{2}H MAOSS spectrum would actually consist of two components with potentially different orientations. It has been found here, that the spectrum consists mainly of components with an orientation of β_{PM}=27° and some minor components with β_{PM}=7°, which would not be consistent with the expected ratios and the result obtained at 210K. However, these findings could reflect a more complex dynamical situation, in which maybe the whole chromophore or part of the protein undergo anisotropic motions. Simulations did show, that the minimum in Fig.4.5 shifts towards larger angles for smaller quadrupole coupling constants, which would underline this assumption, but the tilt angle was always significantly different from the other result within a realistic range of quadrupole coupling constants. It has been also shown, that the signal-to-noise increases remarkably by increasing the temperature, which moves the system away from the T_2 minimum[112], while the methyl group C18 the chromophore of bR is even at liquid nitrogen temperature still in the fast motional limit[128]. Further investigations will show, whether a relaxational or conformational effect causes these different orientations.

4.6 Conclusions

It has been shown, that ^{2}H MAS on oriented systems is a valuable tool for obtaining precise structural information in cases of low deuterium concentration, which makes it especially attractive for studying labelled groups in membrane proteins, which are not as easily available as bR (the deuterium concentration used here was only 3μMol). Future development will focus on multidimensional experiments, such as modified versions of PASS or ^{2}H exchange spectroscopy,

which might allow multiple deuterium labelling [21].

Chapter 5

^{13}C Rotational Resonance and MAOSS Experiments on M13 Coat Protein

Abstract

^{13}C MAS NMR spectroscopy has been applied to M13 coat protein, selectively labelled with two ^{13}C spin pairs its hydrophobic domain in residues Val-29 and Val-30, and Val-29 and Val-31. Rotational resonance recoupling experiments on unoriented samples provided two distance constraints between Cα and C=O positions and so the dihedral angles, Φ and Ψ, for Val-30 which revealed an α-helical conformation. MAOSS experiments using the ^{13}C=O labelled site in the same sample allowed a measurement of the tilt of the helix in the membrane to be made.

It is shown that in principle, one unified MAS approach can be used to obtain conformation as well as orientational information. Potential advantages and future perspectives of the MAOSS approach are discussed.

5.1 Introduction

5.1.1 M13 Coat Protein

Structure and reproductive cycle of M13 bacteriophage

Filamentous bacteriophages form a large group of related virus strains with similar morphology and life cycle [135] which infect non-pathologically gram-negative bacteria by absorbing to the tip of specific bacterial pili, e.g. M13, fd and f1 infect *E.coli* via its F-pili (Fig.5.1). The phage particles are rods of about 6nm diameter and 800nm in length. They contain a circular, single stranded DNA

of 6407 nucleotides [136] which is protected by 2700 copies of coat protein and some other proteins in minor quantities (A,C,D$\simeq$2%) [137]. Upon adsorption, the protein coat of the virion dissolves into the inner cell membrane [138] and the DNA enters the host cell while being converted into double stranded replicative form. Inside the host cell, new single-stranded DNA is synthesized and covered by the DNA-binding protein gene-5, resulting in a intra-cellular rod-shaped nucleoprotein complex similar to the extracellular virus itself but less stable. The filamentous bacteriophage is continuously assembled and extruded through the bacterial membrane without killing the host cell. At the same time, gene-8 encoded major coat protein is newly synthesized as a water soluble procoat protein with an additional leader sequence at the N-terminus consisting of 23 amino acids [139]. The procoat is incorporated in the plasma-membrane and the leader sequence is cleaved off by the leader peptidase. During the process of phage extrusion, the gene-5 protein is exchanged by new and old major coat protein. Although the actual amino acid sequence of gene-8 protein differs among various strains, its geometry is always a slightly curved $\alpha-$helix for all of them [140]. The whole phage cycle is schematically illustrated in Fig.5.1.

M13 coat protein in the bacteriophage

M13 coat protein has been studied extensively due the intriguing property in adopting to three different environments, as coat protein in the bacteriophage, as membrane protein in the inner *E.coli* plasma membrane and as a procoat with a leader sequence after being synthesized prior membrane insertion. It has a molecular weight of 5240Da and consists of 50 residues with a sequence shown in Fig.5.2 [136]. The protein can be divided into three regions: the acidic domain of 20 residues, a hydrophobic domain of 19 and a basic domain of 11 amino acids. The hydrophobic region is believed to span the cytoplasmic membrane of the target cell [141]. The major coat protein is very similar to the coat protein from f1 and fd phage in that the 12th residue asparagine is replaced with aspartic acid [142].

X-ray diffraction has shown, that M13 coat protein is in a complete α-helical secondary structure in the intact phage particle with the overall helix axis approximately parallel to the filamental axis [138]. A disordered helical structure for residues 40-45 has been found by solid-state NMR [143] and the helical axis for residues 28-32, 33-39 and 40-48 is tilted by 20°,7° and 14° with respect to the phage long axis [144]. This agrees well with the diffraction studies, which suggested a slightly twisted helix [140].

M13 coat protein in detergent micelles and model membranes

The membrane-bound form of the coat protein has been studied extensively, which led to the formulation of several structural models. The coat protein dis-

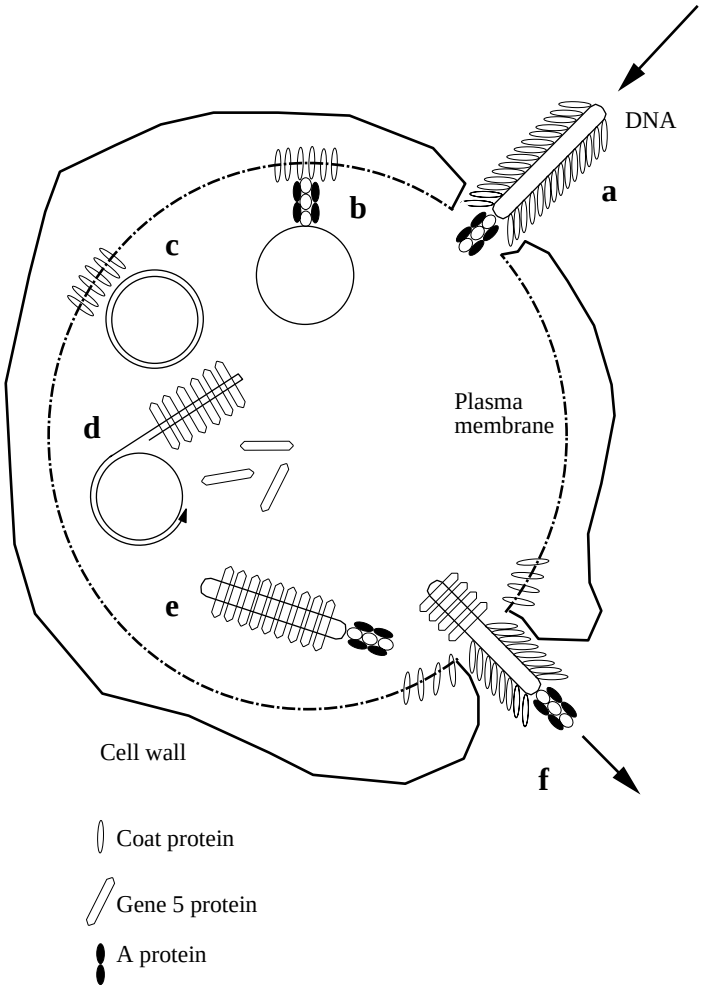

Figure 5.1: Schematic illustration of some features of the filamentous bacterial life cycle. (a) phage attachment to bacterium by means of minor coat protein A; (b) viral DNA and A protein enter cytoplasm, leaving major coat protein in plasma membrane; (c) DNA is converted to duplex form and replicated, which might require presence of major coat protein; (d) duplex spins off a single stranded tail coated with gene 5 protein; (e) circular DNA molecule in linear gene 5 protein complex; (f) viral DNA passes out through bacterial envelope, while gene 5 is replaced by major coat protein.

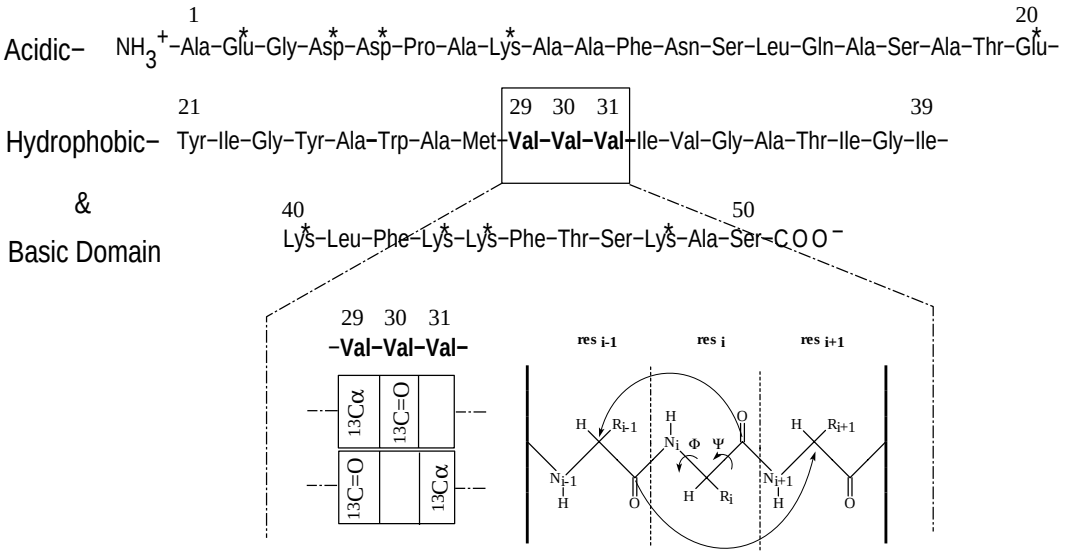

Figure 5.2: Amino acid sequence of major coat protein M13. Three domains are found: an acidic N-terminus of 20 residues, a hydrophobic domain 19 residues and a basic C-terminus of 11 residues. Charged, polar amino acids are labelled with *. Two samples were prepared, each with a pair of $^{13}C\alpha$-$^{13}C{=}O$ labels in [Val-29, Val-30] and [Val-29, Val31], as indicated below the sequence. The distances [α29,30] and [29,α31] define the dihedral angles Φ and Ψ of Val-30.

solved in detergent micelles and bilayers has been described as an arrangement of dimers with a large fraction of α-helix and β-sheet [145],[146] but also as an almost completely α-helical monomer [81]. A form in which the protein adopts a β-sheet structure has also been found [147]. It has been shown that the mentioned differences are brought about by the isolation and purification procedures used for the preparation of the samples [148]. Here, we are only concerned with the α-helical monomeric form (also called b-state). The b-form of M13 has about 60-90% α-helical structure [81],[140]. The system has been studied by NMR for many years. Dynamic and exchange rates of amide protons were measured [77],[83],[85],[149] and chemical shifts of amide protons, ^{15}N resonance, ^{13}CO,^{13}Cα, ^{1}Hα,^{1}Hβ have been assigned [40],[78].In the latter study, it was found, that the secondary structure consists of two α-helices, comprised of residues 6-20, 24-50, connected by a hinge region around residue 22. Using the combination of two-dimensional high-resolution NMR and solid-state NMR, the membrane bound form of the closely related fd-coat protein has been studied, which suggested a long hydrophobic helix crossing the membrane and a shorter amphipathic helix which lies in the plane of the bilayer [81]. Dynamic studies on fd as well as M13 coat protein revealed, that the hydrophobic, transmembrane domain is motionally restricted on the relevant NMR time-scales, while the amphipathic helix is less restricted [77],[82],[85],[150].

5.1.2 Objectives

It will be demonstrated, that by high resolution solid-state NMR (MAS), distance and orientational constraints can be obtained from the same labelling scheme, which allows the local conformation and orientation of membrane proteins to be determined. For that purpose, two samples of M13 coat protein were prepared, following a ^{13}C labelling scheme, which allows two rotational resonance distance measurements to be made to define one pair of dihedral angles Φ and Ψ [151]. As illustrated in Fig.5.2, three residues -Val29-Val30-Val31- in the centre of the hydrophobic core were chosen for labelling. In the following, the symbols M13[α29,30] and M13[29,α31] will refer to the protein M13 with spin pairs^{13}Cα-Val29,^{13}C=O-Val30 and ^{13}C=O-Val29,^{13}Cα-Val31, respectively.

Additionally, the large chemical shift anisotropy of ^{13}C=O can be used to extract the tensor orientation with respect to the membrane normal. This is an extension to the ^{2}H-MAOSS studies on bR demonstrated in Chapter 4, but for spin-1/2 and non-vanishing asymmetry parameter. Here, not the orientation of a chemical group with respect to the molecular frame but the orientation of the whole molecular frame with respect to the membrane frame is studied (see Chapter 3). It will be shown, that the MAOSS approach has some important advantages over measuring orientation constraints by static NMR.

5.1.3 Rotational Resonance NMR

Rotational resonance NMR spectroscopy is a technique that measures internuclear distances in solids. The physical basis of R^2 is the measurement of the magnetic dipole-dipole interaction, which is proportional to r_{IS}^{-3}, where r_{IS} is the internuclear distance:

$$b_{IS} = -\frac{\mu_0}{4\pi}\left(\frac{\gamma_I \gamma_S \hbar}{r_{IS}^3}\right) \tag{5.1}$$

Although the direct dipole-dipole interaction is attenuated during MAS, it can be reintroduced under specific experimental conditions. For an isolated pair of ^{13}C nuclei, accurate internuclear distance measurements as great as 0.6 nm within an error of as low as 0.01 nm have been reported [110],[151],[152]. R^2 has been applied to a broad variety of biological systems, including membrane-bound α-helical peptides [153], bacteriorhodopsin[110],[154], prion fragments [155], the gastric proton pump [52] and β-amyloid protein of Alzheimer's disease [151],[156].

For homonuclear spin pairs at rotational resonance, the dipolar couplings may partially reappear, when the spinning speed in a MAS experiment is adjusted to satisfy the condition

$$\Delta\omega_{iso} = n\omega_r \tag{5.2}$$

where $\Delta\omega_{iso}$ is the isotropic chemical shift difference, n a small integer and ω_r the sample spinning speed. Reintroducing the dipolar coupling leads to two important effects, namely broadening and splitting of usually well resolved MAS resonance lines and an enhancement of Zeeman magnetization exchange [29],[157]. The linebroadening effect has been used in one application to ^{13}C-labelled retinal [158], while all other applications to biological systems were performed by analysing magnetisation exchange, which is also the approach used here.

The rotational resonance condition is illustrated in Fig.5.3 for M13[α29,30] in DMPC bilayers. The spinning speed has to match the chemical shift difference between $^{13}C\alpha$-Val29 and ^{13}C=O-Val30. Their positions are labelled in the spectrum. The pulse sequence needed for recording magnetisation exchange is shown in Fig.5.4.

Initial magnetisation is generated with a 2.5ms cross-polarisation pulse, with a ramp-amplitude on the ^{13}C channel to enhance the signals from both sites of the dilute spin pair. The ramped CP-pulse helps to minimize effects of Hartman-Hahn mismatch at high spinning speeds [159]. A non-selective 90° pulse restores magnetisation to the z-axis, which is followed by a DANTE inversion sequence to invert the C=O resonance line in order to create a non-equilibrium situation for the spin system [160], with opposite Zeeman magnetisation for both spins. The spin system is now allowed to evolve freely for a variable mixing time τ under strong proton decoupling. Transverse magnetisation at the end of the mixing period is finally created by a strong 90° pulse. The experiment is repeated for a

set of mixing times between 0 and 40 msec. The result can be presented as the time course of difference magnetisation $<I_Z\text{-}S_Z>(\tau)$. Comparison with simulated exchange curves for particular molecular structures now allows extraction of the dipolar coupling.

The theoretical background for simulations has been described in detail by Levitt et al.[30]. Here, only a rather brief summary is given after introducing the parameters which have to be known for simulating Zeeman magnetisation exchange. The spin system is characterized by

- the principal values of chemical shift tensors of spins I and S
- the relative orientations of both chemical shift tensors with respect to each other (see Fig.5.5)
- the through space dipolar coupling between both spins
- the relative orientation of the through space dipolar coupling with respect to the chemical shift tensors (see Fig.5.5)
- the isotropic J-coupling between sites
- the zero-quantum relaxation time constant T_2^{ZQ}, which is a phenomenological parameter and describes the coupling of both spins with the environment

The size of the chemical shielding tensors can be easily determined from low speed MAS spectra while the J-coupling, which has only a small influence, can be estimated from solution data. The dipolar coupling is usually the parameter to be determined. Care has to be taken with the orientation of the chemical shift tensor, since they depend on the molecular structure, which is actually the final goal of the experiment. It has been shown however, that at the resonance condition n=1, tensor orientations have only minor effects to the magnetisation exchange [30]. Alternatively, once the dipolar coupling has been measured, magnetization exchange at higher resonance orders can be used to estimate the tensor orientations, which has been demonstrated in a study on bacteriorhodopsin [161] and amyloid fibres[162]. The parameter T_2^{ZQ} is not directly accessible by experimental means, but it was shown, that a lower limit can be estimated from the linewidths of both sites [157]:

$$T_2^{ZQ} \geqslant \frac{1}{\pi(\Delta\nu^S_{1/2} + \Delta\nu^I_{1/2})} \tag{5.3}$$

Let us now briefly outline the theoretical background for describing Zeeman magnetisation exchange at rotational resonance.

The Hamiltonian for an isolated pair of coupled, homonuclear spins I and S in a rotating solid, in the absence of radiofrequency pulses and in the rotating frame is given in the high field approximation as (see also Chapter 1):

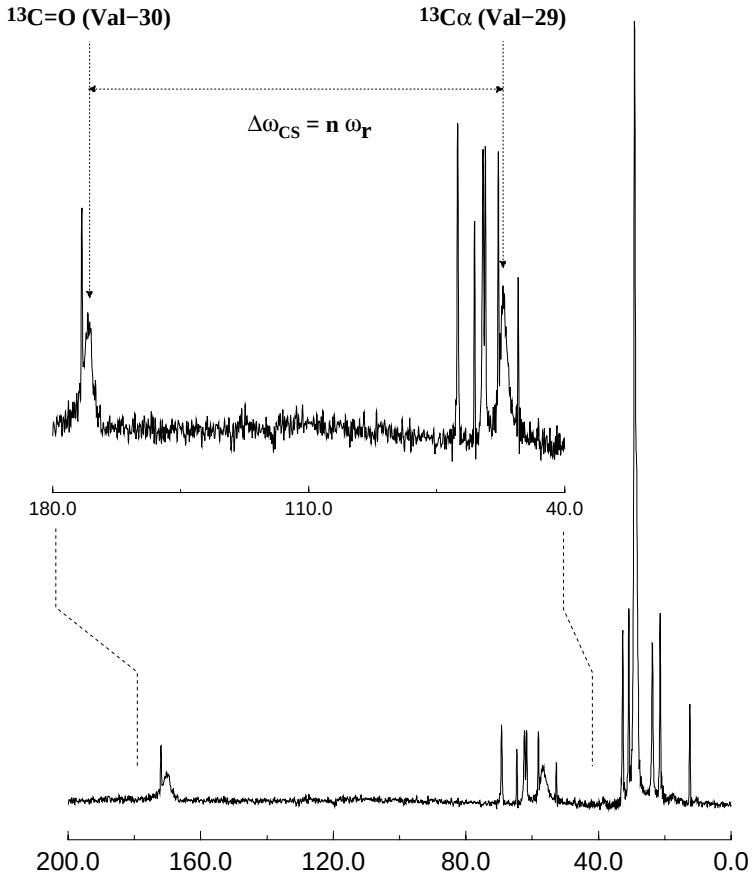

Figure 5.3: ^{13}C-CP-MAS spectrum of M13 coat protein reconstituted in DMPC bilayers (L/P=30) at 25^{o}C and ω_r=10000Hz. The protein was labelled according to the scheme in Fig. 5.2. If an integer multiple of the spinning speed ω_r matches the chemical shift difference between both labelled sites, the homonuclear dipolar coupling is partially reintroduced and can be measured.

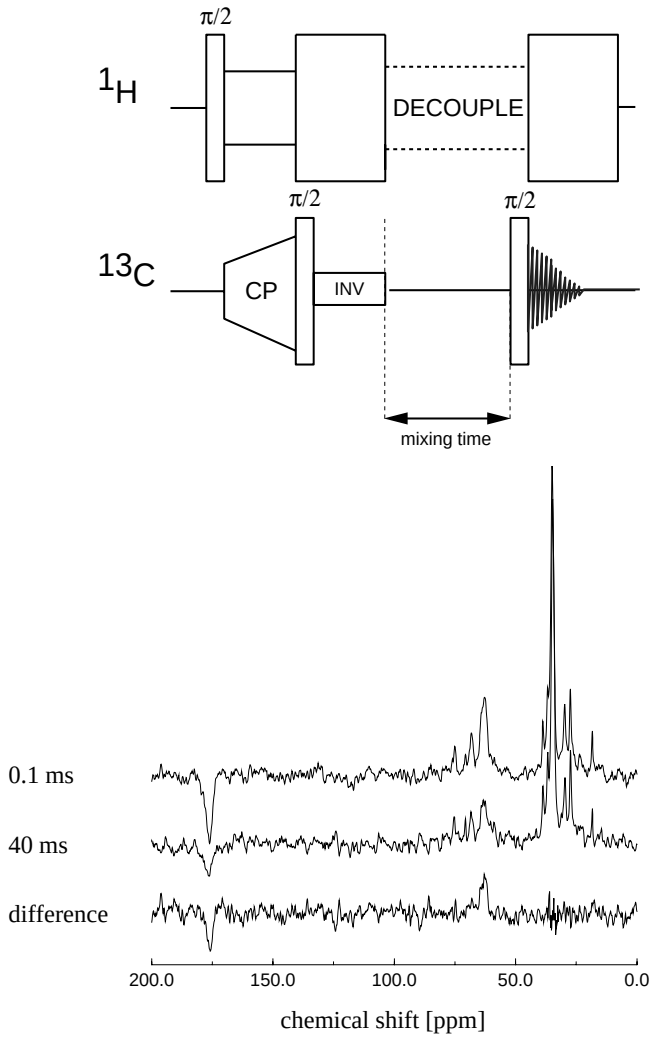

Figure 5.4: Pulse scheme for rotational resonance: Initial magnetisation is generated with a 2.5ms cross-polarisation pulse, with a 40% ramp-amplitude on the ^{13}C channel. A DANTE inversion sequence inverts the C=O resonance line in order to create a non-equilibrium situation for the spin system. Longitudinal magnetisation is created by a $\pi/2$ pulse. Magnetisation exchange takes place for a variable mixing time. Spectra from M13[α29,30] were recorded at n=2 resonance condition. Maximum exchange is achieved at 40ms mixing time.

$$\begin{aligned}\mathcal{H}(t) &= \mathcal{H}^I_{CS}(t) + \mathcal{H}^S_{CS}(t) + \mathcal{H}_{IS}(t) \\ &= \omega_I(\Omega^I_{PL}(t))I_Z + \omega_S(\Omega^S_{PL}(t))S_Z + \mathcal{H}_{IS}(t)\end{aligned} \tag{5.4}$$

where I_Z and S_Z are the z-components of the angular momentum of I and S with the Larmor frequencies $\omega_I(\Omega^I_{PL}(t))$ and $\omega_S(\Omega^S_{PL}(t))$. The spin-spin coupling contains contributions from isotropic J-coupling and dipolar coupling:

$$\mathcal{H}_{IS}(t) = 2\pi J_{iso}\mathbf{I}\cdot\mathbf{S} + b_{IS}d^2_{00}(\beta^{IS}_{PL}(t))(3I_zS_z - \mathbf{I}\cdot\mathbf{S}) \tag{5.5}$$

With the relation

$$\mathbf{I}\cdot\mathbf{S} = \frac{1}{2}\left(I^+S^- + I^-S^+\right) + I_zS_z \tag{5.6}$$

for the general form of the homonuclear two-spin Hamiltonian for a coupled spin-1/2 pair system in a rotating solid, in the absence of a radio-frequency field is obtained [163]:

$$\begin{aligned}\mathcal{H}(t) &= \omega_I(t)I_Z + \omega_S(t)S_Z + \omega_A(t)2I_ZS_Z + \omega_B(t)\frac{1}{2}\left(I^+S^- + I^-S^+\right) \\ \omega_A(t) &= \pi J_{iso} + b_{IS}d^2_{00}(\beta^{IS}_{PL}(t)) \\ \omega_B(t) &= 2\pi J_{iso} - b_{IS}d^2_{00}(\beta^{IS}_{PL}(t))\end{aligned} \tag{5.7}$$

By neglecting spin-lattice relaxation on the magnetization exchange timescale, the whole exchange process can be discussed within a fictitious spin-1/2 space formed by the two central levels of the four-level two-spin system [30]

$$|2\rangle = \left|+\frac{1}{2}, -\frac{1}{2}\right\rangle, |3\rangle = \left|-\frac{1}{2}, +\frac{1}{2}\right\rangle \tag{5.8}$$

which can be used to reduce the Hamiltonian to

$$\mathcal{H}^{(23)}(t) = \omega_\Delta(t)I^{(23)}_Z + \omega_B(t)I^{(23)}_X \tag{5.9}$$

The Hamiltonian represents a fictitious field in {|2>,|3>}subspace, with the z-component given by the difference in precession frequencies of both spins

$$\omega_\Delta(t) = \omega_I(t) - \omega_S(t) \tag{5.10}$$

and the x-component $\omega_B(t)$ represented by the non-secular dipolar coupling. Both coefficients are periodically time-dependent because of sample rotation, and it is of advantage for further discussions to express them in terms of their Fourier components.

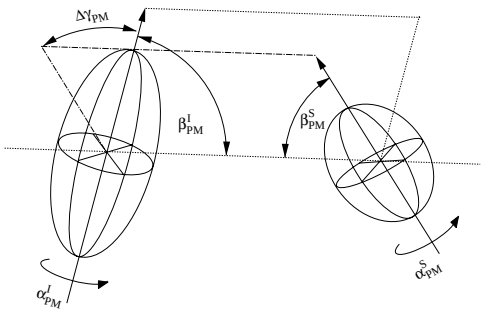

Figure 5.5: Definition of the relative tensor orientations of site I and S: α describes rotations about the z-axis of each tensor, β the tilt of the z-axis with respect to the internuclear vector and $\Delta\gamma$ is the angle between the planes formed by the internuclear vector and the z-axes.

$$\omega_B(\Omega_{PM}, \Omega_{MR}, t) = \sum_m \omega_B^{(m)}(\Omega_{PM}, \Omega_{MR}) \exp(im\omega_r t) \tag{5.11}$$

$$\omega_\Delta(\Omega_{PM}, \Omega_{MR}, t) = \sum_m \omega_\Delta^{(m)}(\Omega_{PM}, \Omega_{MR}) \exp(im\omega_r t) \tag{5.12}$$

Explicit terms for $\omega_B^{(m)}(\Omega_{MR})$ and $\omega_\Delta^{(m)}(\Omega_{PM}, \Omega_{MR})$ are given by Levitt et al. [30]. Both terms depend on magnitude and orientation of shielding and dipolar coupling tensors. The Euler angles Ω_{MR} describe the orientation of the molecule fixed frame MF with respect to the rotor frame, while Ω_{PM} rotates the shielding tensors from the PAS into MF (see Fig.1.2). A powder averaging would remove the Ω_{MR} dependency, but not Ω_{PM} which contains the relative orientation of I and S with respect to each other and which reflects the molecular structure (see Fig.5.5).

At the start of the exchange period τ , the spin pair is prepared in a uniform state of Zeeman polarisation, corresponding to a density operator $\boldsymbol{\rho}^{(23)}(0)$, which describes z-polarisation in the {|2>,|3>}subspace.

$$\boldsymbol{\rho}^{(23)}(0) \sim \frac{1}{2} < I_Z - S_Z > (0) = I_z^{(23)} \tag{5.13}$$

During the mixing time τ, the state vector proceeds to nutate about the fictitious field given in Eqn.5.9. The spin density operator may be described as a vector in the space of spin operators ($I_X^{(23)}$,$I_Y^{(23)}$,$I_Z^{(23)}$) which follows the Bloch equation

$$\frac{d}{dt}\boldsymbol{\rho}^{(23)}(t) = \mathcal{W}^{(23)}(t)\boldsymbol{\rho}^{(23)}(t) \tag{5.14}$$

$$\mathcal{W}^{(23)}(t) = \begin{pmatrix} -r & -\omega_\Delta(t) & 0 \\ \omega_\Delta(t) & -r & -\omega_B(t) \\ 0 & \omega_B(t) & 0 \end{pmatrix} \tag{5.15}$$

where r=$1/T_2^{ZQ}$.The time dependence of $\omega_\Delta(t)$ and $\omega_B(t)$ can be predicted from orientation and magnitude of shielding and dipolar coupling tensors. By numerical integration over Eqn.5.14, the Zeeman magnetisation exchange trajectory $<I_Z\text{-}S_Z>(\tau)$ can now be evaluated. Averaging over Ω_{MR} is necessary for polycrystalline samples. In case of exact rotational resonance, i.e. where $\Delta\omega_{iso} = n\omega_r$, some simple expressions for the magnetisation exchange can be derived [30]. Two cases are to be distinguished by defining a parameter

$$R^2 = r^2 - 4\left|\widetilde{\omega}_B^{(n)}\right| \tag{5.16}$$

where $\left|\widetilde{\omega}_B^{(n)}\right|$ are the resonant Fourier components of the non-secular dipolar interaction $\omega_B(t)$. For fast dephasing ($R^2>0$) one finds

$$\begin{aligned} \langle I_z - S_z\rangle(\tau) &= e^{-r\tau/2}\left[\cosh(R\tau/2) + \frac{r}{R}\sinh(R\tau/2)\right] \\ &\simeq \exp\left[-\frac{\left|\widetilde{\omega}_B^{(n)}\right|^2}{r}\tau\right] \end{aligned} \tag{5.17}$$

and for slow dephasing ($R^2<0$), the time course is described by:

$$\begin{aligned} \langle I_z - S_z\rangle(\tau) &= e^{-r\tau/2}\left[\cosh(iR\tau/2) + \frac{r}{iR}\sinh(iR\tau/2)\right] \\ &\simeq e^{-r\tau/2}\cos\left[\left|\widetilde{\omega}_B^{(n)}\right|\tau\right] \end{aligned} \tag{5.18}$$

In the first case, magnetization would decay in a monotonic way, while in the second, damped oscillations can be observed. A more general analytical solution is derived and discussed in Appendix D. In order to be able to evaluate the effect of all parameters to the final result, the simulation of magnetisation exchange curves has been combined with the non–linear minimisation software MINUIT (CERN software library), which allows each single parameter and each parameter combination to be fitted to an experimental data set (see Appendix C).

A physical picture of the rotational resonance phenomenon is easily accessible in the framework presented above. If the chemical shift difference is always large compared to the dipolar coupling, i.e. $\omega_\Delta(t) \gg \omega_B(t)$ in Eqn.5.9, then the fictitious field remains close to the z-axis and so all solutions of the Bloch equation 5.14 would be close to the initial state, i.e. no magnetisation exchange would be

observed. On resonance however, $\omega_B(t)$ would have components which match the chemical shift difference and so $\omega_\Delta(t)$, which means that the density state vector moves away from the initial state under the influence of the oscillating field $\omega_B(t)$, which is observed as an exchange of Zeeman polarization between I and S. This situation is illustrated in Fig.5.4, where the intensities of the ^{13}C=O and ^{13}Cα resonance lines decay significantly after a sufficient period τ.

5.1.4 MAOSS on Spin-1/2 Systems

While rotational resonance experiments on unoriented samples provide detailed and precise information about local conformation, NMR experiments on oriented membranes would provide additional orientation constraints. The case to be discussed here is slightly different from the situation presented for ^{2}H-MAS on oriented bR in Chapter 4, where the orientation Ω_{PM} of a chemical group with respect to the molecular (protein) fixed frame was measured. Here, it is the chemical shift tensor of spin-1/2 nuclei whose orientational distribution functions in the molecular fixed frame is known and which would allow measurement of the orientation Ω_{MD} of a protein segment with respect to the membrane normal to be made. This could be, for example, the tilt of an α-helix in the membrane.

The advantages of MAS on oriented systems using the chemical shift anisotropy of spin-1/2 nuclei such as ^{15}N or ^{13}C are found in

- a significant spectral response to small tilt angles
- a good spectral sensitivity and resolution due to MAS averaging of remaining disorder in the oriented sample and
- the conservation of the isotropic chemical shift in MAS resonance line I_0, while orientation information is stored in spinning sidebands, which is important for resonance assignment in multiply labelled systems.

To explain the first point, briefly reconsider Eqn.1.24 derived in Chapter 1 for the general angle dependency of the chemical shift ω_{CS}, which is given as:

$$\omega_{CS} = \gamma B_0 \left(\begin{array}{c} \sigma_{iso} + \\ \delta \frac{\left(3\cos^2\theta - 1\right)}{2} \left(\frac{\left(3\cos^2\beta_{PR} - 1\right)}{2} - \frac{\eta}{2}\sin^2\beta_{PR}\cos 2\alpha_{PR} \right) + \\ \delta\left(\widetilde{C_1} + \widetilde{S_1} + \widetilde{C_2} + \widetilde{S_2}\right) \end{array} \right) \tag{5.19}$$

where $\widetilde{C_1}$,$\widetilde{C_2}$,$\widetilde{S_1}$ and $\widetilde{S_2}$ are modified MAS coefficients given in their explicit form in Eqn.1.25, but here, only relationships which are important for the further discussion are shown:

$$\begin{aligned}
\widetilde{C_1} &= \cos(\omega_r t) \times \sin 2\theta \times f(\alpha_{PR}, \beta_{PR,}\gamma_{PR}, \eta) \\
\widetilde{S_1} &= \sin(\omega_r t) \times \sin 2\theta \times f(\alpha_{PR}, \beta_{PR,}\gamma_{PR}, \eta) \\
\widetilde{C_2} &= \cos(2\omega_r t) \times \sin^2\theta \times f(\alpha_{PR}, \beta_{PR,}\gamma_{PR}, \eta) \\
\widetilde{S_2} &= \sin(2\omega_r t) \times \sin^2\theta \times f(\alpha_{PR}, \beta_{PR,}\gamma_{PR}, \eta)
\end{aligned} \tag{5.20}$$

In the static -non spinning- case, i.e. where ω_rt=0, $\widetilde{S_1}$ and $\widetilde{S_2}$ would vanish and only $\widetilde{C_1}$and $\widetilde{C_2}$ remain. These expressions describe the rotations of the CSA tensor from the PAS into the rotor frame RF and from there into the laboratory frame. Since in this experimental situation the membrane director Z_D is identical with the rotor axis Z_R, the expression for ω_{CS} can be used to discuss angle dependences for different membrane orientations in the magnetic field. To be more specific, consider a small membrane spanning α-helical peptide, which is specifically ^{15}N labelled. The close to axially symmetric ^{15}N chemical shift tensor has its principal element $\sigma_{||}$ approximately parallel to the N-H amide bond, which can be used to define in first order the helix normal Z_M [164],[165]. Following the discussions about distributions and transverse isotropy in membranes from Chapter 3, only the tilt angle β_{PR} needs to be considered here, which is now identical with the tilt angle between the helix axis Z_M and the membrane normal Z_D and which would be reflected in the anisotropic chemical shift from the labelled site in the protein backbone.

By placing the membrane normal parallel to the magnetic field (θ=0°), Eqn.5.19 simplifies, since $\widetilde{C_1}$and $\widetilde{C_2}$ vanish and a unique anisotropic chemical shift can be observed for each tilt β_{PR} , which has been used extensively for studying membrane proteins by static solid-state NMR [36]. An illustration can be found in Fig.5.6a, which also underlines a potential problem with that approach. Although the resonance line shifts with the helix tilt, changes in angles in the range of 0° to 30° are relatively small (ca. 5% of the full anisotropy) and they are therefore difficult to measure, unless the sample has an excellent degree of order (mosaic spread $\Delta\beta = 0°$). The most dramatic changes are actually found in the region about 54.7°, which can be easily evaluated by taking the first derivative $\partial\omega_{CS}/\partial\beta_{PR}$ of Eqn.5.19, while for $\beta_{PR} = 0°$ the lowest slope is found. This fact can be utilized by orienting the membrane normal at $\theta = 54.7°$. If the helix axis Z_M and so the chemical shift tensor axis Z_P are exactly parallel to the membrane normal Z_D, a sharp resonance line at the position of the isotropic chemical shift would be observed, while small tilt angles would already cause dramatic and characteristic changes, which is compared to the case discussed before in Fig.5.6b. However, the price to pay for this improvement in "angle resolution" is a lower spectral sensitivity and spectral resolution, because the complicated angle dependences would cause relatively broad and complex lineshapes. This problem can be solved by sample spinning at the magic angle, shown in Fig.5.6c. The observed wideline

spectra would decay into well resolved spinning sideband pattern, which occur about the isotropic chemical shift. In this situation, all orientational information is obtained in the spinning sidebands, which can be analysed by

$$I_N(\alpha_{PM},\beta_{PM},\beta_{MR},\Delta\beta) = K\int_0^{2\pi} d\alpha_{MR}\int_0^{2\pi} d\gamma_{MR}\int_{\beta_{MR}-\Delta\beta}^{\beta_{MR}+\Delta\beta} d\beta_{MR} \times p_{MR}(\beta_{MR})I_N(\alpha_{PM},\beta_{PM},\alpha_{MR},\beta_{MR},\gamma_{MR}) \quad (5.21)$$

as discussed in detail in Chapter 3 and Chapter 4, while at the same time information about the isotropic chemical shift is conserved, which is of importance for resonance assignment in multi-spin systems.

For the study presented here, the anisotropy of the ^{13}C=O tensor in Val-29 of M13 coat protein has been used to measure the protein orientation in the membrane. The orientation of carbonyl tensors in peptide planes are well characterized by NMR and computational studies [165],[166],[167]. The most shielded component σ_{33} in extended sheet and helical conformation lies along the director of the peptide plane. The component that lies close to the C=O bond is σ_{22}. The least shielded component also lies in the amide plane and is perpendicular to the C=O bond [168]. Generally, the orientation of the C=O shielding tensor for all amino acids is intimately related to the amide plane and the direction of the C=O bond, which is illustrated in Fig. 5.7. The angle λ_1, that σ_{22} makes with the C=O bond, has been determined to be between 0° and 30° from single crystal studies and solid state NMR experiments on various model compounds [165],[166],[167]. The angle λ_2 in Fig. 5.7 relates the orientation of the C=O bond vector with respect to the molecular long axis Z_M, which can be defined for a α-helix by the average of all N-H bond vectors. The angle between C=O and N-H bonds in an ideal peptide plane can be assigned to λ_2 and is 3.7° [169]. The sensitivity of a ^{13}C=O spectrum to different helix orientations by oriented static and MAOSS NMR, is shown in Fig.5.8. The simulations represent the same physical situation as discussed before for ^{15}N, but here, the z-axis of the PAS (σ_{33}) is perpendicular to the helix and the C=O tensor has an asymmetry parameter of η=0.82.

The finding that the C=O shielding tensor orientation in the amide plane is almost conformationally or residue independent, makes it an excellent probe for protein structures, which is however limited by the fact that the carbonyls have only a small isotropic chemical shift distribution and also the natural abundance background of 1% complicates the analysis of data from single labelled systems. Nevertheless, it will be shown for the example of ^{13}C=O in Val-29 of M13, that in principle MAOSS experiments on spin-1/2 nuclei can be used for membrane protein structure determination.

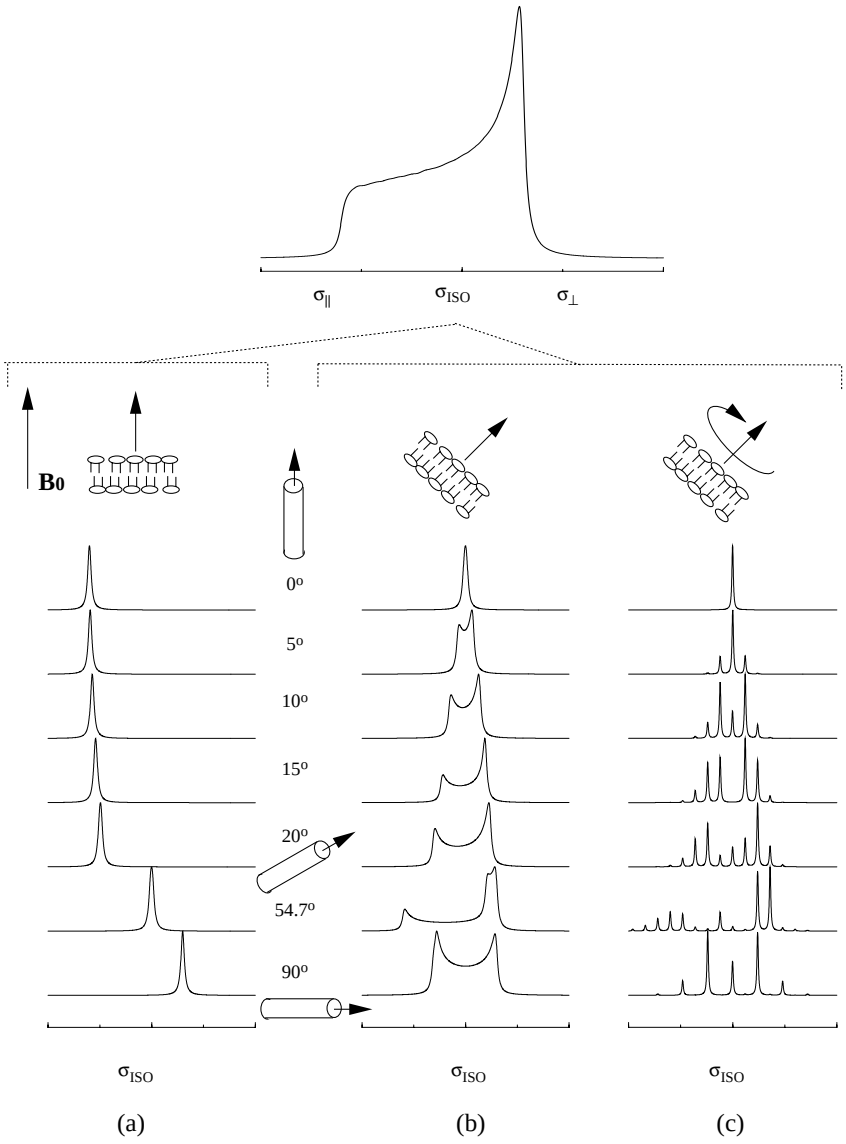

Figure 5.6: Measuring the tilt of an α-helical peptide in the membrane from the anisotropic chemical shift of a ^{15}N label in the peptide backbone: membrane normal parallel to the magnetic field (a), membrane normal at the magic angle (b), membrane normal at the magic angle with sample spinning (c). The angular resolution is better in (b) than in (a), but spectral resolution and sensitivity is improved by sample spinning (c). In (c), orientational information is contained in the spinning sidebands, which appear around the central line at the isotropic chemical shift.

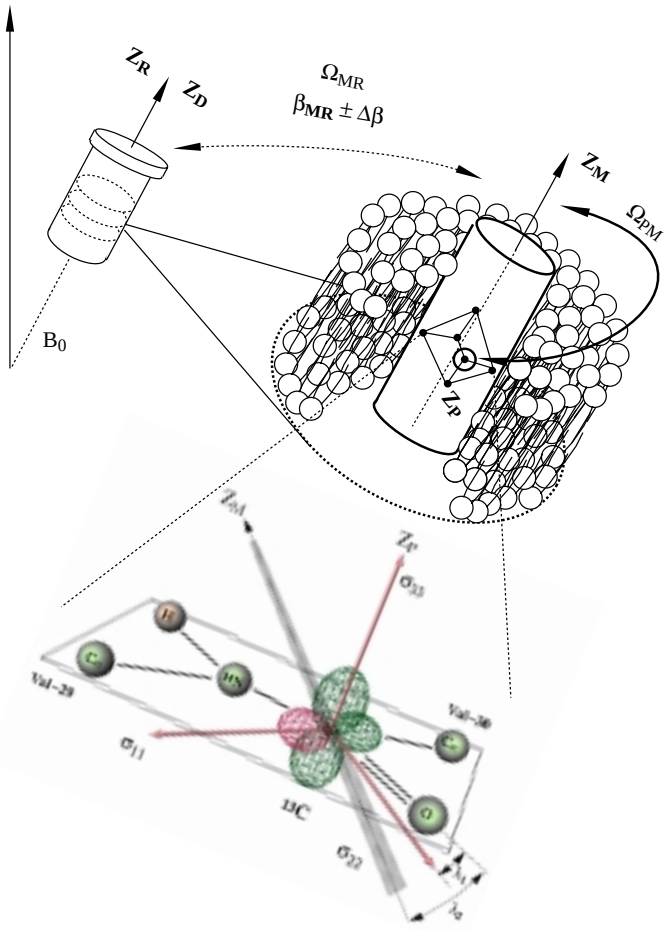

Figure 5.7: Reference frames for a carbonyl labelled site in a protein backbone. Here, the orientational distribution function of β_{MR}, which requires the knowledge of Ω_{PM}, is to be determined. The largest element of the chemical shift tensor of ^{13}C=O is perpendicular to the peptide plane and so approximately perpendicular to Z_M, while σ_{22} is nearly parallel to the C=O bond vector (see text for detailed discussion).

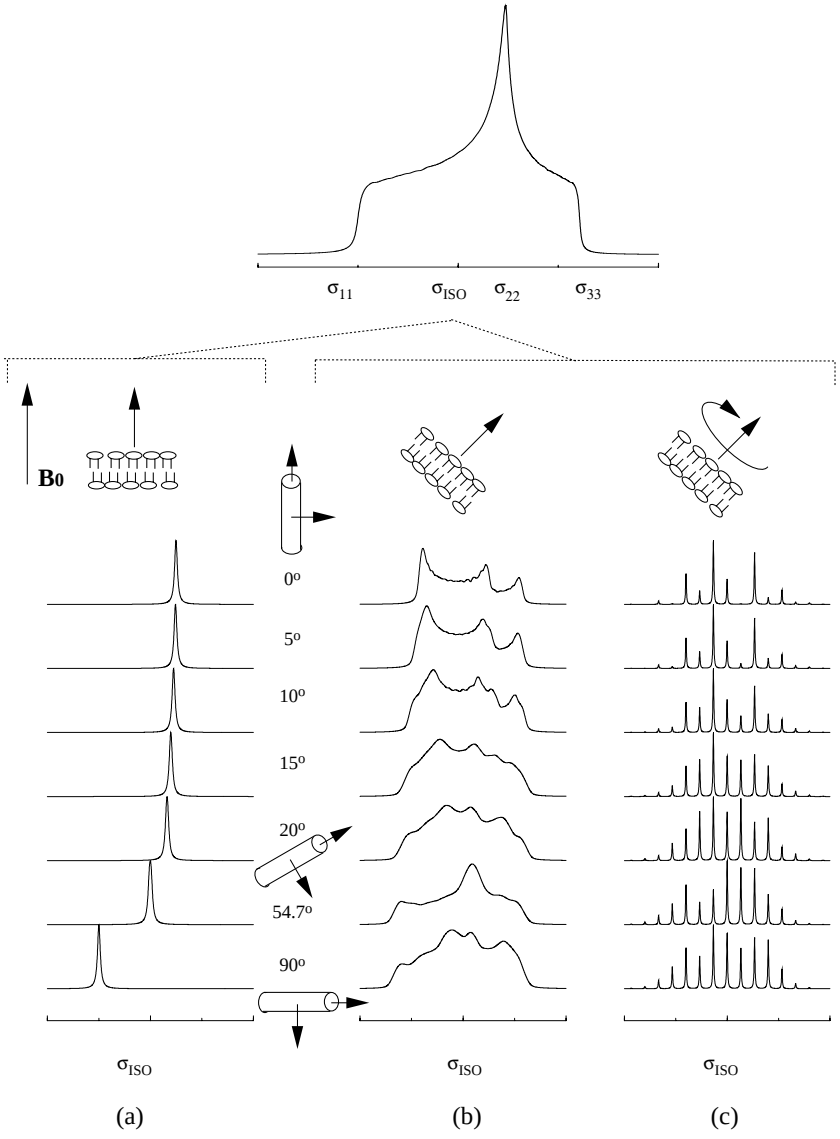

Figure 5.8: Measuring the tilt of an α-helical peptide in the membrane from the anisotropic chemical shift of a ^{13}C=O label, with a orientation shown in Fig. 5.7, with the membrane normal parallel to B_0 (a), at the magic angle (b), and at the magic angle with sample spinning (c).

5.2 Materials and Methods

5.2.1 Sample Preparation and Orientation

L-α−DMPC was obtained from Sigma (UK) and used without further purification. Two doubly ^{13}C labelled samples of M13 coat protein were synthesized using standard solid-phase FMOC chemistry and purified at the NSR Centre, Nijmegen, The Netherlands. For the synthesis, Asp-5 had to be replaced by Asn. The labelled positions in the first sample (M13[α29,30]) were ^{13}Cα in Val-29 and ^{13}C=O in Val-30 and in the second (M13[29,α31]) ^{13}C=O in Val-29 and ^{13}Cα in Val-31, as illustrated in Fig.5.2. [^{13}Cα]Val and [^{13}C=O]Val were purchased from Cambridge Isotope Laboratories, from which FMOC derivatives were prepared in our laboratory. The purity of the synthesized peptide was found to be over 90% as measured by HPLC and mass spectroscopy.

M13 coat protein was incorporated into DMPC bilayers at a lipid to protein molecular ratios of usually 20:1 using a procedure described before [148]. The peptide is quickly dissolved in excess of TFA (10mg peptide in 200 μl TFA) in order to break up any aggregates. After removing TFA under a stream of nitrogen, the remaining peptide film was resuspended by adding 5ml of TFE which was allowed to evaporate to remove any traces of the acidic TFA. The peptide film was then dissolved in 0.5 ml TFE. Reconstitution buffer (10mM NaH_2PO_4, 0.2mM EDTA, 140mM NaCl, 150 mM NaCholate, pH 7.8) was added subsequently in 0.5ml aliquots under vortexing to obtain a clear solution of 8 ml volume. The appropriate amount of lipid (DMPC) was solubilized in 3ml of the same buffer and added to the M13 solution. After vortexing and incubation for 30min at 30°C the solution was transferred into a dialysis tube and dialysed against 1 litre of NaCholate free dialysis buffer (10mM NaH_2PO_4, 0.2mM EDTA, 140mM NaCl, pH 7.8) at 4°C over a period of two weeks. The dialysis buffer was partially (50%) renewed every 24 hours. After completed reconstitution, vesicles were pelleted and resuspended in dialysis buffer and placed on a linear sucrose gradient (0-40% weight/weight). Centrifugation in a SW28 swing bucket rotor (Beckman, USA) was carried out for 12 hours at 4°C and 90000g. A single layer at 22% w/w sucrose was found, which indicates a homogeneous reconstituted sample. The layer was recovered and sucrose was removed by several washing steps. Finally, the sample was resuspended in dialysis buffer solution and pelleted. CD spectroscopy indicated a high percentage of α-helical conformation.

For rotational resonance NMR experiments, samples were centrifuged into a Bruker 4mm MAS rotor. Oriented M13 samples for MAOSS experiments were prepared by covering precisely cut glass disks (5.4mm diameter, 0.1mm thickness, Marienfelde GmbH) with 0.3mg material in 25μl diluted buffer solution. Bulk water was allowed to evaporate over 24 hours at 4°C. Macroscopic order in the sample was prechecked using polarized light microscopy. Disks were stacked on top of each other and rehydrated at 30°C and relative humidity of 93% over five

days. Finally, the disks were transferred into Bruker 7mm MAS rotors using specifically designed tools as described in Appendix A. KelF inserts were placed on top of the disks in the MAS rotor in order to allow a stable positioning under MAS spinning conditions.

5.2.2 NMR Experiments

All NMR experiments were performed at 100.63 MHz for ^{13}C and 400.13 for ^{1}H on a BRUKER MSL 400. Rotational resonance data were acquired using a double resonance Bruker 4mm probe. Typical 90° pulse length was 4 and 6μs for ^{13}C and ^{1}H. Cross polarisation was accomplished using a ramped-amplitude contact pulse sequence (Fig.5.5), which improves signal intensity and stability at high spinning speeds [159]. A CP contact time of 2.5 ms, a repetition delay time of 2.0 sec and a decoupling power of 60 kHz were applied. The carbonyl resonance was selectively inverted using a DANTE inversion sequence [160]. The acquisition order of different RR mixing times was randomized and control points were included in order to check amplifier instabilities. For each mixing time, a total of 2048 FIDs was collected. The spinning speed was controlled to within $\pm 2Hz$ by a homebuilt MAS synchronizer. Temperature was regulated by a Bruker BT3000 temperature control unit. Experiments were performed at temperatures between 260 and 310K.

CP-MAOSS experiments were performed on a Bruker 7mm double resonance probe at 260K. The same speed controller was used to control and stabilise the spinning speed within a range of $\pm 4Hz$. Sample stability was checked before and after sample spinning by static ^{1}H and ^{31}P NMR.

The chemical shift tensors were determined by sideband analysis from low speed MAS spectra in the labelled amino acids before synthesis and in the solid, synthesized peptide. For both $^{13}C\alpha$, σ_{iso}=64.3ppm, δ =-10.70 ppm and $\eta = 0.3$ were found. The ^{13}C=O tensors are characterised by σ_{iso}=175.1ppm,δ =-72.28 ppm and η=0.82.

Spectra were analysed using Felix (Biosym). Numerical simulations were performed on Silicon graphics INDY 5600 workstations.

5.3 Results and Data Analysis

5.3.1 Rotational Resonance: Determination of Internuclear Distances

Although many attempts were undertaken to observe magnetisation exchange trajectories at n=1 rotational resonance condition which corresponds at the used field of 9.8 T to a spinning speed of ω_r=11146.5 Hz, it was not possible to stabilize the rotor at this speed within a sufficient rotor speed accuracy over a necessary

period of time. Sample freezing prevented spinning, due to the formation of ice crystal at the rotor caps at low temperatures. Experiments at higher orders of resonance however, were possible without problems.

Magnetisation exchange experiments with only a few data points were performed at various temperatures in order to evaluate the effect of molecular motions. If a labelled molecule undergoes fast anisotropic reorientations, the dipolar coupling would be projected onto the long axis and analysing rotational resonance effects would yield an incorrect distance. Here, no significant difference in the magnetisation exchange rate at temperatures between -10 and $25°C$ were found, which corresponds to the NMR dynamic studies on M13 suggesting that the hydrophobic domain (res. 21-39) is motionally restricted on the NMR time scale [77],[82],[85],[150].

Intensities of the ^{13}C=O and $^{13}C\alpha$ resonances were determined by integration. A natural abundance correction was performed by analysing the spectrum of unlabelled M13 coat protein. Zeeman magnetization exchange trajectories at n=2 resonance condition and at T=4°C for the samples M13[α29,30] and M13[29,α31] are shown in Fig.5.9.

A significant decay is observed for both samples over a mixing time of $\tau = 40ms$. As mentioned before, at n=2, orientations of the shielding tensors for I and S have significant effects on the Zeeman magnetisation exchange trajectory, which would make data analysis a difficult task without assuming a certain molecular conformation prior to data analysis [170]. Here, an alternative approach has been used. The powder averaged signal depends on five Euler angles $\alpha^I_{PM}, \beta^I_{PM}, \alpha^S_{PM}, \beta^S_{PM}$ and $\Delta\gamma_{PM} = \gamma^I_{PM} - \gamma^S_{PM}$ describing the orientation of the CSA tensors I and S with respect to each other and with respect to the molecular frame MF (see Fig.5.5 and Fig.1.2.). Since the chemical shift anisotropy of the Cα CSA tensor is much smaller and nearly symmetrical compared to C=O, the molecular frame MF can be chosen to be identical with the principal axis system of Cα and with the dipolar coupling tensor. This leaves five unknown parameters in the data anlysis; three Euler angles, the dipolar coupling and T_2^{ZQ}. A lower limit of 2 msec for the latter could be estimated from the linewidth of $^{13}C\alpha$ and ^{13}C=O, used by the minimisation software for defining boundaries for T_2^{ZQ}. The experimental exchange curves were now fitted by stepping the distance r_{IS} from 0.2 to 0.6 nm in 0.01 nm steps while searching for the best fit for each step by varying the C=O tensor orientation and T_2^{ZQ}. This was done both by the Monte Carlo method and by a non-linear minimisation procedure using the software described in Appendix C.

The χ^2 value for the best fit was used to compare fitting results for different distances with each other. The result is plotted over the experimental data in Fig.5.9. It is shown that a best fit with $\chi^2 \simeq 10^{-4}$ can be obtained for distances of r_{IS}= 0.4±0.05nm for M13[α29,30] and r_{IS}= 0.45±0.05nm for M13[29,α31], which is in the range expected for an α-helical conformation. The presented approach allows n=2 exchange curves to be analysed without prior knowledge of a

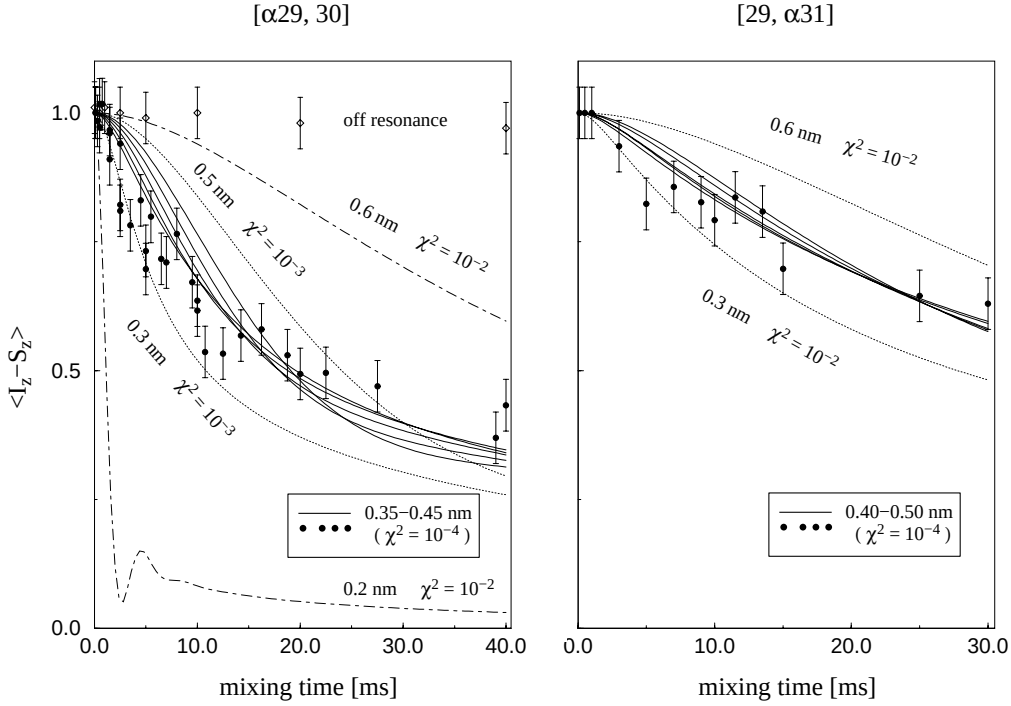

Figure 5.9: Magnetisation exchange curves for M13[α29,30] and M13[29,α31] at n=2 rotational resonance condition. All experimental points are plotted with error bars. An off resonance exchange curve for M13[α29,30] does not show any decay, while on resonance, a magnetisation exchange is observed. Data were analysed by fitting the relative tensor orientations and T_2^{ZQ} within certain limits and for a set of fixed distances to the exchange curves (see text for details). This procedure yields a distance of 0.4±0.05 nm for [α29,30] and 0.45±0.05 nm for [29,α31] without making any assumptions about relative tensor orientations.

molecular structure, which is however reflected in a larger error on the distances. More accurate data could be obtained at n=1. The results were checked with a simulation which assumes a tensor orientation corresponding to a α-helical structure and which returns distances within the determined limits. Typical fitting results for T_2^{ZQ} were between 3 and 8 msec, which is in the range of values used throughout the literature for comparable systems [171]. Both resonances were inhomogeneously broadened to 300 Hz. The effect of inhomogeneous linebroadening to the rotational resonance analysis has been evaluated using the procedure described in Appendix D, but it was found to be negligible within the determined error limits [172].

5.3.2 MAOSS Spectroscopy: Tilt Angle Determination

A MAS spectrum of oriented M13[α29,30] is shown in Fig.5.10, with the signal from ^{13}C=O-Val-30 enlarged. The spectrum was acquired at 1250 Hz spinning speed at a temperature of -10°C. The orientation of the ^{13}C=O tensor to the molecular frame has to be known in order to be able to analyse this spectrum in terms of orientation of the protein with respect to the membrane normal. The molecular frame is here defined by the molecular long-axis Z_M. As discussed before, the ^{13}C=O shielding tensor has its largest element, σ_{33}, which is here used to define Z_P, perpendicular to the peptide plane, and σ_{22} lies almost parallel along the C=O bond (see Fig.5.7). This information, together with an idealized α-helical model of the transmembrane domain of M13 (residues 21-39), agrees with the rotational resonance distance constraints and has been used to estimate the Euler angles α_{PM}, β_{PM}, which relate the shielding tensor to the molecular frame MF. In the definition of Euler angles used here (see Chapter 1), α_{PM} describes rotations about Z_P while β_{PM} rotates the tensor about the new y-axis, defined by σ_{22}. The angle α_{PM} corresponds to λ_1-λ_2 in Fig.5.7. Here we used for the simulations β_{PM} values between 80° and 90°. The angle α_{PM} can not be chosen arbitrarily as for the case of ^{2}H in Chapter 4, since the C=O tensor has a large asymmetry (η=0.82). With the assumptions made above, we would obtain for α_{PM} ca. 0°-15°, depending on the actual orientation of the CSA tensor in the peptide plane. By evaluating many different orientations, we found that the spectral simulations are much more sensitive to β_{PM} than to α_{PM}.

The same fitting routine as described in Chapter 4 for ^{2}H has been used here, with the difference that β_{MR}, which is the angle between Z_M and Z_R/Z_D, was subject to optimization. A χ^2 plot is shown in Fig.5.10, which reveals a minimum at β_{PM} =20°. The second local minimum at 80° is a mirror image of that angle as illustrated for the synthetic data set in the same diagram. The appearance of ambiguous solutions can be explained by examining Eqn.5.19 which is plotted for various angle combinations in Fig.5.11. The chemical shift, referenced to the isotropic value, is plotted over different membrane orientations in the magnetic field θ and β_{PR} for three different values of α_{PR} in the left column. The right

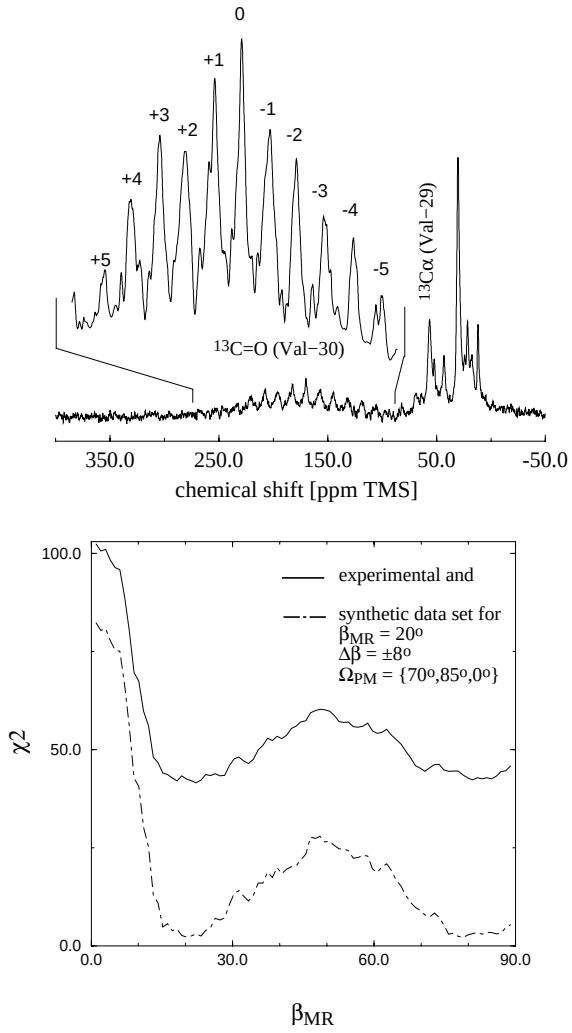

Figure 5.10: Analysis of the spinning sideband pattern of ^{13}C=O in Val-29 in oriented M13 coat protein. The CP-MAS spectrum was obtained at ω_r=1250Hz and T=-10^{o}C. The estimated mosaic spread was $\Delta\beta$=$\pm$8^o. A best fit is obtain for a helix tilt of β_{MR}=20^o $\pm$ 10^o.

column shows the same, but here for three distinct membrane orientations and all possible tensor orientations $\{\alpha_{PR}, \beta_{PR}\}$. It can be seen that the observed signal becomes ambiguous for certain angle combination, while at θ=0° and 90° a clear solution is always obtained. Experiments at different spinning speeds would however help to overcome this problem, as discussed before (Chapter 4).

It is important to analyse potential error sources in order to estimate the accuracy of the obtained peptide plane tilt angle. The ^{13}C natural abundance of 1% creates in this 50 residue protein a contribution to the observed spectrum of about 33% and with lipids 40% (at L/P=20). However, the isotropic chemical shift of peptide backbone carbonyls is distributed over a range of 172-177 ppm, so only a broadening in the baseline of the MAS spinning sidebands would be expected. Additionally, if all residues in the protein would have a similar conformation and orientation, they would exhibit a similar spectrum to the one from the labelled site. It can be concluded, that the natural abundance adds to the experimental error, but does not change the result significantly. The same applies to the effect the different degrees of disorder would have; the fitting procedure would return the same result, but with larger uncertainty.

The measurements of carbonyl ^{13}C chemical shift tensors in peptide planes is complicated by direct dipolar interactions to the adjacent ^{14}N nucleus [164],[173]. Nitrogen-14 with a natural abundance of 99.63% has a spin I=1 and is thus a quadrupolar nucleus. In the typical magnetic fields used in solid-state NMR, the ^{14}N Zeeman interaction is only about 5-10 times larger than typical amide ^{14}N quadrupolar coupling constants (14-28 MHz from 4.6-9.8T with a quadrupolar coupling of 3.2MHz) [173]. Therefore, the high field approximation could break down and would influence the resulting dipolar coupled chemical shift powder spectrum.

It has been shown, that MAS fails to completely eliminate the coupling between ^{13}C and ^{14}N and a residual dipolar coupling b_{res} can be observed [167],[174], for which an expression has been derived by Olivieri [175] :

$$b_{res} = -\frac{3}{20}\frac{b_{IS}\chi}{\omega_I}\left(3\cos^2\beta_{EFG} - 1 + \eta\sin^2\beta_{EFG}\cos 2\alpha_{EFG}\right) \tag{5.22}$$

where b_{IS} is the dipolar coupling between both nuclei, ω_I is the Larmor frequency of ^{14}N and χ is the quadrupolar coupling constant.

$$\chi = e^2qQ/h \tag{5.23}$$

The angles α_{EFG} and β_{EFG} describe the orientation of the dipolar coupling tensor with respect to the electric field gradient tensor frame. Splittings have been actually observed in fields of up to 4.6 T [174],[167], but it is clear from the expression above, that the residual dipolar coupling decreases with increasing field strength (Larmor frequency). It can be concluded, that the ^{14}N-^{13}C coupling has a negligible influence on ^{13}C NMR MAS spectra of amides for $B_0 \geq 4.7$T [167].

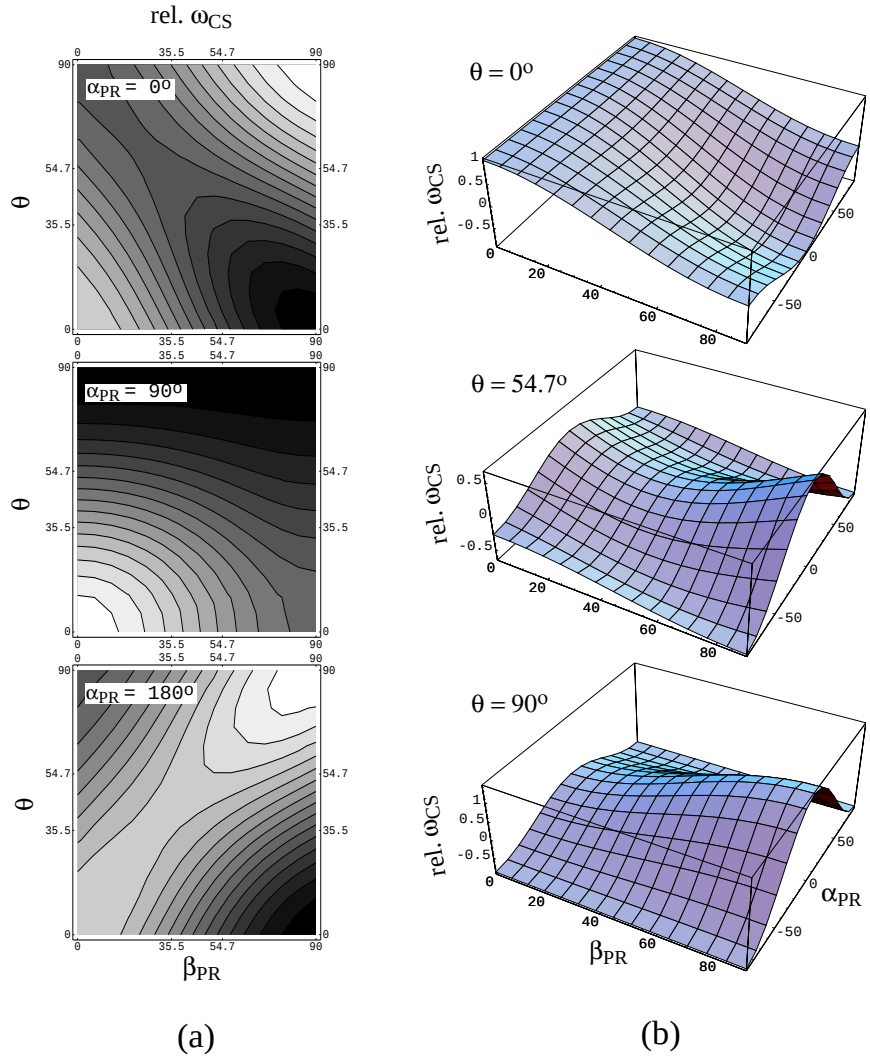

Figure 5.11: Symmetry of anisotropic chemical shift ω_{CS} for $\eta \neq 0$: (a) calculated chemical shift for different orientations of the membrane normal with respect to the magnetic field (θ) and for different orientations of the tensor's PAS with respect to the membrane system (β_{PR} and $\alpha_{PR} = 0, 90, 180°$).(b) same but here for three different values of $\theta = 0, 54.7, 90°$. It can be seen that situations can be found, in which the anisotropic chemical shift corresponds to different tensor orientations.

The best fit simulation is shown in Fig.5.12, which suggests a tilt of the protein region around residues [29-31] of $20^\circ \pm 10^\circ$.

5.4 Discussion

The distance constraints obtained from the R^2 experiments can be used to calculate dihedral angles Φ and Ψ for Val-30, as indicated in Fig.5.2. The set of all possible angle combinations was generated using the software Discover3/InsightII (Biosym, San Diego, USA) and is plotted over a Ramachandran plot created by ProCheck (Fig.5.13). The shaded region defines the angle subset, which would agree with the obtained NMR distance constraints. It can be seen that the most favoured region A, which corresponds to an α-helical structure, agrees well with the NMR distance constraints, while a β-sheet conformation can be reliably excluded. That this clear distinction between an α-helical and β-sheet structure can be made is remarkable, since the experimental error of ± 0.05nm is relatively large for rotational resonance experiments [29]. Experiments at the n=1 resonance condition or with known CSA tensor orientations, would allow a higher precision which would sharpen the Φ-Ψ distribution in Fig.5.13 even more. Spectroscopic and other experiments on M13 and similar coat proteins in lipid bilayers or vesicles, in detergents and in organic solvents generally agree to the view that M13 coat protein is largely α-helical under conditions similar to the *in vivo* state in the cell plasma membrane, but our results represent a direct proof of α-helical conformation for residues 29-31, while the protein is in the lipid bilayer [68],[81],[176],[177],[178].

Since the apolar domain of M13 coat protein has the correct length to span the hydrophobic core of the *E.coli* plasma membrane as an α-helix, an orientation parallel to the membrane normal has been suggested, which was proven by static solid state NMR experiments on oriented membranes [81]. It has been shown from the ^{15}N resonances of Leu-14, Tyr-32, Tyr-24 and Leu-41 of fd-coat protein, that the hydrophobic domain is approximately parallel and the acidic (N-terminal) domain approximately perpendicular to the membrane normal [50],[81]. The result of a slight helix tilt with respect to the membrane normal confirms and extends the model based on these findings. It does not contradict previous work, since our angular resolution for orientations about the membrane normal is higher, than for the methods (FTIR and static NMR) used before [50],[178]. Many known membrane-spanning α-helices tend to be tilted at angles between 5° and 40° with a mean of 20° [179] and it has been suggested by Marvin [140], that a tilt of the protein in the membrane would actually allow an easier insertion into the virion, in which the protein is tilted as well, which is illustrated in Fig.5.1. Interestingly, the peptide plane tilt angle of $20^\circ \pm 10^\circ$,measured for Val-29, coincides with the tilt of 20° of residues 28-32 in the bacteriophage with respect to the phage long axis, as measured by static solid state NMR [144], which would

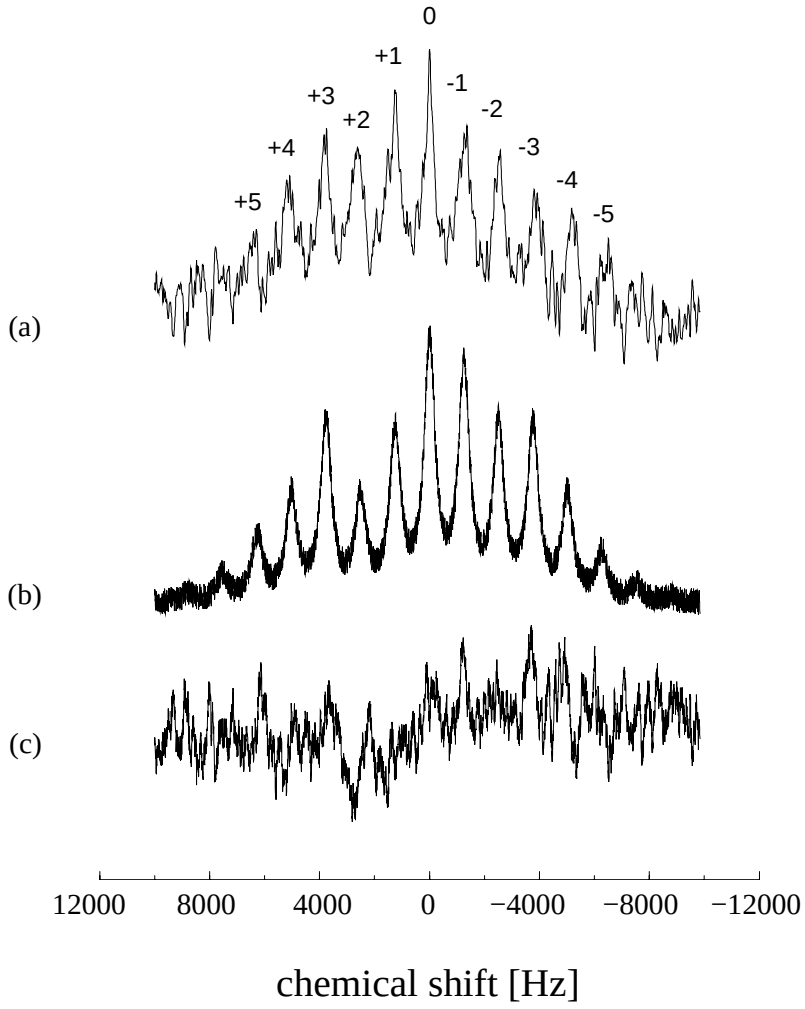

Figure 5.12: Experimental ^{13}C-MAOSS spectrum (a) and best fit simulation with added noise (b) for ^{13}C=O[Val-29] in M13. The difference is plotted in (c). The large natural abundance contribution of ca. 30-40% to the spectrum and the signal to noise yield a result with an error of β_{MR}=20° ± 10° the Val-29 peptide plane.

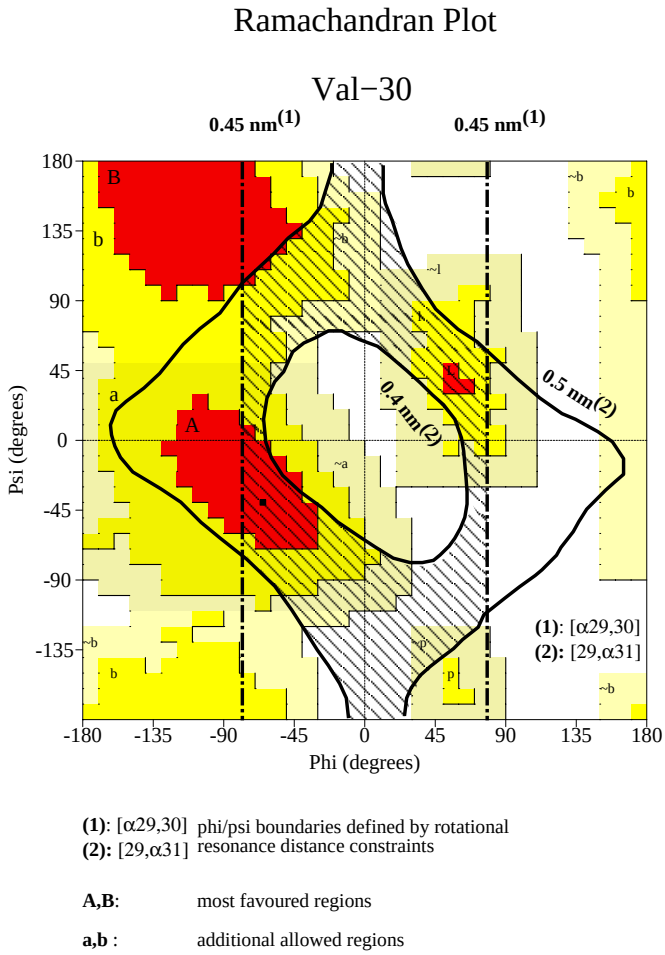

Figure 5.13: Val-30 [Φ-Ψ]-map: the shaded region agrees with the NMR distance constraints [α29,30]=0.4±0.05nm and [29,α31]=0.45±0.05nm. Although the experimental error is relatively large, and so the area of possible angle combinations not well defined, a clear distinction between ideal conformations can be made.

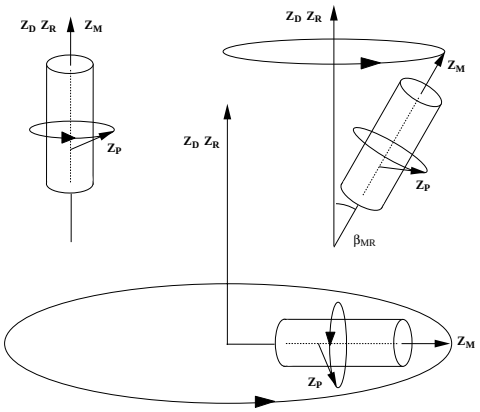

Figure 5.14: Throughout this study transverse isotropy has been assumed, i.e. membrane components are distributed about the bilayer normal Z_D and the PAS is distributed about the molecular axis Z_M. For this situation, the spectrum from a labelled site in a helix approaches a powder spectrum the more the helix is tilted. There might be however situations, in which this is not true any more, e.g. if a helix which is perpendicular to Z_D, has a preferred orientation with respect to the membrane surface, e.g. due to charged residues. In this case, additional experimental information are necessary for the NMR data analysis.

support the model suggested by Marvin [140].

The aim of this study was to show, that MAS NMR spectroscopy on unoriented and oriented samples can provide valuable information about local conformational and orientational details of selectively labelled membrane proteins. The applicability of the MAOSS approach for measuring the orientation of α-helical peptides has been demonstrated by using the chemical shift anisotropy of carbonyl. However, one important point has to be made about the general assumptions made above. Throughout this study, transverse isotropy has been assumed, i.e. membrane components are distributed about the bilayer normal Z_D and additionally, the PAS is distributed about the molecular axis Z_M. A theoretical formalism has been discussed in Chapter 3 and an application to ^{2}H-MAOSS on bacteriorhodopsin was demonstrated in Chapter 4 (see Fig.3.1). For this situation, the spectrum from a labelled site in a helix approaches a powder spectrum the more the helix is tilted, because the signal is integrated about Z_M and about $Z_D(Z_R)$ as illustrated in Fig.5.14. There might be situations however, in which the assumption of orientations with equal probability about Z_M is not true any more, for example if a helix which is perpendicular to Z_D, has a

preferred orientation with respect to the membrane surface due to interaction between charged lipids and charged residues. In this case, additional information is necessary for the NMR data analysis. For example, it would be essential to know, if the peptide crosses the membrane or remains on the surface. A helix which would have a preferred orientation on the membrane surface features uni-axiality, while the same system parallel to the membrane normal would be treated as a transverse isotropic distribution as shown in Fig.3.1 and Fig.5.14. Fortunately, these problems would only occur for short peptides and membrane protein fragments, because the whole molecule fixed coordinate system MF might be tilted, while for large membrane proteins, all steps such as those discussed here and for bacteriorhodopsin in Chapter 4 would apply.

5.5 Conclusion

It has been shown by a uniform MAS high-resolution solid state NMR approach, that the transmembrane domain of M13 coat protein is α-helical and slightly tilted with respect to the membrane normal, which agrees with published data and extends the accepted model.

MAOSS spectroscopy has been shown to be applicable to membrane-bound proteins using carbonyls as an example for spin-1/2 nucleus. Future development will concentrate on multi-dimensional applications to multiple ^{15}N labelled systems and MAS recoupling experiments and will be extended to oriented systems for measuring the orientation of the dipole coupling vector.

Chapter 6

Probing Membrane Surfaces and the Location of Membrane Components by ^{13}C MAS NMR using Lanthanide Ions

Abstract

The interaction of the Lanthanide ion Dy^{3+} with dimyristoylphosphatidylcholine (DMPC) bilayers and selectively ^{13}C-labelled M13 coat protein is observed by ^{13}C-CP MAS. It is shown that this approach forms a simple and efficient way to probe the membrane interface and to estimate the location of membrane components within the bilayer.

6.1 Introduction

It has been shown in the previous chapters that structural parameters, such as distances, dihedral angles and tensor orientations can be obtained by MAS spectroscopy, which is essential for the structural understanding and model building of membrane proteins. Besides these essential geometrical information, the polar interfacial region of membranes, where many important interactions between membraneous components and extracellular/cytoplasmic substances occur, is of particular interest. Pure phospholipids, lipids with sterols, and membranes with peptides/proteins have been studied extensively, often by exploiting the binding of various cations to the membrane surface and then monitoring the occurring structural or phase changes [180],[181],[182],[183],[184].

In the following, the problem of determining whether a particular site in a membrane protein, is buried in the hydrophobic core, close the the interface or outside the membrane, is addressed. Despite a number of structural studies on

membrane bound peptides and other membrane effectors, there is still often some controversy about where precisely these molecules are located in the membrane, which is however an important issue in understanding the molecular mechanism of action for these systems.

Here, it is demonstrated, that it is possible to estimate the location of membrane embedded components with respect to the interface, using a combination of high resolution ^{13}C CP MAS NMR and binding of paramagnetic shift reagents (in our case Dy^{3+}) to the membrane surface.

In the past, it has been shown that ^{31}P MAS NMR can be used to screen specific interactions between peripheral/integral proteins with various phospholipids in a membrane. The potential of this method which uses the ^{31}P nucleus found in the lipid head groups and so in the membrane interface, as an intrinsic non-perturbing reporter, has been demonstrated by studying interactions between lipids and *cytochrome c*. The protein was bound to mixed cardiolipin/PC/PE vesicles and specific protein-phospholipid interactions could be described in a quantitative way [185]. The same approach has been used to study the effect of cardiotoxin II on the segregation of PG out of PG/PC mixtures [186].

However, ^{31}P MAS can only provide local information about the phospholipid headgroup properties, while ^{13}C CP MAS NMR would allow information to be gained simultaneously for the various chemical groups in lipids or peptides/proteins. For pure lipid systems it was first shown by Oldfield and coworkers that a spectral resolution could be achieved which allows an assignment of all carbon atom positions in a lipid molecule [61], while Opella et.al demonstrated the possibility to resolved ^{13}C resonances for solid proteins by MAS [187]. The successful spectral separation of the various chemical groups was made possible due to the large spread of chemical shift values for ^{13}C nuclei in various environments covering a range of nearly 200 ppm compared with 10 ppm for ^{1}H . Thus the influence of membrane effectors, such as cholesterol, on the lipid headgroup, backbone and fatty acid chain simultaneously at atomic resolution, thereby avoiding expensive labelling (as for ^{2}H NMR) since the ^{13}C natural abundance in these systems in particular in combination with CP techniques, could be exploited [61].

The potentially good resolution of ^{13}C CP MAS NMR and known resonance assignments enables the site-resolved observation of the effect of Dy^{3+} ions, which bind tightly to the polar phosphatidylcholine headgroups. The binding of these Lanthanide ions allows a spectrally resolved broadening or shift of resonances arising from chemical groups of the various molecules which are in close proximity to the polar interface or outside the membrane [188]. The basic idea is illustrated in Fig.6.1.

The validity of the approach presented here was evaluated by NMR experiments on pure liquid crystalline DMPC membranes upon titration of various amounts of Dy^{3+} ions. The effect of the lanthanide ions on the resonances arising from the various carbon atoms of the lipid headgroup and the glycerol backbone could be observed and the binding constant of Dy^{3+} on PC membrane surfaces

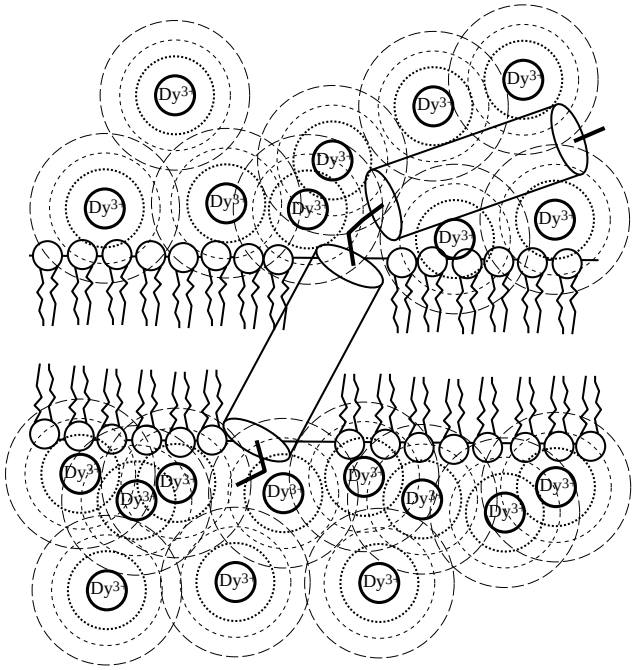

Figure 6.1: The effect of binding paramagnetic ions to the membrane surface: chemical shift and relaxation effects are scaled with r^{-6}, the distance between the paramagnetic ions and the observed NMR nuclei, which allows an estimate of the location of specific sites with respect to the membrane interface to be made.

was determined by analysing the decay of intensities for the various resonances.

Finally the applicability of this method to membrane-bound peptides is demonstrated on the 50 residue long M13 coat protein which was specifically ^{13}C=O labelled at Val-29 and ^{13}Cα labelled at Val-31. It is shown that these residues are, as suggested from other studies, deeply buried inside the membrane bilayer and therefore not effected by the binding of lanthanides to the membrane surface.

Theory. The unpaired electrons of paramagnetic ions produce a magnetic field which strongly influences other nuclei located in their vicinity. The local field can considerably exceed the effects of the external magnetic field B_0 and may so change the resonance of neighbouring nuclei dramatically.

The interaction of paramagnetic ions with adjacent nuclei can take place in two ways. Fermi contact interaction, i.e. direct transmission of electron spin density through the bonds and "through-space" dipolar (pseudo-contact) interaction due to the field effects of the paramagnetic ions [189]. The Fermi contact is only of importance for nuclei which are directly adjacent to the paramagnetic, trivalent cations. Lanthanides associate in lipids with the anionic phosphate group which creates a large contact contribution to the phosphorus signal, while in contrast protons and ^{13}C experience large dipolar, pseudo-contact interaction [190].

Paramagnetic ions can be divided into two groups, those with long electron relaxation times would cause extensive linebroadening, while others with short electron relaxation times do not alter the T_2 relaxation time of the perturbed nuclei, but change their chemical shielding and so move their chemical shift upfield or downfield.

In practice, paramagnetic ions act both as shift as well as relaxation reagents. Which is most easily observed depends on the experimental conditions [191].

For Lanthanides, the origin of the paramagnetic shift in high-resolution NMR is mainly dipolar, and is given for a uniaxially symmetrical ligand field:

$$\frac{\Delta\omega}{\omega} = D_1\left(\frac{3\cos^2\beta - 1}{r^3}\right) + D_2\left(\frac{3\sin^2\theta\cos 2\alpha}{r^3}\right) \tag{6.1}$$

where D_1 and D_2 are temperature dependent constants which depend on individual Lanthanide ions, $\mathbf{r}$ is the vector between ion and nuclear spin, α,β relate vector $\mathbf{r}$ to the PAS of the magnetic susceptibility tensor and $\Delta\omega/\omega$ is the ratio of chemical shift change to the chemical shift.

The dipolar contribution of the electron spin, S, to the nuclear relaxation rates of nucleus I is expressed as [191]:

$$\frac{1}{T_{1M}} = \frac{2}{15}\frac{\gamma_I^2\mu_S^2}{r_{IS}^6}\left(\frac{3\tau_C}{1+\omega_I^2\tau_C^2} + \frac{7\tau_C}{1+\omega_S^2\tau_C^2}\right) \tag{6.2}$$

and

$$\frac{1}{T_{2M}} = \frac{1}{15}\frac{\gamma_I^2\mu_S^2}{r_{IS}^6}\left(4\tau_C + \frac{3\tau_C}{1+\omega_I^2\tau_C^2} + \frac{13\tau_C}{1+\omega_S^2\tau_C^2}\right) \tag{6.3}$$

where γ_I is the magnetogyric ratio, μ_S the magnetic moment $\mu_S = g_S\sqrt{S(S+1)}$ given in units of the Bohr Magneton $\beta = 9.2741 \times 10^{-24} JT^{-1}$, r_{IS} is the vector between the paramagnetic ion and the observed nucleus and, ω_I and ω_S are the electronic and nuclear Larmor frequencies (with $\omega_S \gg \omega_I$). The correlation time τ_C is given by

$$\frac{1}{\tau_C} = \frac{1}{\tau_R} + \frac{1}{T_{1e}} + \frac{1}{\tau_M} \tag{6.4}$$

where τ_R is the overall rotational correlation time of the observed complex, T_{1e} is the electronic spin relaxation time and τ_M is the life time of the complex. For Lanthanide ions, which have relatively short electron spin relaxation times of 0.1-0.4 psec [192], relaxation terms which have to be added to the expressions above have been derived by Vega and Fiat [193]:

$$\frac{1}{T_{1M}^{\varkappa}} = \frac{6}{5}\frac{\gamma_I^2 B_0^2 \mu_S^4}{(3kT)^2 r_{IS}^6}\left(\frac{\tau_R}{1+\omega_I^2\tau_R^2}\right) \tag{6.5}$$

$$\frac{1}{T_{2M}^{\varkappa}} = \frac{1}{5}\frac{\gamma_I^2 B_0^2 \mu_S^4}{(3kT)^2 r_{IS}^6}\left(4\tau_R + \frac{\tau_R}{1+\omega_I^2\tau_R^2}\right) \tag{6.6}$$

It can be seen that the T_2 contribution to the linewidth increases with the field strength B_0^2 and with μ_S^4. The magnetic moment of a typical downfield shift reagent like Yb^{3+} is $4.5\times\beta$, while Dy^{3+} and Ho^{3+} have the largest moments of $10.5\times\beta$ and $10.4\times\beta$ [194],[195], which means they would contribute more to the nuclear relaxation, compared to other Lanthanide ions. All equations for relaxation times above assumed that paramagnetic ions undergo isotropic rotation, which is not the case in lipid membrane systems. Angle dependent terms would need to be included [191], but here, qualitative discussions can be based on the assumptions made before and the r^{-6} distance dependence of the relaxation rates can be used to estimate locations of specific sites with respect to the membrane surface, which has been illustrated already for some sterols in phospholipids by ^{13}C-T_1 measurements [183],[184].

6.2 Materials and Methods

Materials and Preparation. L-α-DMPC was obtained from Sigma (UK), and used without further purification. $DyCl_3 \cdot 6H_2O$ (Aldrich, UK) was prepared as a 25 mM stock solution in doubly distilled water at pH 4. M13 coat protein (^{13}C=O labelled at Val-29, $^{13}C_\alpha$ labelled at Val-3, Asp-5 replaced by Asn) was synthesized using standard solid-phase FMOC chemistry (NSR Centre, Nijmegen, The Netherlands). The quality of the obtained protein was checked by HPLC and mass spectrometry and found to be over 90% pure.

Pure DMPC dispersions were prepared by adding 60 wt% of double distilled water to 20 mg of dried lipid. DMPC dispersions containing various amounts of Dy^{3+} cations were prepared as before using appropriate aliquots of the 25 mM $DyCl_3$ stock solution. Complete homogenization for all samples was achieved by three cycles of freezing with liquid N_2 and thawing at 37^{o}C. Afterwards membrane vesicles were pelleted into 4 mm MAS NMR rotors (Bruker, Karlsruhe, Germany), sealed and immediately measured.

M13 coat protein was incorporated into DMPC bilayers at a lipid to protein molar ratio of 30:1 as described in Chapter 5. The lipid/protein molar ratio was determined by using appropriate phosphate and protein assays. Correct incorporation of the protein in an α-helical form was checked by CD-measurements. Finally the sample was resuspended either in water or appropriate Dy^{3+}solution and pelleted into 7 mm MAS NMR rotors.

NMR measurements. ^{13}C CP MAS NMR experiments under efficient proton decoupling (40 kHz) were carried out at 100.63 MHz carbon frequency on an MSL-400 (Bruker, Germany) and at 50.32 MHz carbon frequency on a 200 MHz Infinity (Chemagnetics, USA) using double resonance 7- and 4-mm MAS NMR probes (Bruker, Germany). The NMR spectra were acquired with a $\pi/2$ carbon pulse length of 4μs, a recycle time of 3s and a CP mixing time of 2.5 ms. All NMR measurements at 400 MHz proton frequency were recorded at 5 kHz spinning speed using a RAMP-CP pulse sequence [97][159] . For experiments at 200 MHz and 1.9 kHz spinning speed a conventional CP pulse sequence was applied. All experiments were carried out at 308 K$\pm$1 K regulated by an BVT3X00 temperature control unit (Bruker, Germany). The spinning speed for the MAS NMR rotors was regulated by a pneumatic MAS control unit (Bruker, Karlsruhe). The number of acquisitions varied between 500 and 100 000 scans.

6.3 Results and Discussion

Pure DMPC membranes.

A complete assignment of the ^{13}C NMR MAS spectra of DMPC is necessary for the study of interactions between lipids and Lanthanide ions and is shown in Fig.6.2. The resonances were assigned according to literature values [97]. Especially resonances from the lipid headgroups and immobilized glycerol backbone are of importance, since they are close to the membrane interface and so most likely being effected by paramagnetic ions. The resolution required was achieved by ^{13}C CP MAS NMR experiments at 100.63 Mhz carbon frequency on multilamellar DMPC vesicles in their liquid crystalline phase at 308 K. The high spinning speed of 5 kHz required a RAMP CP pulse sequence, which provides

sufficient cross polarization for the various carbons in such a complex and dynamic system [159].

The NMR spectrum in Fig.6.2 shows all ^{13}C resonances for DMPC with their chemical shift values covering nearly 200 ppm resolved. Performing the same experiment at a lower spinning speed (spectrum not shown) revealed no spinning sideband resonances in the L_α phase of DMPC and therefore all resonance lines in Fig.6.2 reflect the isotropic chemical shift values of the various carbons in the lipid molecule in agreement with earlier observations [61],[97].

In contrast to gel phase of phosphatidylcholine bilayers, very fast intra- and intermolecular motions [69],[97] of lipid molecules occur in the liquid crystalline phase, thereby reducing the chemical shift anisotropies for the various carbons and finally leading to the disappearance of spinning sidebands even at moderate spinning speeds. The very narrow linewidths are observed due to lower spin-spin relaxation rates caused by the altered dynamic behaviour of the lipid molecules in the liquid crystalline phase [70],[97] (see also Chapter 2).

The chemical shift range of ^{13}C resonances in lipids can be divided roughly into four main spectral groups: aliphatic fatty acid chains, polar headgroup, glycerol backbone and carbonyl groups. Based on previously reported spectra [97],[61] a complete, unambiguous assignment of all the resonances in the obtained spectrum was possible, even including the signals for the *sn*-2 and *sn*-1 carbonyl groups (173.3 ppm and 173.1 ppm) and both chain-C3 carbons (25.3 ppm for *sn*-2 carbon, 25.1 ppm for sn-1).

The resonances arising from the headgroups and backbone which both occur in the same region of the spectrum (50-70 ppm) are as indicated in Fig.6.2.

Addition of $Dy^{3+}$to DMPC membranes.

After adding of Dy^{3+} ions in various concentrations in the range of 1 - 25 mM to DMPC bilayers, ^{13}C CP MAS NMR experiments were carried out under the same conditions as used before for pure lipid bilayers. The enlarged spectral region for headgroup and glycerol resonances is displayed as an inset in Fig.6.2a-f for concentrations of 0,1, 2, 5, 10 and 25 mM. The addition of Lanthanide ions leads gradually to loss of intensity for various resonances which finally results in a complete disappearance of all resonances at a concentration, of 25 mM as shown in Fig.6.2f.

A concentration as low as 1mM of Dy^{3+} ions has already a small, but clear linebroadening effect on all headgroup and backbone resonances, while glycerol-$\underline{C_3}$ and choline C_α are effected most (Fig.6.2b). At 2mM Dy^{3+} the $\underline{C_3}$ and C_α resonance lines are nearly quenched and all other resonances show a further, more drastic reduction of their intensities in the NMR spectrum. This effect is amplified upon further addition of Lanthanide ions up to 5mM, but all resonances can still be detected, while at a concentration of 25 mM all signals from backbone and headgroup carbons have disappeared. At this high concentration, a decrease of

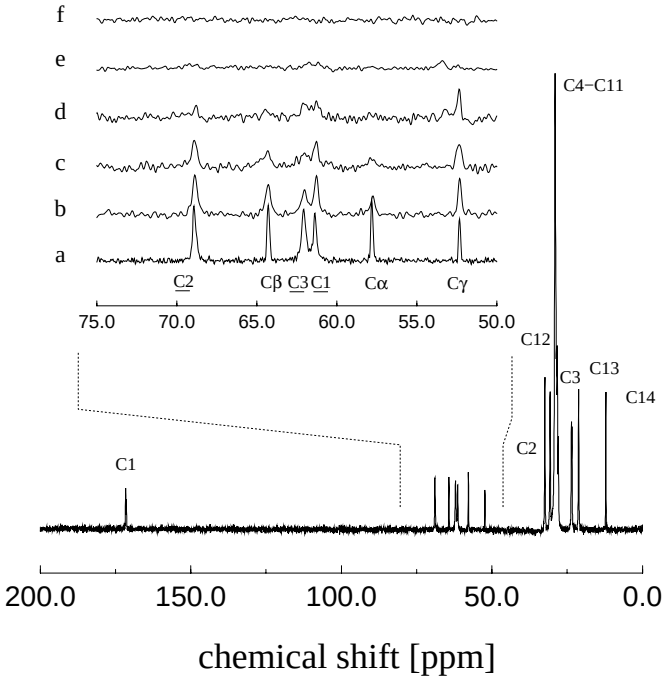

Figure 6.2: Proton (400.13 MHz) decoupled ^{13}C CP MAS spectrum of multilamellar DMPC membranes at 308 K, 5000 Hz spinning speed and 2.5 ms CP mixing time. Inset: expanded spectra of the headgroup and glycerol ^{13}C resonance region without and with various concentrations of $DyCl_3$ solution: a) 0 mM, b) 1 mM, c) 2 mM, d) 5 mM, e) 10 mM, f) 25 mM. Same Acquisition parameter for a) - f).

the intensity of fatty acid chain methylene resonances was observed as well, which was has not been seen at lower concentrations and is probably caused by a larger paramagnetic contribution of Dy^{3+} to the spin-spin and spin-lattice relaxation of the methylene carbons.

Summarising, it can be stated that adding of Dy^{3+} leads to loss of intensity and broadening of resonance lines for carbons at the lipid interface, but no significant shift effects are observed for the Dy^{3+}concentrations used here. Paramagnetic relaxation effects, i.e. T_{2M} contribution to T_2 and so to linewidth are probably larger than chemical shift contribution under our experimental conditions. A similar effect at moderate levels of Dy^{3+} in solution has been reported before by Hauser et al. [182] who found that only phosphorous and proton resonance showed clear shift effects, while the ^{13}C resonances were only slightly or not shifted. Due to the larger linewidth in solid state MAS NMR spectra compared to liquid-state NMR the shift changes were probably not large enough to be discernible.

The integral intensity for each carbon signal normalised to the total fatty acid chain-C_4-C_{11}-CH_2 resonance, is plotted versus the concentration in Fig.6.3. All intensities were normalized to 1.0 when no Dy^{3+} ions were present.

The most dramatic loss of up to 60% in intensity upon addition of 1mM Dy^{3+} occurs for the glycerol-$\underline{C_3}$ and the choline C_α atoms while glycerol-$\underline{C_2}$ and C_β positions are only effected to about 15%. However at 2mM, the intensity decay for all resonances is already more pronounced for all lines. The $\underline{C_1}$ carbon is now effected by a 30 % loss in intensity while the $\underline{C_3}$ and C_α resonances are already reduced to 15% of their original intensities. Adding higher amounts of ions leads to a continued gradually deterioration of signal intensity for all resonances and finally to a complete loss of signals in the 50-75 ppm region of the spectrum at 25 mM Dy^{3+} (see inset of Fig.6.3).

Comparing the response of ^{13}C signals from headgroup and backbone carbons of DMPC upon Dy^{3+}titration enables us to define the binding site for the metal ion. Therefore, as shown in Fig.6.2 and 6.3, the intensity for the C_α line is reduced drastically after adding only 1 mM trivalent ion, followed by an slightly smaller reduction for C_3. Compared to these drastic losses in intensity the decay of the C_β and $\underline{C}2$ carbon signals were less pronounced, an indication that these positions have a more remote distance to the lanthanide binding site (r^{-6} distance dependency). These findings indicate, that Dy^{3+} binds to the PO^- group, since the adjacent carbon atoms $\underline{C}3$ and C_α, are effected most.

This observation agrees well with earlier ^{13}C MAS NMR studies by Villian et. al. [183],[184] who showed by measuring spin-lattice relaxation rates before and upon adding of the spin relaxation agent Gd^{3+}, that mainly $\underline{C}3$ and C_α carbons were effected. Solution proton NMR studies on small vesicles upon adding of various lanthanide ions also indicated that the nearest protons to this trivalent ion were attached to the $\underline{C}3$ and C_α[180][182].

The correct interpretation of the ^{13}C data is underlined by the fact, the most

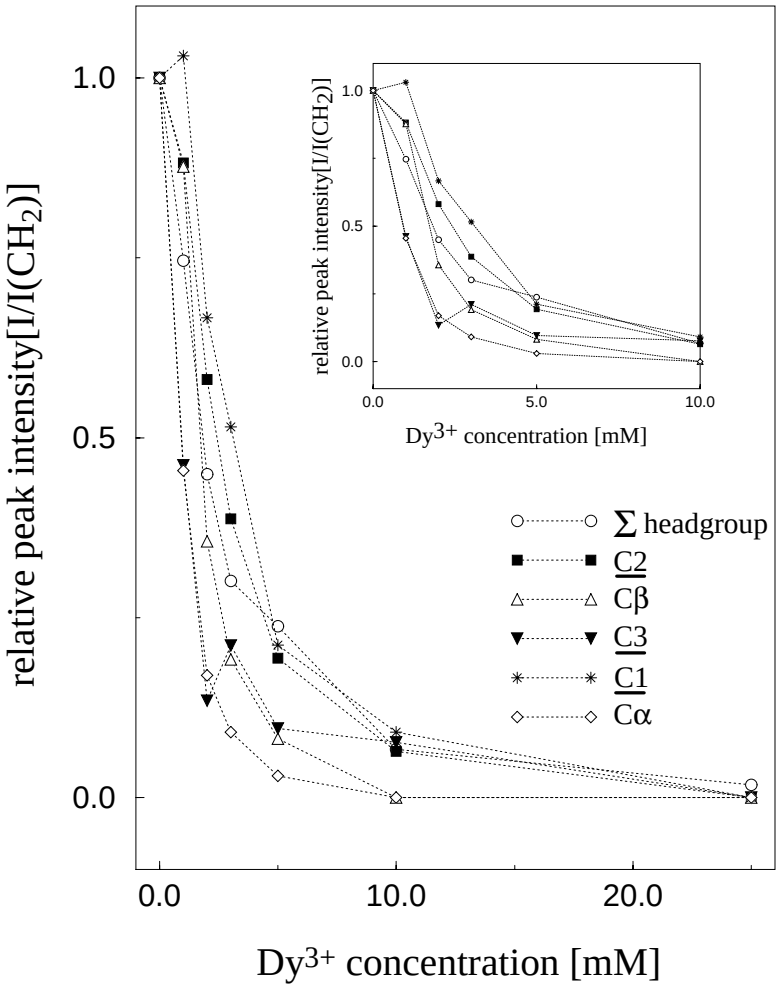

Figure 6.3: Effect of Dy^{3+} added at various concentrations on the relative intensities of the headgroup and backbone ^{13}C NMR resonances of DMPC bilayers at 308 K (spectrum shown in Fig.1). Intensities expressed as fraction of the uneffected lipid fatty acid chain CH_2 groups and scaled up to 100% for the undisturbed system for each resonance. Various symbols indicate the specific resonances. Open circle: Sum of headgroup and backbone intensities. Inset diagram: Expansion of diagram for 0 mM - 10 mM Dy^{3+} concentration.

dramatic effects of Dy^{3+} were observed for the PO^-group using ^{31}P NMR. As mentioned before, it has been concluded from chemical shift data, that lanthanide ions when added to the phospholipid membrane surfaces, bind through direct attachment to the PO^-group [182]. This closed proximity of trivalent ion to the phosphorous is also reflected in ^{31}P MAS NMR spectra obtained by us for the DMPC vesicles, where extremely broadened lineshapes (not shown) were detected.

Based on our own observations alone we can already conclude that the most likely binding site for Dy^{3+} must be the negatively charged PO^-group in the lipid molecule since DMPC is zwitterionic over the pH range 3-13.

The presented solid state ^{13}C MAS NMR experiments illustrate that the interaction of paramagnetic Lanthanide ions with lipid headgroups and so with the membrane surface, can be detected at a molecular level by observing the intensity losses in the NMR resonances for each carbon atom located at the membrane/water interface.

Nuclei in different chemical groups located near the membrane interface should experience similar effects, i.e. decrease of intensity of their NMR resonances, depending on the ion concentration and their distance from the ion binding site. Groups deeply buried inside the membrane should be protected from the influence of the bound paramagnetic ions. Since visible changes were observed in spectra of pure DMPC liposomos down to the fatty acid $\underline{C_3}$ groups, it is expected that it is possible to differentiate between ^{13}C labelled residues of a peptide/protein located above or below these $\underline{C_3}$ carbon positions.

Interaction with M13 coat protein/DMPC vesicles.

By using the 50 residue long M13 coat protein incorporated into DMPC bilayers at a molar lipid to protein ratio of 30:1, the possibility of determining the location of two specifically ^{13}C labelled protein residues in the membrane was tested. It was of particular interest to find if the method could be used to differentiate between a location of these residues at the membrane interface or in the hydrophobic region. The protein was ^{13}C=O labelled at Val-29 and $^{13}C\alpha$ labelled at Val-31 in its hydrophobic domain (see Fig.5.2).

^{13}C CP MAS NMR experiments were performed on multilamellar DMPC/M13 liposomes, both before and after addition of 10 mM aqueous Dy^{3+} solution at 308 K and 1.9 kHz spinning speed. The spectrum of the untreated system is displayed in Fig.6.4, on same chemical shift range as the pure DMPC spectrum in Fig.6.2. As expected, the spectrum is nearly identical to the one for DMPC bilayers except for two additional broad peaks at 170 ppm and 56 ppm arising from the labelled protein residues.

Compared to the lipid resonances shown in Fig.6.2, the NMR resonances

obtained here, again show no significant changes in their chemical shift values, but have slightly larger linewidths and the resolution, mainly in the chemical shift region of the aliphatic carbons, is reduced. These effects are most likely caused by a changes in the dynamic and ordering profile of the lipid molecules due to the interactions with the incorporated protein, as shown in by ESR and ^{2}H-NMR [196].

Spectrum (a) in Fig.6.4 shows an extended spectral regions where the ^{13}C resonances of both Val residues in the protein appear. As seen in the left spectrum, two peaks appear in the carbonyl region. The narrow sharp resonance line occurs at 171.8 ppm and can be assigned to the *sn*-1 and *sn*-2 carbonyl groups of the highly mobile DMPC lipid molecules. However both carbonyl groups cannot be resolved separately as in the case of the pure DMPC system. The second, broad peak at 170 ppm can be assigned to ^{13}C at the carbonyl position of the Val-29 residue. The spectrum on the right in Fig. 6.4a displays the expanded 35 - 85 ppm chemical shift region. Here all the expected resonances for the lipid backbone and headgroup carbons can clearly be detected and assigned. Additionally a new broad resonance, similar to the one at 171 ppm, appears at 56 ppm which belongs to the $^{13}C\alpha$ carbon in the Val-31 residue. Both resonances show some inhomogeneous linebroadening, which may indicate a certain conformational distribution or peptide wobbling in the bilayer.

^{13}C CP MAS NMR spectra were acquired upon addition of 10 mM Dy^{3+}solution to the M13/DMPC vesicles under the same experimental conditions as described before. The expanded areas of the spectrum containing the protein resonances are displayed in Fig.6.4b. As in Fig. 6.4a, the diagram on the left shows the region where carbonyl signals are expected and the one on the right the region where lipid headgroup and backbone resonances and $^{13}C\alpha$ signals of proteins appear.

It can be seen that all ^{13}C signals arising from the lipid carbons vanished completely in this spectral region, which is not a surprising result when compared with the spectrum of pure DMPC bilayers at 10 mM Dy^{3+} concentration in Fig.6.2e. However both protein resonances are still fully visible and seem to be unaffected by the presence of the trivalent Lanthanide ions.

A quantitative comparison was performed by substruction of the spectrum of M13/DMPC containing 10mM Dy^{3+} (Fig.6.4b) from the spectrum of the untreated system (Fig.6.4a) which is displayed in Fig.6.4c. Here only lipid resonances can be seen while the protein peaks are not present which shows clearly that neither a change in the linewidths nor a drop in absolute intensity for these protein resonances occur upon addition of 10 mM Dy^{3+} solution. Therefore it can also be assumed that the cross polarisation efficiency for both carbons at the two residues is not effected by the presence of trivalent cations at the membrane surface.

To explain this unchanged behaviour of the protein resonances in the NMR spectra, both Val-29 and Val-31 have to be located at a position which is too far away for dipolar interactions with the paramagnetic ions, i.e. a location at

the membrane interface or in the aqueous phase can be ruled out, but a position in the hydrophobic core of the lipid bilayers is most likely. The conclusion that both residues are located in the apolar region of the membrane is not a surprise since it has been shown before that both residues are part of the transmembraneous membrane spanning region of the protein [81],[140]. It is known from earlier studies [147],[140],[145],[146] and the results in Chapter 5, that the transmembrane domain has an α-helical structure in the reconstituted DMPC/M13 bilayer, which mimics the *in vivo* state in the *E.coli* plasma membrane.

Since the $\underline{C_3}$ resonances of the fatty acid chains of the DMPC lipids are still effected by the binding of Dy^{3+} as shown in the intensity plot in Fig.6.3 and in the spectra in Fig.6.2e and 6.4b, it is suggested that the labelled sites in Val-29 and Val-31 are situated below this position in the membrane. However, the data does not allow any conclusion to be drawn about their precise location in the hydrophobic core region.

A more precise positional refinement would be possible in principle by our approach by using various differently labelled proteins to obtain the residues in the sequence located at both sides of the membrane leaflet interface. A recent study for determining precisely the location of these residues limiting the transmembrane spanning part was carried out by Hemminga et. al. [197]. They performed EPR studies on spin-labelled M13 major coat protein mutants where various single cysteine replacements in the transmembrane part were introduced, for which individual locations could be estimated by using Ni^{2+} and O_2 as paramagnetic relaxation agents. They concluded that the transmembrane helix is spanning the membrane in a way where Ala-25 and Thr-46 are located at the membrane interface of opposite monolayer leaflets while Thr-36 is at the centre of the membrane. According to this model the Val-29 residue would be located one pitch height below Ala-25 while Val-31 would be closer to the hydrophobic centre; a finding which agrees very well with our observations. Alternatively, solution NMR relaxation measurements of the protein backbone on detergent solubilized peptides would allow to identify motionally restricted residues in the transmembrane domain and more dynamic sites outside the hydrophobic core. M13 coat protein in a micelle system has been studied extensively and it was found, that the hydrophobic helical part of the protein, including both Val-29 and Val-31 residues, is motionally restricted while the amphipathic part experienced much more unrestricted dynamics [77],[85],[150],[82].

Both these approaches, detergent supported solution NMR and spin-label EPR, use modified systems. In EPR, bulky spin reporters and mutated proteins are necessary, both of which could introduce a possible cause of altered secondary structure and residue location. In the NMR study, the protein is not modified but solubilized in detergent micelles which only resemble partially membrane bilayers.

A transmembrane spanning helix could therefore also experience secondary structure modification and a correct determination of the residues located at the membrane interface is not possible due to the missing interaction of the

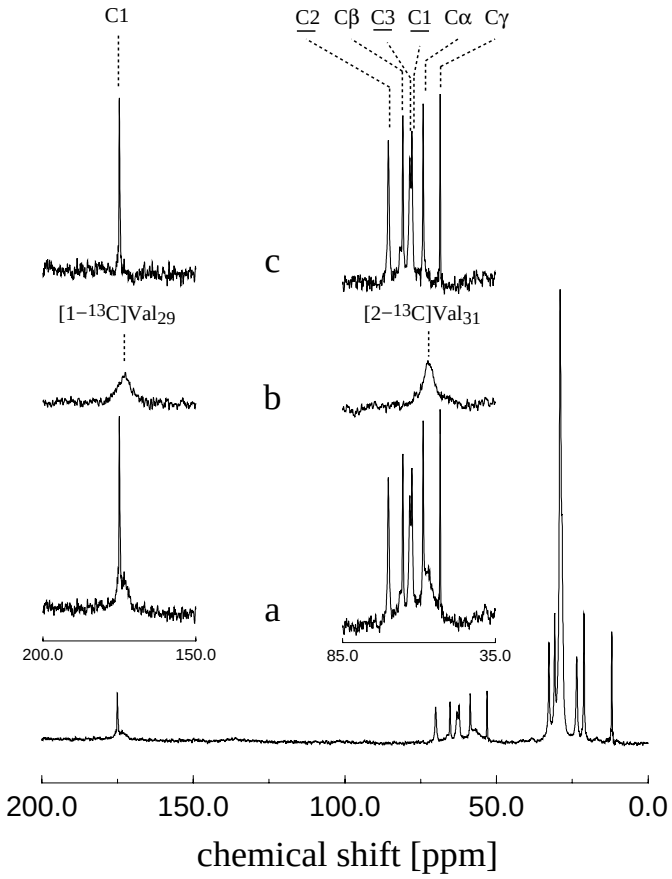

Figure 6.4: Proton (200.13 MHz) decoupled ^{13}C CP MAS spectra of multilamellar DMPC membranes containing M13 coat protein at lipid to protein ratio of 30:1 before and upon adding of 10 mM $DyCl_3$ solution. Full spectrum of untreated M13/DMPC complex and extended regions of from carbonyl peaks (left) and headgroup, glycerol lipid peaks and C_α protein peaks (right) (a); same extended regions as in (a) but after adding of 10 mM Dy^{3+}(b); Spectra obtained for the same regions after subtraction of spectra of treated complexes from untreated (c). Experimental conditions: 308 K, 1900 Hz spinning speed, 2.5 ms CP mixing time and 100 000 Scans each.

transmembrane part with both leaflet interfaces of a lipid bilayer.

The approach presented here, avoids these disadvantages.

6.4 Conclusions

It has been shown by ^{13}C-CP MAS, that the Lanthanide ion Dy^{3+} can be used as a paramagnetic relaxation agent to probe the membrane interface as deep as to the backbone position C3. The observed linebroadening or quenching of ^{13}C resonance lines allows an estimate of the location of membrane components with respect to the membrane surface to be made. The advantage of ^{13}C-CP MAS over other techniques is mainly in its resolution, sensitivity and the fact, that it does not perturb the system.

Chapter 7

Future Perspective

It has been shown, that NMR experiments based on the suggested MAOSS approach can provide valuable structural information on membrane proteins and peptides. Applications to bacteriorhodopsin, bovine rhodopsin and phospholamban are already in progress in our laboratory but are not reported here.

To make full use of the potential of this technique, some further methodological development is necessary and will be addressed in the future. The most important issues are outlined below.

7.1 ^{1}H-MAOSS and Protein Dynamics

The highly resolved proton spectra of lipids obtained by ^{1}H-MAOSS give rise to the question, how this effect could be exploited for highly mobile peptides or proteins. A feasibility study on gramicidin A, which has a long axis correlation time of 10^{-6} sec [117], did show some promising improvements in the resolution of the aromatic protons. However, sample preparation has still to be optimized towards the best compromise between orientation, hydration, fluidity and stability. Due to a lack of time, this study was not pursued, but will be continued later.

Although ^{1}H resolution improvement by utilizing anisotropic motions might be limited to small membrane components, there are some theoretically interesting effects which could be studied. In a simplified model, a small membrane component, such a α-helical peptide, would rotate fast about the membrane normal and so about the magic angle. This fast correlation time would allow cross-relaxation within the membrane plane, but not along the helix long axis, since the dipolar coupling would vanish along the magic angle (see [198]). In this situation, anisotropic effects should be observed in NOESY experiments, which might be used to extract some structural information.

7.2 Anisotropic Interactions

The full potential of the MAOSS approach as illustrated for ^{2}H and ^{13}C on bR and M13 coat protein, can only be used, if experiments on multiple labelled proteins can be performed and analysed which will require multidimensional NMR in order to provide the necessary resolution.

Preliminary experiments on ^{15}N-Met labelled bR, which were carried out in our laboratory, did allow to resolve five out of nine residues in a simple one-dimensional MAS experiment. The central problem is separating all sideband families in order to calculate the main elements from MAS NMR and the orientation of the CSA tensor from MAOSS NMR for each labelled site. The basic idea of such an experiment is shown in Fig.7.1. The simulation corresponds to a ^{15}N resolution as observed for bR, while some tensor orientations were assumed from a structural bR model. Separating the sidebands in a second dimension can either be achieved by using the dipolar ^{1}H-^{15}N coupling, or the ^{1}H or ^{15} N chemical shift anisotropy [21]. An alternative would be a modified PASS experiment [21].

7.3 Anisotropic MAS Recoupling Experiments

Recoupling experiments such as rotational resonance, allow distance measurements within membrane proteins, as illustrated in Chapter 5. Performing these experiments in a MAOSS arrangement, i.e. on oriented systems, an additional structural constraint, namely the direction of the internuclear vector between the coupled spins I and S can be obtained (see Fig.5.5). If this vector would be parallel to the membrane normal Z_D, no magnetisation exchange would be observed, since the dipolar coupling would collapse at the magic angle. However, the more the internuclear vector is tilted with respect to the membrane normal Z_D and so to the rotor axis Z_R, the larger would be the Zeeman magnetisation exchange rate. The advantage of this approach is, that the internuclear vector is directly related to the molecular structure, while for studying chemical shift anisotropies, some knowledge about the orientation of the tensor in the molecular frame is necessary.

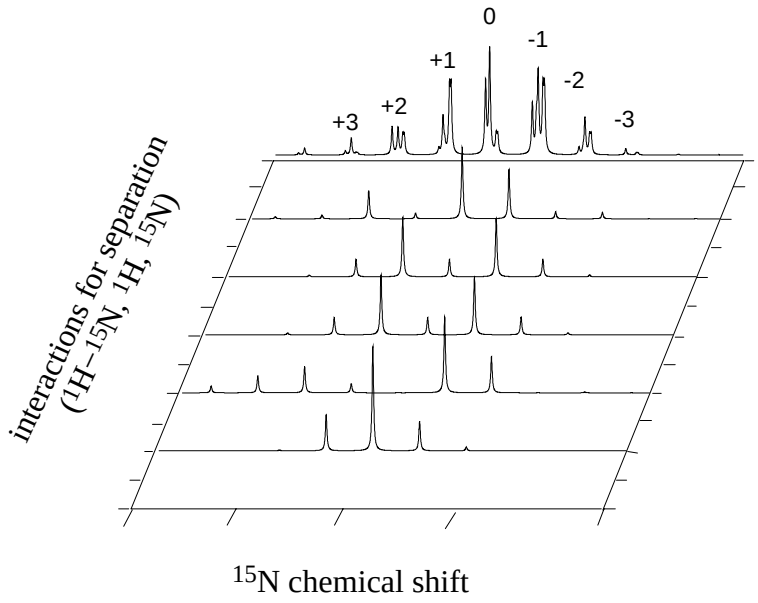

Figure 7.1: Multiple ^{15}N-Labelling of peptides or proteins requires a two-dimensional experiment in order to deconvolve all sideband families belonging to each spin. This simulation shows a ^{15}N-MAOSS experiment based on preliminary results and resolution obtained on ^{15}N-Met-labelled bR. Possible interactions for sideband separation are discussed in the text.

Bibliography

[1] S. J. Singer and G. L. Nicolson. The fluid mosaic model of the structure of membranes. *Science*, 175:720–731, 1972.

[2] J. A. F. On Den Kamp. Lipid asymmetry in membranes. *Annual Reviews in Biochemistry*, 48:47–71, 1979.

[3] A. Watts. Protein-lipid interaction at membrane surfaces. In R. Glaser and D. Gingell, editors, *Biophysics on the Cell Surface*, pages 23–50. Springer Verlag, 1990.

[4] R. R. Kopito and H. F. Lodish. Primary structure and transmembrane orientation of the murine anion-exchange protein. *Nature*, 316:234–238, 1985.

[5] P. J. R. Spooner and A. Watts. Cytochrome-c interactions with cardiolipin in bilayers - a multinuclear magic-angle spinning NMR study. *Biochemistry*, 31:10129–10138, 1992.

[6] J. A. G. Areas, G. Groebner, C. Glaubitz, and A. Watts. Interaction of a type II myosin with biological membranes studied by 2H solid state NMR. *Biochemistry*, 37:5582–5588, 1998.

[7] E. Sackmann. Biological membranes - architecture and function. In R. Lipowsky and E. Sackmann, editors, *Structure and Dynamics of Membranes*, pages 1–64. Elsevier, 1995.

[8] S. L. Hardt. Rates of diffusion controlled reactions in one, two and three dimensions. *Biophysical Chemistry*, 10:239–243, 1979.

[9] G. Cevc and D. Marsh. *Phospholipid Bilayers: Physical Principles and Models*. J. Wiley & Sons, New York, 1987.

[10] C. M. Fraser et al. The minimal gene complement of mycoplasma genitalium. *Science*, 270:397–403, 1995.

[11] J. Deisenhofer, O. Epp, K. Miki, R. Huber, and H. Michel. X-ray structure analysis of a membrane protein complex. *Journal of Molecular Biology*, 180:385–398, 1984.

[12] S. Iwata, C. Ostermeier, B. Ludwig, and H. Michel. Structure at 2.8 Angstrom resolution of cytochrome C oxidase from Paracoccus Denitrificans. *Nature*, 376:660–669, 1995.

[13] E. Pebay-Peyroula, G. Rummel, J.P. Rosenbusch, and E.M. Landau. X-Ray structure of bacteriorhodopsin at 2.5 Angstroms from microcrystals grown in lipidic cubic phases. *Science*, 277:1676–1681, 1997.

[14] Y. Kimura et al. Surface of bacteriorhodopsin revealed by high-resolution electron crystallography. *Nature*, 389:206–211, 1997.

[15] M. Mehring. *Principles of High Resolution NMR in Solids*. Springer Verlag, Berlin, 1983.

[16] M. E. Rose. *Elemenary Theory of Angular Momentum*. John Wiley, 1967.

[17] D. A. Varshalovich, A. N. Moskalev, and V. K. Khersonskii. *Quantum Theory of Angular Momentum*. World Scientific, Singapore, 1988.

[18] E. R. Andrew, A. Bradbury, and R. G. Eades. NMR spectra from crystals rotated at high speed. *Nature*, 182:1659–, 1958.

[19] I. J. Lowe. Free induction decays in rotating solids. *Physical Reviews Letters*, 2:285–, 1959.

[20] M. M. Maricq and J. S. Waugh. NMR in rotating solids. *Journal of Chemical Physics*, 70:3300–3316, 1979.

[21] K. Schmidt-Rohr and H. W. Spiess. *Multidimensional Solid-State NMR and Polymers*. Academic Press, London, 1994.

[22] J. Herzfeld and A. E. Berger. Sideband intensities in NMR spectra. *Journal of Chemical Physics*, 73:6021, 1980.

[23] C. P. Slichter. *Principles of Magnetic Resonance*. Springer Verlag, Berlin, 1980.

[24] B. J. van Rossum, H. Forster, and H. J. de Groot. High-field and high-speed CP-MAS C-13 NMR heteronuclear dipolar-correlation spectroscopy of solids with frequency-switched Lee-Goldburg homonuclear decoupling. *Journal of Magnetic Reseonance*, 124:516–519, 1997.

[25] B. C. Gerstein and C. R. Dybrowski. *Transient Techniques in NMR of Solids*. Academic Press, London, 1985.

[26] D. A. Hall. Polarisation-enhanced NMR spectroscopy of biomolecules in frozen solution. *Science*, 276:930–932, 1997.

[27] E. R. Andrew, A. Bradbury, R. G. Eades, and V. T. Wynn. *Physics Letters*, 4:99, 1963.

[28] E. R. Andrew, S. Clough, L. F. Farnell, and I. Roberts. *Physics Letters*, 21:505, 1966.

[29] D. P. Raleigh, M. H. Levitt, and R. G. Griffin. Rotational resonance in solid-state NMR. *Chemical Physics Letters*, 146(1-2):71–76, 1988.

[30] M. H. Levitt, D. P. Raleigh, F. Creuzet, and R. G. Griffin. Theory and simulations of homonuclear spin pair systems in rotating solids. *Journal of Chemical Physics*, 92(11):6347–6364, 1990.

[31] R. Tycko and G. Dabbagh. Measurements of S-S dipole couplings in MAS NMR (drama). *Chemical Physics Letters*, 173:461, 1990.

[32] A. E. Bennet, J. H. Ok, R. G. Griffin, and S. Vega. Chemical shift correlation spectroscopy in rotating solids: Radio frequency driven dipolar recoupling and longitudinal exchange. *Journal of Chemical Physics*, 96:8624–8627, 1992.

[33] B.-Q. Sun, P. R. Costa, D. Kocisko, P. T. Lansbury, and R. G. Griffin. Internuclear distance measurements in solid state NMR: Dipolar recoupling via rotor synchronized spin locking. *Journal of Chemical Physics*, 102:702–707, 1995.

[34] Y. K. Lee, N. D. Kurur, M. Helmle, O. G. Johannessen, N. C. Nielsen, and M. H. Levitt. Efficient dipolar recoupling in the NMR of rotating solids. a sevenfold symmetric radiofrequency pulse sequence. *Chemical Physics Letters*, 242:304–309, 1995.

[35] T. Gullion and J. Schaefer. Detection of weak hetreonuclear couplings by REDOR. *Advances in Magnetic Resonance*, 13:57, 1989.

[36] S. J. Opella. NMR and membrane proteins. *Nature Structural Biology*, 4:845–848, 1997.

[37] T. A. Cross and S. J. Opella. Solid-state NMR structural studies of peptides and proteins in membranes. *Current Opinion in Structural Biology*, 4:574–581, 1994.

[38] S. O. Smith, K. Aschheim, and M. Groesbeek. Magic angle spinning NMR spectroscopy of membrane proteins. *Quarterly Reviews of Biophysics*, 29(4):395–449, 1996.

[39] R. Tycko. Prospects for resonance assignments in multidimensional solid-state NMR-spectra of uniformly labelled proteins. *Journal of Biomolecular NMR*, 8:239–251, 1996.

[40] F.J.M van de Ven, J.W.M van Os, J.M.A. Aelen, S.S. Wymenga, M.L. Remerowski, R.N.H Konings, and C.W. Hilbers. Assignment of H-1, N-15,

and backbone C-13 resonances in detergent-solubilized M13 coat protein via multinuclear multidimensional NMR - a model for the coat protein monomer. *Biochemistry*, 32:8322–8328, 1993.

[41] H. Patzelt et al. Towards structural investigations on isotope labelled native bacteriorhodopsin in detergent micelles by solution-state NMR spectroscopy. *Journal of Biomolecular NMR*, 10:95–106, 1997.

[42] A. S. Ulrich, I. Wallat, M. P. Heyn, and A. Watts. Re-orientation of retinal in the M-photointermediate of bacteriorhodopsin. *Nature Structural Biology*, 2:190–192, 1995.

[43] G. Groebner, G. Choi, I. J. Burnett, C. Glaubitz, P.J.E. Verdegem, J. Lugtenburg, and A. Watts. Photoreceptor rhodopsin: Structural and conformational study of it's chromophore 11-cis retinal in oriented membranes by deuterium solid state NMR. *FEBS Letters*, 422:201–204, 1998.

[44] R.R. Ketchem, W. Hu, and T. A. Cross. High-resolution conformation of gramicidin a in a lipid bilayer by solid state NMR. *Science*, 261:1457–60, 1993.

[45] B. Bechinger, L. M. Gierasch, M. Montal, M. Zasloff, and S. J. Opella. Orientations of helical peptides in membrane bilayers by solid state NMR spectroscopy. *Solid State NMR*, 7:185–191, 1996.

[46] G. Gröbner, A. Taylor, P.T.F. Williamson, G. Choi, C. Glaubitz, J.A. Watts, W.J. de Grip, and A. Watts. Macroscopic orientation of natural and model membranes for structural studies. *Analytical Biochemistry*, 254:132–138, 1997.

[47] C. R. Sanders, B. J. Hare, K. Howerd, and J. H. Prestegard. Magnetically-oriented phospholipid micelles as a tool for the study of membrane-associated molecules. *Progress in NMR Spectroscopy*, 26:421–444, 1993.

[48] S. R. Prosser, S. A. Hunt, J. A. Dinatale, and R. R. Vold. Magnetically aligned membrane model systems with positive order parameters: Switching the sign of Szz with paramagnetic ions. *Journal of the American Chemical Society*, 118:269–270, 1996.

[49] K. P. Howard and S. J. Opella. High-resolution solid-state NMR spectra of integral membrane proteins reconstituted into magnetically oriented phospholipid bilayers. *Journal of Magnetic Resonance*, 112:91–94, 1996.

[50] F. M. Marassi, A. Ramamoorthy, and S. J. Opella. Complete resolution of the solid-state NMR spectrum of a uniformly 15N-labeled membrane protein in phospholipid bilayers. *Proceedings of the National Academy of Sciences*, 94:8551–8556, 1997.

[51] P. J. R. Spooner, N. G. Rutherford, A. Watts, and P. J. F. Henderson. NMR observation of substrate in the binding site of an active sugar-H+ symport protein in native membranes. *Proceeedings of the National Academy of Sciences*, 91:3877–3881, 1994.

[52] D. A. Middleton, R. Robins, X. L. Feng, M. H. Levitt, I. D. Spiers, C. H. Schwalbe, D. G. Reid, and A. Watts. The conformation of an inhibitor bound to gastric proton pump. *FEBS Letters*, 410:269–274, 1997.

[53] P. T. F. Williamson, G. Groebner, K. Miller, and A. Watts. Solid state nuclear magnetic resonance of ligand protein interaction in the nicotinic acetylcholine receptor. *Biochemistry*, page in press, 1998.

[54] X. Feng, P. J. E. Verdegem, Y. K. Lee, D. Sandstrom, M. Eden, P. BoveeGeurts, W. J. de Grip, J. Lugtenburg, H. J. M de Groot, and M. H. Levitt. Direct determination of a molecular torsional angle in the membrane protein rhodopsin by solid-state NMR. *Journal of the American Chemical Society*, 119:6853–6857, 1997.

[55] R. Smith, F. Separovic, F. C. Bennet, and B. A. Cornell. Melittin-induced changes in lipid multilayers - a solid state NMR study. *Biophysical Journal*, 63:469–474, 1992.

[56] S. Haffner and H. W. Spiess. Advanced solid-state NMR spectroscopy of strongly dipolar coupled spins under fast magic angle spinning. *Concepts in Magnetic Resonance*, 10(2):99–128, 1998.

[57] J. Gottwald, D. E. Demco, R. Graf, and H. W. Spiess. High-resolution double-quantum NMR spectroscopy of homonuclear spin pairs and proton connectivities in solids. *Chemical Physics Letters*, 243:314–323, 1995.

[58] C. Filip, X. Filip, D. E. Demco, and S. Hafner. Spin dynamics under magic angle spinning by Floquet formalism. *Molecular Physics*, 92(4):757–771, 1997.

[59] E. Oldfield, J. L. Bowers, and J. Forbes. High-resolution proton and C-13 NMR of membranes - why sonicate. *Biochemistry*, 26:6919–6923, 1987.

[60] J. Forbes, C. Husted, and E. Oldfield. High-field, high-resolution proton magic-angle sample-spinning nuclear magnetic-resonance spectroscopy studies of gel and liquid-crystalline lipid bilayers and the effects of cholesterol. *Journal of the American Chemical Society*, 110:1059–1065, 1988.

[61] J. Forbes, J. Bowers, X. Shan, L. Moran, E. Oldfield, and M.A. Moscarello. Some new developments in solid-state nuclear magnetic-resonance spectroscopic studies of lipids and biological-membranes, including the effects of cholesterol in model and natural systems. *Journal of the Chemical Society - Faraday Transactions*, 84:3821–3849, 1988.

[62] J. H. Davis, M. Auger, and R. S. Hodges. High resolution H-1 nuclear magnetic resonance of a transmembrane peptide. *Biophysical Journal*, 69:1917–1932, 1995.

[63] C. Le Guerneve and M. Seigneure. High-resolution monodimensional and multidimensional magic-angle-spinning H-1 nuclear-magnetic-resonance of

membrane peptides in nondeuterated lipid-membranes and H2O. *Biophysical Journal*, 71:2633–2644, 1996.

[64] F. Volke and A. Pampel. Membrane hydration and structure on a subnanometer scale as seen by high-resolution solid-state nuclear-magnetic-resonance - POPC and POPC/C12EO4 model membranes. *Biophysical Journal*, 68:1960–1965, 1995.

[65] A. Pampel and F. Volke. Rotational side bands in two-dimensional proton high-resolution MAS NMR spectra. *Journal of Magnetic Resonance Analysis*, 3:193–198, 1997.

[66] F. Volke, A. Pampel, M. Haensler, and G. Ullmann. Proton MAS NMR of a protein in a frozen aqueous-solution. *Chemical Physics Letters*, 262:374–378, 1996.

[67] M. Bouchard, J. H. Davis, and M. Auger. High-speed magic-angle-spinning solid-state H-1 nuclear-magnetic-resonance study of the conformation of gramicidin A in lipid bilayers. *Biophysical Journal*, 69:1933–1938, 1995.

[68] J.C. Sanders, P.I. Haris, D. Chapman, C. Otto, and M.A. Hemminga. Secondary structure of M13 coat protein in phospholipids studied by circular-dichroism, Raman, and fourier-transform ir. *Biochemistry*, 32:12446–12454, 1993.

[69] K. Weisz, G. Gröbner, C. Mayer, J. Stohrer, and G. Kothe. Deuteron nuclear magnetic resonance study for the dynamic organization of phospholipid/cholesterol bilayer membranes: Molecular properties and viscoelastic behavior. *Biochemistry*, 31:1100–1112, 1992.

[70] J. Stohrer, G. Gröbner, D. Reimer, K. Weisz, C. Mayer, and G. Kothe. Collective lipid motions in bilayer-membranes studied by transverse deuteron spin relaxation. *Journal of Chemical Physics*, 95:672–678, 1991.

[71] M. Bloom and E. Evans. *Observations of Surface Undulations on the Mesoscopic Length Scale by NMR.* Plenum Press, New York, 1991.

[72] J. Davis. The description of membrane lipid conformation, order and dynamics by deuterium NMR. *Biochimica Biophysica Acta*, 597:477–491, 1980.

[73] J. Seelig. Deuterium magnetic resonance: Theory and application to lipid membranes. *Quarterly Reviews of Biophysics*, 10:345–418, 1977.

[74] A. Watts. *Dynamic Properties of Biomolecular Assemblies*, pages 320–347. Royal Chemical Society, London, 1988.

[75] U. Haeberlen and J. S. Waugh. Coherent averaging effects in magnetic resonance. *Physical Review*, 175:453–467, 1968.

[76] A. Sodickson and D. G. Cory. Shimming a high-resolution MAS probe. *Journal of Magnetic Resonance*, 128:87–91, 1997.

[77] J.D.J. O'Neil and B.D. Sykes. Structure and dynamics of a detergent-solubilized membrane protein: Measurements of amide hydrogen exchange rates in M13 coat protein by H-1 NMR spectroscopy. *Biochemistry*, 27:2753–2762, 1988.

[78] G. D. Henry and B. D. Sykes. Assignment of amide H-1 and N-15 NMR resonances in detergent-solubilized M13 coat protein: A model for the coat protein dimer. *Biochemistry*, 31:5284–5297, 1992.

[79] K. P. Datema, B. J. H. van Boxtel, and M. A. Hemminga. Dynamic properties of M13 coat protein in mixed bilayers. a deuterium NMR study of exchangeable sites. *Journal of Magnetic Resonance*, 77:372–376, 1988.

[80] W.F. Wolkers, R.B. Spruijt, A. Kaan, R.N.H. Konings, and M.A. Hemminga. Conventional and saturation-transfer EPR of spin-labeled mutant bacteriophage M13 coat protein in phospholipid bilayers. *BBA-Biomembranes*, 1327:5–16, 1997.

[81] P. A. McDonnell, L. Shon, Y. Kim, and S. J. Opella. fd Coat protein-structure in membrane environments. *Journal of Molecular Biology*, 233:447–463, 1993.

[82] F.C.L. Almeida and S.J. Opella. fd Coat protein structure in membrane environments: Structural dynamics of the loop between the hydrophobic trans-membrane helix and the amphipathic in-plane helix. *Journal of Molecular Biology*, 270:481–495, 1997.

[83] T. A. Cross and S. J. Opella. H-1 and C-13 nuclear magnetic resonance of the aromatic residues of fd coat protein. *Biochemistry*, 20:290–297, 1981.

[84] G. C. Leo, L. A. Colnago, K. G. Valentine, and S. J. Opella. Dynamics of fd-coat protein in lipid bilayers. *Biochemistry*, 26:854–862, 1987.

[85] G.D. Henry, J.H. Weiner, and B.D. Sykes. Backbone dynamics of a model membrane-protein - C-13 NMR- spectroscopy of alanine methyl-groups in detergent-solubilized M13 coat protein. *Biochemistry*, 25:590–598, 1986.

[86] H. D. Dettman, J.H. Weiner, and B.D. Sykes. Phenylalanyl and tyrosyl side-chain mobility in the M13 coat protein resonstituted in phospholipid-vesicles. *Biochemistry*, 23:705–712, 1984.

[87] N.J.P. Ryba and D. Marsh. Protein rotational diffusion and lipid protein interactions in recombinants of bovine rhodopsin with saturated diacylphospatidylcholines different chain lengths studied by conventional and saturation-transfer electron-spin-resonance. *Biochemistry*, 31:7511–7518, 1992.

[88] Z. Song, O. N. Antzutkin, Y. K. Lee, S. C. Shekar, A. Rupprecht, and M. H. Levitt. Conformational transition of the phosphodiester backbone in native DNA: Two-dimensional magic-angle-spinning 31P-NMR of DNA fibres. *Biophysical Journal*, 73:1539–1552, 1997.

[89] M. Baldus, T. O. Levante, and B. H. Meier. Numerical simulations of magnetic resonance experiments: Concepts and applications to static, rotating and double rotating experiments. *Zeitschrift fuer Naturforschung*, 49a:80–88, 1993.

[90] S. A. Smith, T. O. Levante, B. H. Meier, and R. R. Ernst. Computer simulations in magnetic resonance. *Journal of Magnetic Resonance A*, 106:75–105, 1994.

[91] J. H. Shirley. Solution of the schroedinger equation with a hamiltonian periodic in time. *Physical Review*, B138:979–987, 1965.

[92] S. Vega, E. T. Olejniczak, and R. G. Griffin. Rotor frequency lines in the nuclear magnetic resonance spectra of rotating solids. *Journal of Chemical Physics*, pages 4832–4840, 1984.

[93] T. O. Levante, M. Baldus, B. H. Meier, and R. R. Ernst. Formalized quantum mechanical Floquet theory and its application to sample spinning in nuclear magnetic resonance. *Molecular Physics*, 86:1195–1212, 1995.

[94] R. R. Ernst, G. Bodenhausen, and A. Wokaun. *Principles of Nuclear Magnetic Resonance in One and Two Dimensions*. Clarendon Press, Oxford, 1987.

[95] M.J. Janiak, D. M. Small, and G.G. Shipley. Nature of the thermal pretransition of synthetic phospholipids: Dimyristoyl- and dipalmitoyllecithin. *Biochemistry*, 15:4575–4577, 1976.

[96] A. Watts, K. Harlos, W. Maschke, and D. Marsh. Control of structure and fluidity of phosphatidylglycerol bilayers by pH-titration. *Biochimica Biophysica Acta*, 510:63–74, 1978.

[97] C. Le Guerneve and M. Auger. New approach to study fast and slow motions in lipid bilayers - application to dimyristoylphospahatidylcholine - cholesterol interactions. *Biophysical Journal*, 68:1952–1959, 1995.

[98] D.L. VanderHart. Characterization of the methylene C-13 chemical shift tensor in the normal alkane N-C20H42. *Journal of Chemical Physics*, 64:830–834, 1976.

[99] K. Schmidt-Rohr, M. Wilhelm, A. Johansson, and H. W. Spiess. Determination of chemical-shift tensor orientations in methylene groups by seperated-local-field NMR. *Magnetic Resonance in Chemistry*, 31:352–356, 1993.

[100] Z.Y. Song, O.N. Antzutkin, A. Rupprecht, and M.H. Levitt. Order-resolved side-band separation in magic-angle-spinning NMR - 31P-NMR of oriented DNA fibres. *Chemical Physics Letters*, 253:349–354, 1997.

[101] M. Hong, J.D. Gross, and R.G. Griffin. Site-resolved determination of peptide torsion angle phi from the relative orientations of backbone N-H and C-H bonds by solid-state NMR. *Journal of Physical Chemistry*, 101:5869–5874, 1997.

[102] X. Feng, Y.K. Lee, D. Sandstrom, M. Eden, H. Maisel, A. Sebald, and M.H. Levitt. Direct determination of a molecular torsional angle by solid-state NMR. *Chemical Physics Letters*, 257:314–320, 1996.

[103] Y. Tomita, E.J. O'Connor, and A. McDermott. A method for dihedral angle measurement in solids - rotational resonance NMR of a transition-state inhibitor of triose phosphate isomerase. *Journal of the American Chemical Society*, 116:8766–8771, 1994.

[104] D. Oesterhelt and W. Stoeckenius. Functions of a new photoreceptor membrane. *Proceedings of the National Academy of Sciences*, 70:2853–2857, 1973.

[105] H. G. Khorana. Two light-transducing membrane proteins: Bacteriorhodopsin and the mammalian rhodopsin. *Proceedings of the National Academy of Sciences*, 90:1166–1171, 1993.

[106] J. Baldwin, R. Henderson, E. Beckman, and F. Zemlin. Images of pm at 0.28 nm resolution obtained by cryo-electron microscopy. *Journal of Molecular Biology*, 202:585–581, 1988.

[107] Y. A. Ovichinnikov, N. G. Abdulaev, M. Y. Feigina, A. V. Kieslev, and N. A. Lobdanov. The structural basis of the functioning bacteriorhodopsin: An overview. *FEBS Letters*, 100:219–224, 1979.

[108] R. Henderson, J. M. Baldwin, T. A. Ceska, F. Zemlin, E. Beckmann, and K. H. Downing. Model for the structure of bacteriorhodopsin based on high-resolution cryo-microscopy. *Journal of Molecular Biology*, 213:899–929, 1990.

[109] C. Nicolini. *Molecular Bioelectronics*. World Scientific Publ., 1996.

[110] F. Creuzet, A. Mcdermott, R. Gebhard, K. Vanderhoef, M. B. Spijkerassink, J. Herzfeld, J. Lugtenburg, M. H. Levitt, and R. G. Griffin. Determination of membrane-protein structure by rotational resonance NMR - bacteriorhodopsin. *Science*, 251(4995):783–786, 1991.

[111] J. G. Hu, B. Q. Sun, A. T. Petkova, R. G. Griffin, and J. Hertzfeld. The predischarge chromophore in bacteriorhodopsin: A 15N solid-state NMR study of the L photointermediate. *Biochemistry*, 36:9316–9322, 1997.

[112] J. G. Hu, B. Q. Sun, M. Bizounok, M. E. Hatcher, J. C. Lansing, J. Raap, P. J. E. Verdegem, J. Lugtenburg, R. G. Griffin, and J. Hertzfeld. Early and late M intermediates in the bacteriorhodopsin photocycle: A solid-state NMR study. *Biochemistry*, 37:8088–8096, 1998.

[113] H. G. Khorana. Bacteriorhodopsin, a membrane protein that uses light to translocate protons. *The Journal of Biological Chemistry*, 263:7439–7442, 1988.

[114] R. S. Prosser, S. I. Daleman, and J. H. Davis. The structure of an integral membrane peptide: A deuterium NMR relaxation study of gramicidin. *Biophysical Journal*, 66:1415–1428, 1994.

[115] R. S. Prosser, J. H. Davis, C. Mayer, K. Weisz, and G. Kothe. Deuterium NMR relaxation studies of peptide-lipid interactions. *Biochemistry*, 31:9355–9363, 1992.

[116] A. Watts. *Magnetic Resonance Studies of Phospholipid-Protein Interactions in Bilayers*, pages 687–740. Marcel Dekker, New York, 1993.

[117] R. S. Prosser and J. H. Davis. Dynamics of an integral membrane peptide: A deuterium NMR relaxation study of gramicidin. *Biophysical Journal*, 66:1429–1440, 1994.

[118] A. Watts and S.J. Opella. Membranes studied by NMR spectroscopy. In John C. Lindon, editor, *Encyclopedia of Spectroscopy and Spectrometry.* Academic Press, 1998.

[119] J. L. Ackerman, R. Eckman, and A. Pines. Experimental results on deuterium NMR in the solid state by magic angle sample spinning. *Chemical Physics*, 42:423–428, 1979.

[120] A. E. Aliev, K. D. M. Harris, and D. C. Apperley. Natural abundance high-resolution solid state 2H NMR spectroscopy. *Chemical Physics Letters*, 226:193–198, 1994.

[121] A. J. Kim and L. G. Butler. Resolving two inequivalent sites with deuterium MAS NMR. *Journal of Magnetic Resonance*, 99:292–300, 1992.

[122] N. J. Clayden. Computer simulations of H-2 MAS NMR spinning sideband spectra. *Chemical Physics Letters*, 131:517–521, 1986.

[123] J. H. Kristensen, H. Bildsoe, H. J. Jakobsen, and N. C. Nielsen. Deuterium quadrupole couplings from least-squares computer simulations of 2H MAS NMR spectra. *Journal of Magnetic Resonance*, 92:443–453, 1991.

[124] D. Reichert, Z. Olender, R. Poupko, H. Zimmermann, and Z. Luz. Deuterium two-dimensional exchange nuclear magnetic resonance by rotor-

synchronized magic angle spinning. *Journal of Chemical Physics*, 98:7699–7710, 1993.

[125] D. Marks, N. Zumbulyadis, and S. Vega. Deuterium cross-polarization magic-angle spinning. *Journal of Magnetic Resonance*, 122:16–36, 1996.

[126] D. Oesterhelt. Reconstitution of the retinal proteins bacteriorhodopsin and halorhodopsin. *Methods in Enzymology*, 88:11–17, 1982.

[127] D. Oesterhelt and W. Stoeckenius. Isolation of the cell membrane of halobacterium halobium and it's fractionation into red and purple membranes. *Methods of Enzymology*, 31:667–678, 1974.

[128] V. Copie, A. McDermott, K. Beshah, J. C. Williams, M. Spijker-Assink, R. Gebhard, J. Lugtenburg, J. Hertzfeld, and R. G. Griffin. Deuterium solid-state nuclear magnetic resonance studies of methyl group dynamics in bacteriorhodopsin and retinal model compounds: Evidence for a 6-s-trans chromophore in the protein. *Biochemistry*, 33:3280–3286, 1994.

[129] A. S. Ulrich and A. Watts. H-2 NMR lineshapes of immobilized uniaxially oriented membrane - proteins. *Solid State NMR*, 2:21–36, 1993.

[130] B. S. Kumar, K. V. Ramanathan, C. L. Khetrapal, S. J. Opella, and E. D. Becker. Determination of the sign of the order parameter from MAS spectra of oriented molecules. *Journal of Magnetic Resonance*, 86:516–525, 1990.

[131] W. H. Press, S. A. Teukolsky, W. T. Vetterling, and B. P. Flannery. *Numerical Recipes*. Cambridge University Press, 1992.

[132] A. S. Ulrich, A. Watts, I. Wallat, and M. P. Heyn. Distorted structure of retinal chromophore in bacteriorhodopsin resolved by 2H-NMR. *Biochemistry*, 33:5370–5375, 1994.

[133] N. Grigorieff, T. A. Ceska, K. H. Downing, J. M. Baldwin, and R. Henderson. Electron-crystallographic refinement of the structure of bacteriorhodopsin. *Journal of Molecular Biology*, 259:393–421, 1996.

[134] K. Koyama. Direct measurements for iosmer ratios of retinal in bacteriorhodopsin by an electrochemical method. *Photochemistry and Photobiology*, 66:784–787, 1997.

[135] M. Russel, N. A. Linderoth, and A. Sali. Filamentous phage assembly: Variations on a protein export theme. *Gene*, 192:23–32, 1997.

[136] P.M.G.F. Van Wezenbeck, T.J.M. Hulsebos, and J.G.G.Schoenmakers. *Gene*, 11:129–148, 1980.

[137] D. A. Marvin. Filamentous bacterial viruses. *Journal of Biosciences*, 8:799–813, 1985.

[138] D. A. Marvin and E.J. Wachtel. Structure and assembly of filamentous bacterial viruses. *Nature*, 253:19–23, 1975.

[139] K. Sugmoto, K. Sugiski, and M. Takanami. *Journal of Molecular Biology*, 110:487–507, 1977.

[140] D. A. Marvin. Filamentous phage structure, infection and assembly. *Current Opinion in Structural Biology*, 8:150–158, 1998.

[141] R. Bayer and G.W. Feigenson. Reconstitution of M13 bacteriophage coat protein - a new strategy to analyze configuration of the protein in the membrane. *Biochimica et Biophysica Acta*, 815:369–379, 1985.

[142] J. Beck et Al. *Nucleic Acids Research*, 5:4495–4503, 1978.

[143] T.A. Cross and S.J. Opella. Protein structure by solid state nuclear magnetic resonance-residues 40 to 45 of bacteriophage fd coat protein. *Journal of Molecular Biology*, 182:367–381, 1985.

[144] K.G. Valentine, D.M. Schneider, G.C. Leo, L.A. Colnago, and S.J. Opella. Structure and dynamics of fd-coat protein. *Biophysical Journal*, 49:36–38, 1986.

[145] Y.Nozaki, J. Reynolds, and C. Tanford. *Biochemistry*, 17:1239–1246, 1978.

[146] K.P. Datema, A.J.W.G Visser, A. VanHoek, C.J.A.M. Wolfs, R.B. Spruijt, and M.A. Hemminga. Time resolved tryptophan fluorescence anisotropy investigation of bacteriophage M13 coat protein in micelles and mixed bilayers. *Biochemistry*, 26:6145–6152, 1987.

[147] R. B. Spruijt and M. A. Hemminga. The in situ aggregational and conformational state of the major coat protein of bacteriophage M13 in phospholipid bilayers mimicking the inner membrane of host Escherichia coli. *Biochemistry*, 30:11147–11154, 1991.

[148] M.A. Hemminga, J.C. Sanders, and R.B. Spruijt. Spectroscopy of lipid protein interactions - structural aspects of 2 different forms of the coat protein of bacteriophage M13 incorporated in model membranes. *Progress in Lipid Research*, 31:301–333, 1992.

[149] G.D. Henry and B.D. Sykes. Hydrogen exchange kinetics in a membrane protein determined by N-15 NMR spectroscopy-use of the INEPT experiments to follow individual amides in detergent solubilized M13 coat protein. *Biochemistry*, Vol.29:6303–6313, 1990.

[150] C. H. M. Papavoine, M. L. Remerowski, L. M. Horstink, R. N. H. Konings, C. W. Hilbers, and F.J.M. Van de Ven. Backbone dynamics of the major coat protein of bacteriophage M13 in detergent micelles by 15N-NMR relaxation measurements using the model-free approach and reduced spectral density mapping. *Biochemistry*, 36:4015–4026, 1997.

[151] R.G.S. Spencer, K.J. Halverson, M. Aauger, A.E. McDermott, R.G. Griffin, and P.T. Lansbury. An unusual peptide conformation may precipitate amyloid formation in Alzheimer's disease - application of solid-state NMR to the determination of protein secondary structure. *Biochemistry*, 30:10382–10387, 1991.

[152] D. P. Raleigh, F. Creuzet, S. K. Das Gupta, M. H. Levitt, and R. G. Griffin. Measurement of internuclear distances in polycrystalline solids:

Rotationally enhanced transfer of nuclear spin magnetization. *Journal of the American Chemical Society*, 111(12):4502–4503, 1989.

[153] O. B. Peersen, S. Yoshimura, H. Hojo, S. Aimoto, and S. O. Smith. Rotational resonance NMR measurements of internuclear distances in an alpha-helical peptide. *Journal of the American Chemical Society*, 114(11):4332–4335, 1992.

[154] L. K. Thompson, A. E. Mcdermott, J. Raap, C. M. Vanderwielen, J. Lugtenburg, J. Herzfeld, and R. G. Griffin. Rotational resonance NMR-study of the active-site structure in bacteriorhodopsin - conformation of the Schiff-base linkage. *Biochemistry*, 31(34):7931–7938, 1992.

[155] J. Heller, A. C. Kolbert, R. Larsen, M. Ernst, T. Bekker, M. Baldwin, S. B. Prusiner, A. Pines, and D. E. Wemmer. Solid-state NMR-studies of the prion protein H1 fragment. *Protein Science*, 5(8):1655–1661, 1996.

[156] P. T. Lansbury, P. R. Costa, J. M. Griffiths, E. J. Simon, M. Auger, K. J. Halverson, D. A. Kocisko, Z. S. Hendsch, T. T. Ashburn, R. G. S. Spencer, B. Tidor, and R. G. Griffin. Structural model for the beta-amyloid fibril based on interstrand alignment of an antiparallel-sheet comprising a C-terminal peptide. *Nature Structural Biology*, 2(11):926–928, 1995.

[157] A. Kubo and C. A. McDowell. Spectral spin diffusion in polycrystalline solids under magic-angle spinning. *Journal of the Chemical Society - Faraday Transaction*, 84(11):3713–3730, 1988.

[158] P. J. E. Verdegem, M. Helmle, J. Lugtenburg, and H.J.M. DeGroot. Internuclear distance measurements up to 0.44 nm for retinals in the solid state with 1-D rotational resonance C-13 MAS NMR spectroscopy. *Journal of the American Chemical Society*, 119(1):169–174, 1997.

[159] G. Metz, X. Wu, and S. O. Smith. Ramped-amplitude cross-polarisation in magic-angle-spinning NMR. *Journal of Magnetic Resonance A*, 110(2):219–227, 1994.

[160] P. Caravatti, G. Bodenhausen, and R. R. Ernst. Selective pulse experiments in high-resolution solid-state NMR. *Journal of Magnetic Resonance*, 55(1):88–103, 1983.

[161] A. E. Mcdermott, F. Creuzet, R. Gebhard, K. Vanderhoef, M. H. Levitt, J. Herzfeld, J. Lugtenburg, and R. G. Griffin. Determination of internuclear distances and the orientation of functional-groups by solid-state NMR - rotational resonance study of the conformation of retinal in bacteriorhodopsin. *Biochemistry*, 33(20):6129–6136, 1994.

[162] P.R. Costa, D.A. Kocisko, B.Q. Sun, P.T. Lansbury, and R.G. Griffin. Determination of peptide amide configuration in a model amyloid fibril by solid-state NMR. *Journal of the American Chemical Society*, 119(43):10487–10493, 1997.

[163] A. Abragam. *Principles of Nuclear Magnetism*. Oxford University Press, 1961.

[164] Q. Teng and T. A. Cross. The in situ determination of the 15N chemical-shift tensor orientation in a polypeptide. *Journal of Magnetic Resonance*, 85:439–447, 1989.

[165] C.J. Hartzell, M. Whitfield, T.G. Oas, and G. P. Drobny. Determination of the 15N and 13C chemical shift tensors of L-[13C]Alanyl-L-[15N]alanine from the dipole-coupled powder patterns. *Journal of the American Chemical Society*, 109:5966–5969, 1987.

[166] R.E. Stark, L. W. Jelinski, D. J. Ruben, D. A. Torchia, and R. G. Griffin. 13C chemical shift and 13C-15N dipolar tensors for the peptide bond: [1-13C]Gycyl[15N]glycine.HCL.H2O. *Journal of Magnetic Resonance*, 55:266–273, 1983.

[167] K. Eichele, M. D. Lumsden, and R. E. Wasylishen. Nitrogen-14 coupled dipolra-chemical shift 13C NMR spectra of the amide fragment of peptides in the solid state. *Journal for Physical Chemistry*, 97:8909–8916, 1993.

[168] A. E. Walling, R. E. Pargas, and A. C. de Dios. Chemical shift tensors in peptides: A quantum mechanical study. *Journal of Physical Chemistry*, 101:7299–7303, 1997.

[169] T.E. Creighton. *Proteins - Structure and Molecular Properties*. W. H. Freeman, 1993.

[170] F. Creuzet, D.P. Raleigh, M.H. Levitt, and R.G. Griffin. NMR magnetization exchange trajectories at rotational resonance: Determination of molecular structures in polycrystalline solid. *in preparation*.

[171] O. B. Peersen, M. Groesbeek, S. Aimoto, and S. O. Smith. Analysis of rotational resonance magnetization exchange curves from crystalline peptides. *Journal of the American Chemical Society*, 117(27):7228–7237, 1995.

[172] J. Heller, R. Larsen, M. Ernst, A. C. Kolbert, M. Baldwin, S. B. Prusiner, D. E. Wemmer, and A. Pines. Application of rotational resonance to inhomogeneously broadened systems. *Chemical Physics Letters*, 251(3-4):223–229, 1996.

[173] Q.Teng, M. Iqbal, and T.A. Cross. Determination of the 13C chemical shift and 14N electric field gradient tensor orientations with respect to the molecular frame in a polypeptide. *Journal of the American Chemical Society*, 114:5312–5321, 1992.

[174] J.G. Hexem, M.H. Frey, and S.J. Opella. Influence of 14N on 13C NMR spectra of solids. *Journal of the American Chemical Society*, 103:226–228, 1981.

[175] A. C. Olivieri. Quadrupolar effects in the CPMAS NMR spectra of spin-1/2 nuclei. *Journal of Magnetic Resonance*, 81:201–205, 1989.

[176] K.A. Williams and C. M. Deber. Biophysical characterization of wild-type and mutant bacteriophage IKe majot coat protein in the virion and in detergent micelles. *Biochemistry*, 35:10472–10483, 1996.

[177] A.R. Khan, K. A. Williams, J. M. Boggs, and C. M. Deber. Accessibility and dynamics of Cys residues in bacteriophage IKe and M13 major coat protein mutants. *Biochemistry*, 34:12388–12397, 1995.

[178] E. Thiaudiere, M.Soekarjo, E. Kuchinka, A. Kuhn, and H.Vogel. Structural characterization of membrane insertion of M13 procoat, M13 coat and Pf3 coat proteins. *Biochemistry*, 32:12186–12196, 1993.

[179] J. U. Bowie. Helix packing in membrane proteins. *Journal of Molecular Biology*, 272:780–789, 1997.

[180] H. Hauser, M.C. Philips, B.A. Levine, and R.J.P. Williams. Conformation of the lecithin polar group in charged vesicles. *Nature*, 261:390–394, 1976.

[181] H. Hauser, C.C.Hinckley, J.Krebs, B.A.Levine, M.C. Philips, and R.J.P. Williams. The interaction of ions with phosphatidylcholine bilayers. *Biochimica et Biophysica Acta*, 468:364–377, 1977.

[182] H. Hauser, M. C. Philips, B.A. Levine, and R.J.P. Williams. Ion-binding to phospholipids. *European Journal of Biochemistry*, 58:133–144, 1975.

[183] J. Villalain. Location of cholesterol in model membranes by magic-angle-spinning NMR. *European Journal of Biochemistry*, 241:586–593, 1996.

[184] J. Villalain. Location of the toxic molecule abietic acid in model membranes by MAS-NMR. *Biochchimica et Biophysica Acta*, 1328:281–289, 1997.

[185] T.J.T. Pinheiro and A. Watts. Lipid specificity in the interaction of Cytochrome-C with anionic phospholipid-bilayers revealed by solid-state P-31 NMR. *Biochemistry*, 33:2451–2458, 1994.

[186] M.A. Carbone and MacDonald P.M. Cardiotoxin-II segregates phosphatidylglycerol from mixtures wityh phosphatydilcholine - P-31 and H-2 NMR spectroscopic evidenvce. *Biochemistry*, 35:3368–3378, 1996.

[187] S.J. Opella, M.H. Frey, and T.A. Cross. Detection of individual carbon resonances in solid proteins. *Journal of the American Chemical Society*, 101:5856–5857, 1979.

[188] V.F. Bystrov, Y.E. Shapiro, A. V. Viktorov, L.C. Borsukov, and L.D. Bergelson. 31-P-NMR signals from inner and outer surfaces of phospholipid membranes. *FEBS Letters*, 25:337–338, 1972.

[189] C.N. La Mar, W. Horrocks, and R.H. Holms. *NMR of Paramagnetic Molecules.* Academic Press, 1973.

[190] L.D.Bergelson. Paramagnetic hydrophilic probes in NMR investigations of membrane systems. In E.D. Korn, editor, *Methods in Membrane Biology*, chapter 4, pages 275–331. Plenum Press, 1978.

[191] R. A. Dwek. *Nuclear Magnetic Resonance in Biochemistry.* Clarendon Press, Oxford, 1973.

[192] J. Reuben and G.A. Elgavish. In K.A. Gschneider and L. Eyring, editors, *Handbook of the Physics and Chemistry of Rare Earth.* North Holland, New York, 1979.

[193] A. J. Vega and D. Fiat. *Molecular Physics*, 31:347, 1976.

[194] B. Bleaney. Nuclear magnetric resonance shifts in solution due to lanthanide ions. *Journal of Magnetic Resonance*, 8:91–100, 1972.

[195] R. S. Prosser, J. S. Hwang, and R. R.Vold. Magnetically aligned phospholipid bilayers with positive ordering: A new model membrane system. *Biochphysical Journal*, 74:2405–2418, 1998.

[196] L.C.M. Van Gorkom, L.I. Horvath, M.A.Hemminga, B. Sternberg, and A. Watts. Identification of trapped and boundary lipid-binding sites in M13 coat protein lipid complexes by deuterium NMR-spectroscopy. *Biochemistry*, 29:3828–3834, 1990.

[197] D. Stopar, K. A. J. Jansen, T. Pali, D. Marsh, and M. A. Hemminga. Membrane location of spin-labelled M13 coat protein mutants determined by paramagnetic relaxation agents. *Biochemistry*, 36:8261–8268, 1997.

[198] D. Neuhaus and M. Williamson. *The Nuclear Overhauser Effect.* VCH, 1989.

[199] B. Q. Sun, P. R. Costa, D. Kocisko, P. T. Lansbury, and R. G. Griffin. Internuclear distance measurements in solid-state nuclear-magnetic-resonance - dipolar recoupling via rotor synchronized spin locking. *Journal of Chemical Physics*, 102:702–707, 1995.

[200] Y. K. Lee, N. D. Kurur, M. Helmle, O. G. Johannessen, N. C. Nielsen, and M. H. Levitt. Efficient dipolar recoupling in the NMR of rotating solids - a sevenfold symmetrical radiofrequency pulse sequence. *Chemical Physics Letters*, 242:304–309, 1995.

[201] M. G. Colombo, B. H. Meier, and R. R. Ernst. Rotor-driven spin diffusion in natural-abundance C-13 spin systems. *Chemical Physics Letters*, 146(3,4):189–198, 1988.

[202] A. E. Mcdermott, F. Creuzet, R. G. Griffin, L. E. Zawadzke, and C. T. Walsh. Rotational resonance determination of the structure of an enzyme-inhibitor complex - phosphorylation of an (aminoalkyl)phosphinate inhibitor of D-alanyl-D-alanine ligase by ATP. *Biochemistry*, 29(24):5767–5775, 1990.

[203] T. Nakai and C. A. Mcdowell. Calculation of rotational resonance NMR-spectra using Floquet theory combined with perturbation treatment. *Molecular Physics*, 88(5):1263–1275, 1996.

[204] M. Eden, Y. K. Lee, and M. H. Levitt. Efficient simulation of periodic problems in NMR - application to decoupling and rotational resonance. *Journal of Magnetic Resonance Series A*, 120(1):56–71, 1996.

[205] J. M. Griffiths, T. T. Ashburn, M. Auger, P. R. Costa, R. G. Griffin, and P. T. Lansbury. Rotational resonance solid-state NMR elucidates a structural model of pancreatic amyloid. *Journal of the American Chemical Society*, 117(12):3539–3546, 1995.

[206] H. J. M. de Groot, S.O. Smith, A. C. Kolbert, J. M. L. Courtin, C. Winkel, J. Lugtenburg, J. Herzfeld, and R. G. Griffin. Iterative fitting of magic-angle-spinning NMR-spectra. *Journal of Magnetic Resonance*, 91:30–38, 1991.

[207] V. Muhajan and R.L. Suss. Crystal structure of acetylcholine perchlorate. *Journal for Crystallography and Molecular Structure*, 4:15–21, 1974.

Appendix A

Sample Handling Tools for MAOSS Experiments

Correct and precise sample handling is essential for the successful application of MAS spectroscopy to oriented biomembranes. Some simple tricks and tools can help to overcome some typical experimental problems.

Once the membranes are well aligned on glass disks, which can be achieved by either drying and re-hydrating or by centrifuging the samples onto the solid support [46], they have to be transferred into a MAS rotor (see Fig.A.1). The disks are microscope cover slips, which were custom made by Marienfeld GmbH [1] to fit precisely into a 7mm Bruker MAS rotor, which has an inner diameter of 5.5mm. Rotors and KelF caps were obtained from RotoTec GmbH [2]. One rotor can contain up to 100 disks. It is essential that slipping and wobbling of the disk stack during spinning is prevented, in order to achieve a stable and precise sample rotation. The samples are held in position by two home-made KelF inserts (Fig.A.2), which fit so tight, that they can only be inserted or extracted by using the positioning tool shown in Fig.A.4. Since it is mechanically awkward to place single disks one after each other into a rotor, a special mounting tool was constructed to simplify this procedure which is shown in Fig.A.3. Disks can be pre-aligned with respect to each other, re-hydrated and mounted into the MAS

[1] Marienfeld GmbH, Laboratory Glassware, P.O.Box 1523, 97965 Bad Mergentheim, Germany, Tel.:+49-7931-9777-0, Fax.:+49-7931-9777-11/12

[2] Rototec GmbH, Frankensteiner Str. 125, 64297 Darmstadt, Germany, Tel.:+49-6151-595640, Fax.: +49-6151-593485, www.rototec-spintec.com

rotor using this simple assembly. Finally, a KeLF insert has to be placed on top of the last disk to fix their position. An insertion/extraction tool which uses a single axis micropositioning system from World Precision Instruments [3], was designed for that purpose. The positioning system allows an insert to be placed at a pre-defined position, which is important to prevent damaging the glass disks (Fig.A.4).

[3]World Precision Instruments Ltd, Tel.:+44-1438-880025, Fax:.+44-1438-880026, www.wpiinc.com

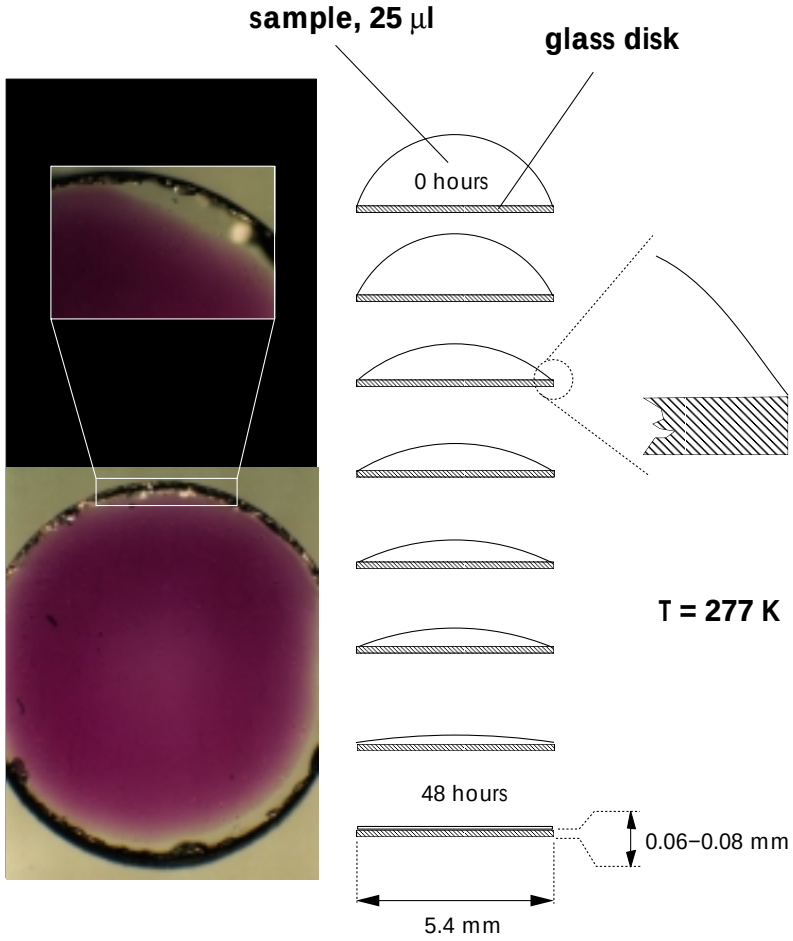

Figure A.1: Usually, 25 μl buffer solution containing lipid/protein vesicles at a concentration of 0.002-0.02 mg/μl were carefully dropped onto a the surface of a glass disk in such a way that one spherical drop covered the surface area completely. Bulk water was allowed to evaporate slowly over some hours. The photograph shows a glass disk carrying oriented bacteriorhodopsin (purple membrane).

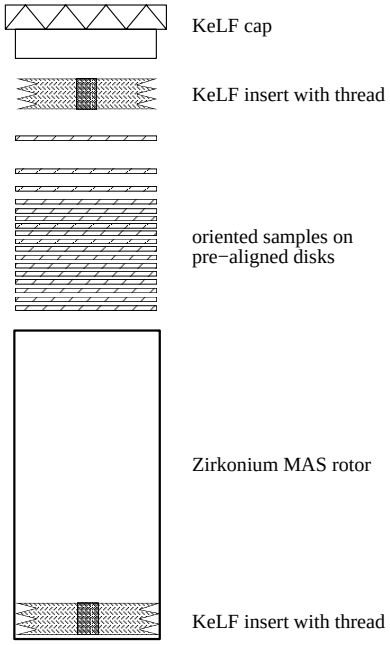

Figure A.2: A stable and precise alignment of the glass disks in the MAS rotor is achieved by fixing their position with precisely made and rather tight fitting KeLF inserts on top and bottom. These inserts prevent wobbling and slipping of the samples during spinning. The inserts can only be inserted and removed using a screw with a specific insertion/extraction tool.

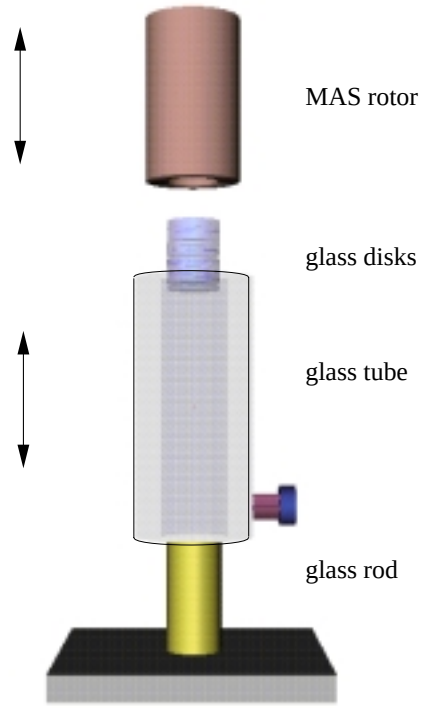

Figure A.3: The glass disks containing the membrane samples have to be pre-aligned before transferring them into the MAS rotor. They are carefully piled up on top of each other on top of a glass rod with exactly the same diameter as the disks. A movable glass tube, which can be fixed at any height keeps all disks well aligned with respect to each other. Usually, a glass tube with some horizontal opening was used, so that samples could be re-hydrated in this position if necessary. The stack of disks was mounted into the rotor by placing an rotor onto the glass tube and sliding it down.

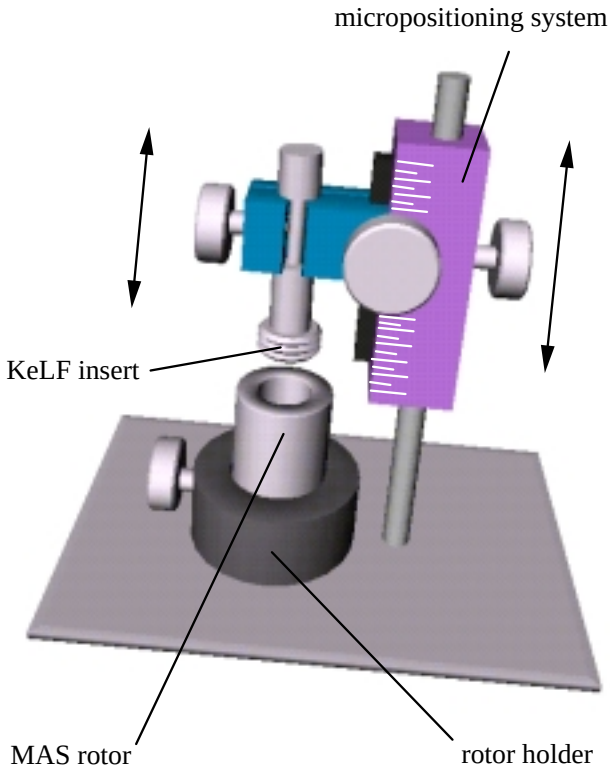

Figure A.4: Once the disks are transferred into the rotor, an insert has to be placed on top to guarantee a stable sample position under spinning conditions. The inserts were inserted and extracted using a simple single axis micropositioner system, which allowed placing the insert at a specific height in the rotor, i.e. exactly on top of the top disk. This precaution is necessary to prevent damaging the disks by applying accidentally too much pressure.

Appendix B

GAMMA Source Code for Spin-1/2 and Spin-1 MAOSS Simulations

The programme for MAS lineshape simulations of oriented systems was written in C++ by using the NMR software library GAMMA-3.5b[1] [90] and the gnu compiler gcc-2.6.3[2]. All MAS simulations were calculated by GAMMA's built-in Floquet operators as published by Baldus et al. [89]. Chemical shift anisotropy spectra of a single spin-1/2 can be calculated for various distributions, from a single crystal to the full powder. This is achieved by defining explicitly the range of the Euler angles, which define the orientation of the PAS with respect to the molecular frame (Ω_{PM}) and the orientation of the molecular frame to the rotor fixed system (Ω_{MR}). The Monte Carlo method is applied for sampling over these defined intervals and a dynamic, spherical weighting function is applied. Fig.B.1 shows a simple flow chart and the necessary input parameters. Quadrupole spectra can be obtained by setting the isotropic chemical shift to zero, the chemical shift anisotropy to the appropriate quadrupole coupling constant, η to the necessary value (usually $\eta \simeq 0$ for ^{2}H) and by choosing the symmetrizing option. The same applies for simulations of dipolar spectra of an isolated spin-1/2 pair, which can be treated as a spin-1 system. Usually, one particular orientation of the interaction tensor Ω_{PM} with respect to the molecular frame is assumed, i.e.

[1] http://gamma.magnet.fsu.edu
[2] http://www.gnu.ai.mit.edu

averaging takes place during the transformation from the molecular frame into the rotor system (see Chapter 1), but the programme allows also pre-averaging during the first transformation.

It is planned in the future to add more spins to the simulation and to explore relaxation effects on MAS sidebands.

The source code is given below.

```
/*************************************************************
*  filename: maoss.cc                                        *
*  simulates MAS spectra for I=1/2 amd I=1 nuclei in partially *
*  ordered systems                                           *
*  CSA or EFG tensor can be averaged from PAS->MF or MF_RF or *
*  over both transformations                                 *
*                                                            *
*  clemens glaubitz, oxford biochemistry                     *
*                                                            *
*  uses  GAMMA-3.5.2:                                        *
*  Floquet operators                                         *
*  [Baldus, Levante, Meier, Z. Naturforsch. 49a, 80-88(1994)] *
*************************************************************/
#include ''gamma.h''
#include <stdlib.h>
#include <math.h>
main (){
// declare symbols
// Set up a 1 spin system called 'A'
    spin_system A(1);
// vector of the magnetic field along z
    coord B(0,0,1);
// CSA: spin tensor
    spin_T TTS = T_CS2(A,0,B);
// CSA: space tensor in LAB system
    space_T CS;
// CSA: space tensor molecular frame
    space_T CS_mf;
// Spectral range
    double minFreq, maxFreq;
// euler angle PAS->MF
    double alpha_pm, beta_pm, gamma_pm;
    double alpha_pm_min,alpha_pm_max;
    double beta_pm_min,beta_pm_max;
    double gamma_pm_min,gamma_pm_max;
// euler angle MF->RF
    double alpha_mr, beta_mr, gamma_mr;
    double alpha_mr_min,alpha_mr_max;
    double beta_mr_min,beta_mr_max;
    double gamma_mr_min,gamma_mr_max;
    double beta_pr;
// Output filename
     String outFileName;
// chemical shift tensor
     double sig, delta, eta;
```

Figure B.1: Flow chart and input files for the programm MAOSS, which simulates MAS lineshapes for oriented systems. One input file containing all parameters is required. The fourier transformed data are stored in an ascii file in XMGR format. All parameters are stored in a seperate file. For details see explanation in text.

```
     double sixx,siyy,sizz;
// Steps in powder loop
     int steps_pm, steps_mr;
// MAS rotation frequency
     double omegar;
     int lb, proc, norm, sym, N;
// read parameter from stream
        cin>>outFileName;
        cin>>N;
        cin>>proc;
        cin>>minFreq;
        cin>>maxFreq;
        cin>>omegar;
        cin>>sig;
        cin>>delta;
        cin>>eta;
        cin>>alpha_pm_min;
        cin>>alpha_pm_max;
        cin>>beta_pm_min;
        cin>>beta_pm_max;
        cin>>gamma_pm_min;
        cin>>gamma_pm_max;
        cin>>steps_pm;
        cin>>alpha_mr_min;
        cin>>alpha_mr_max;
        cin>>beta_mr_min;
        cin>> beta_mr_max;
        cin>>gamma_mr_min;
        cin>>gamma_mr_max;
        cin>>steps_mr;
        cin>>lb;
        cin>>norm;
        cin>>sym;
// define output streams for data and parameter files
     ofstream os (outFileName+''.dat'');
     ofstream ps (outFileName+''.par'');
// define CSA tensor
     sixx = sig-delta*(1+eta)/2;
     siyy = delta*(eta-1)/2+sig;
     sizz = delta+sig;
     matrix s1(3,3);
     s1.put_h(sixx, 0, 0);
     s1.put_h(0., 0, 1);
     s1.put_h(  0.,  0, 2);
     s1.put_h(siyy, 1, 1);
     s1.put_h( 0., 1, 2);
     s1.put_h(sizz, 2, 2);
     space_T CS_pas(A2(s1));
// set up density matrix
     gen_op sigma1;
// set up a detection operator
     gen_op detect=Fm(A);
// prepare spin system (sigma0)
     sigma1=sigma_eq(A);
     sigma1=Iypuls(A,sigma1,90.);
```

```
// setup Floquet density matrix
     floq_op fsigma   ( N, A.HS(), omegar);
     fsigma.put_block ( sigma1, 0, 0);
// set data blocks for spectra
     int NP=4096;
     block_1D spect(NP);
     block_1D specsum(NP);
     block_1D specsum1(NP);
     block_1D specsum2(NP);
// Fourier expansion of the Hamiltonian
     gen_op H_0, H_1, H_2;
// Time and orientation independent component
// of the Hamiltonian
     H_0 = CS_pas.component(0,0) * TTS.component(0,0);
for(int b=1;b<=steps_mr;b++)
{ //<----start MF->RF loop
  // calculate random values for OMEGA_mr within predefined range
     alpha_mr = random() * (alpha_mr_max - alpha_mr_min ) /
                (pow(2.0,31.0)-1.0) + alpha_mr_min ;
     beta_mr  = random() * (beta_mr_max  - beta_mr_min  ) /
                (pow(2.0,31.0)-1.0) + beta_mr_min  ;
     gamma_mr = random() * (gamma_mr_max - gamma_mr_min ) /
                (pow(2.0,31.0)-1.0) + gamma_mr_min ;
for(int a=1;a<=steps_pm;a++)
{ //<----start PAS->MF loop
  // calculate random values for OMEGA_pm within predefined range
     alpha_pm =  random() * (alpha_pm_max - alpha_pm_min) /
                 (pow(2.0,31.0)-1.0) + alpha_pm_min ;
     beta_pm  =  random() * (beta_pm_max  - beta_pm_min ) /
                 (pow(2.0,31.0)-1.0) + beta_pm_min  ;
     gamma_pm =  random() * (gamma_pm_max - gamma_pm_min) /
                 (pow(2.0,31.0)-1.0) + gamma_pm_min ;
  // transform CS from PAS->MF->RF
     CS_mf = CS_pas.rotate( alpha_pm, beta_pm, gamma_pm);
     CS =  CS_mf.rotate( alpha_mr, beta_mr, gamma_mr);
  // Calculate the space+time dependent parts of the Hamiltonian
     H_1 =  CS.component(2,1)  * TTS.component(2,0);
     H_1 = (1/sqrt(3.))*H_1;
     H_2 =  CS.component(2,2)  * TTS.component(2,0);
     H_2 = (1/sqrt(6.))*H_2;
  // define the Floquet Hamiltonian
  // Hamilton Floquet Matrix
     floq_op HAMFLOQ (N,A.HS(),omegar);
     HAMFLOQ.put_sdiag(adjoint(H_2),-2); // side diagonal # -2
     HAMFLOQ.put_sdiag(adjoint(H_1),-1); // side diagonal # -1
     HAMFLOQ.put_sdiag(H_0,0);           // main diagonal
     HAMFLOQ.put_sdiag(H_1,1);           // side diagonal # 1
     HAMFLOQ.put_sdiag(H_2,2);           // side diagonal # 1
     HAMFLOQ.add_omega();                // Add omegas on diagonal
  // Calculate the spectrum ('spec' for general simulations)
     if(proc==1)
```

```
                    {
     spec_maspowder
     (fsigma, detect, HAMFLOQ, minFreq, maxFreq, NP, spect);
                    }
     else
                    {
     spec
     (fsigma, detect, HAMFLOQ, minFreq, maxFreq, NP, spect);
                    }
     specsum += spect;
} //<----end PAS->MF loop
  // spherical weight on beta_mr
     if(steps_mr==1 && abs(beta_mr_min-beta_mr_max)==0.0)
                    {
     specsum *= 1.0;
                    }
     else
                    {
     specsum *=
     sin(abs((0.5*(beta_mr_min+beta_mr_max)-beta_mr)*PI/180.));
                    }
     specsum1+=specsum;
} //<----end MF->RF loop
// fourier transformation and exp.linebroadening
   specsum1 =IFFT (specsum1);
   exponential_multiply (specsum1,-lb);
   specsum1 =FFT (specsum1);
// symmetrise spectrum if required
   if(sym==1)
                    {
   for(int jjj=0;jjj<NP;jjj++)
                    {
   specsum2(jjj)=specsum1(jjj)+specsum1(NP-1-jjj);
                    }
   specsum1=specsum2;
                    }
// normalise spectrum if required
   double maxy=0.0;
   double miny=1000000000.0;
   if(norm==1){
   for(int l =0;l<4096;l++)
                    {
   if(Re(specsum1(l)) > maxy) maxy=Re(specsum1(l));
   if(Re(specsum1(l)) < miny) miny=Re(specsum1(l));
                    }
   for(int mm=0;mm<NP;mm++)
                    {
   specsum1(mm)=specsum1(mm)-miny;
                    }
   specsum1=specsum1/(maxy-miny) ;
                    }
// write out data to file
   for (int i =0;i<NP;i++)
   os<<(maxFreq-minFreq)*(i-NP/2)/NP
     <<'' ''
     <<Re(specsum1(i))
```

```
      << '' ''
      <<Im(specsum1(i))
      <<''\n'';
}
```

Appendix C

RR-FIT: Fitting Rotational Resonance Data with MINUIT

RR_FIT is a modified version of Malcolm Levitt's CC2 software[1] for simulating magnetisation exchange trajectories under rotational resonance conditions. In the ideal case of distance determination, only one parameter - the dipolar coupling - would have to be optimized, but since T_2^{ZQ} is difficult to determine, usually a restricted two parameter fit is necessary [30]. The magnetisation exchange rate at higher orders of resonance depends additionally on the orientation Ω_{PM} of CSA and dipolar coupling tensors with respect to the molecular frame. By fixing the parameters for distance and T_2^{ZQ}, information of orientations of tensors with respect to each other can be obtained by optimizing Ω_{PM}. Additionally, rotational resonance on labelled proteins in oriented membranes would allow to determine the orientation of the dipolar coupling tensor with respect to the membrane fixed coordinate system. These tasks require a reliable multi-parameter fitting procedure, which is supplied by CERN's MINUIT F77 library[2]. MINUIT functions allow non-linear minimisation of up to 150 parameters. Fig.C.1 shows a simplified flow chart and necessary input parameters. The file "experimental.dat" contains the normalised experimental exchange curve as standard ASCII, while "parameter.dat" holds parameters such as spinning speed, number of crystal orientations, etc., i.e. parameters which will not be subject to optimization.. With

[1] http://www.fos.su.se/~mhl/science/software.html

[2] CERN Program Library Office, CERN-CN Division, CH-1211 Geneva, Switzerland, cernlib@cernvm.cern.ch

the parameter "proc", the user can specify, whether an on-resonance approximation (11), a near-resonance solution (12) or an exact simulation (13) should be used for calculating magnetisation exchange (see also Appendix D). All fitting and MINUIT control data are stored in "alpha.dat". Each or any combination of parameters 1-18 can be simultaneously fitted by deleting their number in the "fix-line". This line is followed by MINUIT commands. Data on lines 1-18 have to be defined by the expected value, followed by accuracy and by the interval in which the parameter space should be searched. MINUIT actually minimizes a function FCN, which was chosen to be the standard deviation χ^2:

$$\chi^2 = \sum_{i=1}^{n} \left(\frac{e_i - f(x_i, \alpha)}{\sigma_i} \right)^2 \tag{C.1}$$

where α is the vector of free parameters being fitted, and the σ_i are the uncertainties in the individual measurements e_i.

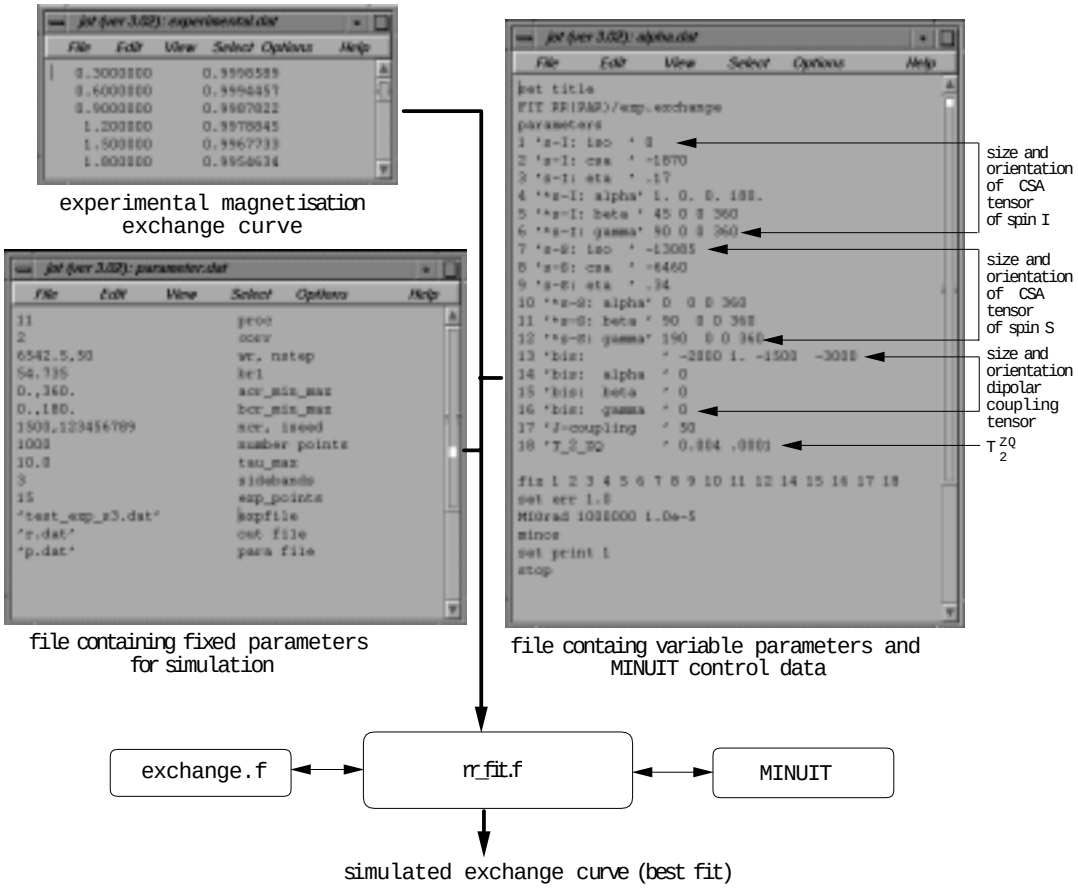

Figure C.1: Flow chart and input files for multi-parameter fitting of RR exchange curves. Each or any combination of the 18 parameters in file "alpha.dat" can be optimized by deleting their number in the "fix-line".

Appendix D

The Simulation of Magnetisation Exchange Near the Resonance Condition: An Analytical Solution

Abstract

An analytical expression for calculating magnetisation exchange curves close to the rotational resonance condition is presented. This term allows fast simulations of magnetisation exchange trajectories and is potentially useful for treating data arising from inhomogeneously broadened systems and near resonance phenomena.

Introduction

The problem of recoupling in Magic Angle Sample spinning NMR has received much attention in the last years [31],[35],[199],[200]. These methods have to be used to reintroduce the dipolar couplings back into the spectrum, which offers the possibility for structural studies in systems of unrestricted molecular weight. One of the simplest methods is rotational resonance [29],[201],[152]. The dipolar coupling within an isolated spin-1/2 pair is reintroduced under MAS conditions, when the chemical shift frequency difference is equal to an integer multiple of the sample spinning speed. In case of ^{13}C labels, distances up to 0.5 and 0.6 nm can be measured, which has been used for complex problems, such as ^{13}C labelled

ligands bound to membrane proteins (e.g. bacteriorhodopsin, rhodopsin, gastric proton pump [202],[154],[52],[158]). In addition, information about the orientation of both CSA tensors with respect to each other and to the dipolar coupling tensor can be extracted by studying higher orders of resonance [161],[162]. Although experimentally relatively simple, the analysis of lineshapes or Zeeman magnetisation exchange trajectories obtained under rotational resonance condition requires some care and multi-dimensional parameter fits are necessary in some cases, although the rotational resonance phenomenon is theoretically well described and understood [30, 203, 204]. A specific problem occurred by studying labelled peptides, which were found to exhibit inhomogeneous linebroadening in the solid state [162],[155],[172],[205],[156],[171]. Recently, the application of rotational resonance to inhomogeneously broadened systems has been discussed by Heller et al. [172] and special attention has been paid to error analysis and parameter correlation. The presented protocol for data analysis was based on Floquet theory and is rather time consuming. In the following, we present an analytical expression for the magnetisation exchange trajectory which allows calculations on and near the rotational resonance condition and which can be easily incorporated into standard programming languages. In addition, we evaluate our theoretical findings for an interesting case of magnetisation exchange near the rotational resonance condition.

Theory

A detailed theoretical description for rotational resonance has been presented [30], which allows to focus here as much as possible on special aspects of Zeeman magnetisation exchange (see Chapter 5).

At the start of the exchange period τ , the spin pair is prepared in a uniform state of Zeeman polarisation, corresponding to a density operator $\boldsymbol{\rho}^{(23)}(0)$, which describes z-polarisation in the {|2>,|3>}subspace.

$$\boldsymbol{\rho}^{(23)}(0) \sim \frac{1}{2} < I_Z - S_Z > (0) = I_z^{(23)} \tag{D.1}$$

During the mixing time τ, the state vector proceeds to nutate about the fictitious field given in Eqn.5.9. The spin density operator may be described as a vector in the space of spin operators ($I_X^{(23)}$,$I_Y^{(23)}$,$I_Z^{(23)}$) which follows the Bloch equation

$$\frac{d}{dt}\boldsymbol{\rho}^{(23)}(t) = \mathcal{W}^{(23)}(t)\boldsymbol{\rho}^{(23)}(t) \tag{D.2}$$

$$\mathcal{W}^{(23)}(t) = \begin{pmatrix} -r & -\omega_\Delta(t) & 0 \\ \omega_\Delta(t) & -r & -\omega_B(t) \\ 0 & \omega_B(t) & 0 \end{pmatrix} \tag{D.3}$$

where r=$1/T_2^{ZQ}$.The time dependence of $\omega_\Delta(t)$ and $\omega_B(t)$ can be predicted from orientation and magnitude of shielding and dipolar coupling tensors. Even further simplification can be achieved by considering, that only Fouriercomponents of the non-secular dipolar interactions $|\widetilde{\omega}_B^{(n)}|$ contribute to the rotational resonance effect in a suitable ferefence frame. $\mathcal{W}^{(23)}(t)$ becomes time independent:

$$\tilde{\mathcal{W}}^{(23)} = \begin{pmatrix} -r & -\Delta\omega & 0 \\ \Delta\omega & -r & -|\tilde{\omega}_B^{(n)}| \\ 0 & |\tilde{\omega}_B^{(n)}| & 0 \end{pmatrix} \tag{D.4}$$

where the resonance offset describes the deviation from the rotational resonance condition and is given by $\Delta\omega = (\omega_\Delta^{iso} - n\omega_r)$. The chmical shift difference is given as ω_Δ^{iso} and toe MAS spinning speed is ω_r. MAS spinning speed. At this point, further simplifications are possible by assuming exact rotational resonance, i.e. $\Delta\omega = 0$, which has been shown in [30], but here a more general situation is considered by continuing using expression D.4.

Integrating the Bloch equation in the $\{2,3\}$ subspace over one rotor period τ_R yields a formal solution for $\boldsymbol{\rho}^{(23)}(t)$:

$$\begin{aligned} \boldsymbol{\rho}^{(23)}(n\tau_R) &= \widehat{\widehat{\mathcal{L}}}(n\tau_R, 0)\boldsymbol{\rho}^{(23)}(0) \\ \widehat{\widehat{\mathcal{L}}}(n\tau_R, 0) &= \hat{T}e^{\tilde{\mathcal{W}}^{(23)}n\tau_R} \end{aligned} \tag{D.5}$$

where $\widehat{T}$ is the Dyson time ordering operator. Using simple matrix algebra, $\widehat{\widehat{\mathcal{L}}}(\tau_R, 0)$ can be written as:

$$\widehat{\widehat{\mathcal{L}}}(n\tau_R, 0) \simeq X_W e^{L_W n\tau_R} {X_W}^{-1} \tag{D.6}$$

where L_W represents the matrix of Eigenvalues

$$L_W = \begin{pmatrix} \lambda_1 & 0 & 0 \\ 0 & \lambda_2 & 0 \\ 0 & 0 & \lambda_3 \end{pmatrix} \tag{D.7}$$

and X_W the matrix of Eigenvectors of $\tilde{\mathcal{W}}^{(23)}$.

$$X_W = \left(\begin{pmatrix} x_{11} \\ x_{21} \\ x_{31} \end{pmatrix} \begin{pmatrix} x_{12} \\ x_{22} \\ x_{32} \end{pmatrix} \begin{pmatrix} x_{13} \\ x_{23} \\ x_{33} \end{pmatrix} \right) \tag{D.8}$$

$\tilde{\mathcal{W}}^{(23)}$has been diagonalised analytically by using the following substitutions and supported by the computer algebra software Mathematica 2.0 (Wolfram Research):

$$\begin{aligned} X &= 3|\tilde{w}_B^{(n)}|^2 - r^2 + 3\Delta\omega^2 \\ Y &= 2r^3 - 9|\tilde{w}_B^{(n)}|^2 r + 18 r \Delta\omega^2 \\ Z &= (Y + \sqrt{4X^3 + Y^2})^{1/3} \end{aligned} \tag{D.9}$$

We obtained for the Eigenvalues and Eigenvectors the following expressions:

$$\begin{aligned} \lambda_1 &= -\frac{2}{3}r - \frac{\sqrt[3]{2}}{3}\left(\frac{X}{Z} - \frac{Z}{\sqrt[3]{4}}\right) \\ \lambda_2 &= -\frac{2}{3}r + \frac{1}{3\sqrt[3]{4}}\left(\frac{X}{Z} - \frac{Z}{\sqrt[3]{4}}\right) + \frac{i}{\sqrt{3}\sqrt[3]{4}}\left(\frac{X}{Z} + \frac{Z}{\sqrt[3]{4}}\right) \\ \lambda_3 &= -\frac{2}{3}r + \frac{1}{3\sqrt[3]{4}}\left(\frac{X}{Z} - \frac{Z}{\sqrt[3]{4}}\right) - \frac{i}{\sqrt{3}\sqrt[3]{4}}\left(\frac{X}{Z} + \frac{Z}{\sqrt[3]{4}}\right) \end{aligned} \tag{D.10}$$

$$\vec{x}_1 = \begin{pmatrix} x_{11} \\ x_{21} \\ x_{31} \end{pmatrix} = \begin{pmatrix} -\frac{\Delta\omega(\sqrt[3]{4}(Z^2 - \sqrt[3]{4}X) - 4rZ)}{|\tilde{w}_B^{(n)}|(\sqrt[3]{4}(Z^2 - \sqrt[3]{4}X) + 2rZ)} \\ \frac{\sqrt[3]{4}(Z^2 - \sqrt[3]{4}X) - 4rZ}{6|\tilde{w}_B^{(n)}|Z} \\ 1 \end{pmatrix} \tag{D.11}$$

$$\vec{x}_2 = \begin{pmatrix} x_{12} \\ x_{22} \\ x_{32} \end{pmatrix} = \begin{pmatrix} -\frac{\Delta\omega(\sqrt[3]{4}(Z^2-\sqrt[3]{4}X)+8rZ-i\sqrt[3]{4}\sqrt{3}(Z^2+\sqrt[3]{4}X))}{|\tilde{w}_B^{(n)}|(\sqrt[3]{4}(Z^2-\sqrt[3]{4}X)-4rZ-i\sqrt[3]{4}\sqrt{3}(Z^2+\sqrt[3]{4}X))} \\ -\frac{(\sqrt[3]{4}(Z^2-\sqrt[3]{4}X)+8rZ-i\sqrt[3]{4}\sqrt{3}(Z^2+\sqrt[3]{4}X))}{12|\tilde{w}_B^{(n)}|Z} \\ 1 \end{pmatrix} \tag{D.12}$$

$$\vec{x}_3 = \begin{pmatrix} x_{13} \\ x_{23} \\ x_{33} \end{pmatrix} = \begin{pmatrix} -\frac{\Delta\omega(\sqrt[3]{4}(Z^2-\sqrt[3]{4}X)+8rZ+i\sqrt[3]{4}\sqrt{3}(Z^2+\sqrt[3]{4}X))}{|\tilde{w}_B^{(n)}|(\sqrt[3]{4}(Z^2-\sqrt[3]{4}X)-4rZ+i\sqrt[3]{4}\sqrt{3}(z^2+\sqrt[3]{4}X))} \\ -\frac{\sqrt[3]{4}(Z^2-\sqrt[3]{4}X)+8rZ+i\sqrt[3]{4}\sqrt{3}(Z^2+\sqrt[3]{4}X)}{12|\tilde{w}_B^{(n)}|Z} \\ 1 \end{pmatrix} \tag{D.13}$$

Substituting expressions (10) - (13) into (5) and (6) gives an analytical expression for the magnetization exchange in a single crystal:

$$\begin{aligned} \rho_Z^{(23)}(n \times \tau_R) \;=\; & \\ & e^{\lambda_1 t}\frac{(-x_{13}x_{22}+x_{12}x_{23})x_{31}}{(-x_{13}x_{22}x_{31}+x_{12}x_{23}x_{31}+x_{13}x_{21}x_{32} \\ & \qquad -x_{11}x_{23}x_{32}-x_{12}x_{21}x_{33}+x_{11}x_{22}x_{33})} \\ + \;& e^{\lambda_2 t}\frac{(x_{13}x_{21}-x_{11}x_{23})x_{32}}{(-x_{13}x_{22}x_{31}+x_{12}x_{23}x_{31}+x_{13}x_{21}x_{32} \\ & \qquad -x_{11}x_{23}x_{32}-x_{12}x_{21}x_{33}+x_{11}x_{22}x_{33})} \\ + \;& e^{\lambda_3 t}\frac{(-x_{12}x_{21}+x_{11}x_{22})x_{33}}{(-x_{13}x_{22}x_{31}+x_{12}x_{23}x_{31}+x_{13}x_{21}x_{32} \\ & \qquad -x_{11}x_{23}x_{32}-x_{12}x_{21}x_{33}+x_{11}x_{22}x_{33}))} \end{aligned} \tag{D.14}$$

This analytical expression for the difference magnetisation time course allows much faster computation than diagonalising the matrix D.3 for each time step and crystal orientation. These simulations can be easily done by performing a powder average over Eqn. D.14. For that purpose, the software obtained from M.Levitt was modified and combined with the non-linear fitting package MINUIT (CERN). A multi-dimensional space of any combination of spin parameters can

be searched for the best fit within a reasonable time. Usually, fittings are performed over the internuclear distance and T_2^{ZQ}, since the latter parameter is difficult to measure. Additionally, various tensor orientations and chemical shift distributions can be included as well [161],[172],[162]. This approach appears to be about four times faster than the numerical simulation. Two experimental applications are discussed below.

Experimental

All spectra were recorded at 100.63 MHz for ^{13}C and 400.13 MHz for ^{1}H using a Bruker MSL 400 spectrometer and double resonance 4 mm MAS probe (Bruker, Germany). Typical $\pi/2$ pulse duration were 4 μs. Rotational resonance experiments were performed using a DANTE pulse sequence and RAMP cross-polarisation [159]. The spinning speed was controlled within a range of ± 1 Hz using a home built spinning speed synchronizer connected between the pneumatic Bruker MAS unit and the probe.

Doubly labelled acetylcholine $^{13}\mathbf{C}H_3COO(CH_2)_2N(^{13}CH_3CH_3CH_3)$ (Fig.3), kindly provided by Phil Williamson, Biomembrane Structure Unit, Oxford University, has been synthesized and crystallised as described elsewhere [53]. The chemical shift tensors for both labelled sites were characterised from static and low speed MAS spectra using the Hertzfeld-Berger algorithm and the software Speedyfit [22, 206]. The MAS resonance lines were rather narrow, which shows, that only one molecular conformation exists in the polycrystalline sample. The sample has been diluted in unlabelled material at a ratio of 1:6 in order to suppress intermolecular interaction.

Magnetisation exchange was measured inverting the single quantum coherence arising from the labelled N-Methyl group using a DANTE pulse train [160]. To avoid spectrometer artefacts, all 120 mixing times were randomly mixed and 4 dummy scans were allowed before acquiring each spectrum using 16 scans [172],[171]. The contact time for cross polarisation was 1 ms and a 3 s recycle delay was used.

Computer simulation were performed on a SGI INDI 4600 workstation.

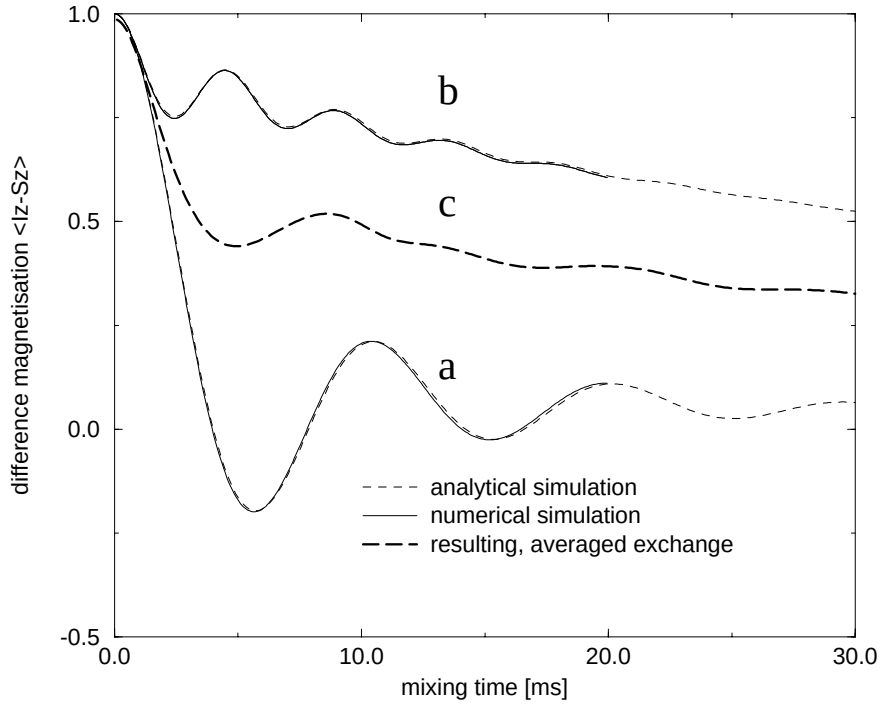

Figure D.1: Comparison between simulation using equation (14) and numerical diagonalisations for each time step and crystal orientations of matrix (3). A parameter set corresponding to labels in the C=O and Cα position in a peptide backbone was used, with J-coupling set to zero, T_2^{ZQ}= 6.00 ms and a dipolar coupling of $b_{IS}/2\pi$= - 300Hz. The spinning speed of ω_r=10500Hz would satisfy the n=1 resonance condition, i.e. matches the chemical shift difference exactly **(a)**. Changing the isotropic chemical shift for both sites by 100Hz results in a resonance offset of 200Hz **(b)**. Simulating inhomogeneous linebroadening (see Fig.D.2) by stepping through a certain chemical shift dispersion with a Lorentz weighting function gives an averaged exchange curve **(c)**. Numerical and analytical simulations are nearly indistinguishable in this example.

Results and Discussion

Inhomogeneous Linebroadening - Simulations

Fig.D.1 compares simulations of powder averaged magnetisation exchange using the analytical expression with numerical matrix diagonalisations. The results are almost indistinguishable. A parameter set corresponding to a C=O and a Cα CSA tensor found in peptide backbones has been used. Curve (a) corresponds to the exact "n=1- on - resonance" situation, at which the spinning speed matches the chemical shift difference, where curve (b) was calculated for the same spinning speed, but larger chemical shift difference, which results in a resonance offset of 200 Hz. An experimental situation in which a chemical shift distribution for both spin sites has to be taken into account would arise in cases of inhomogeneous linebroadening, as illustrated in Fig.D.2: Only a few spin pairs in the ensemble would be exact on rotational resonance, while others would exchange magnetisation at a different rate. The need to incorporate these "near resonance effects" into the data analysis of rotational resonance has been pointed out in a number of papers about NMR studies of solid peptides [171, 205, 172, 162]. Peersen et al. [171] have experimentally shown, that the initial exchange rate around the resonance condition is weighted by a Lorentz function. Trajectory (c) shown in Fig.D.1 is actually the averaged exchange curve (the one which would be observed) obtained by stepping through a chemical shift distribution of 200 Hz weighted by a Lorentzian lineshape. A protocol for data analysis is discussed in detail by Heller et al. [172] but using the analytical solution presented here allows much faster computation.

Magnetisation exchange near the resonance condition

Acetylcholine, which binds as a ligand to the acetylcholine receptor, has been synthesised and ^{13}C labelled (see Fig. D.3) for rotational resonance experiments in the native membrane. Here, we present some data on its crystalline form, acetylcholine perchlorate, which were originally planned to be useful in calibrating the experiments in the membrane, but show interesting off-resonance effects.

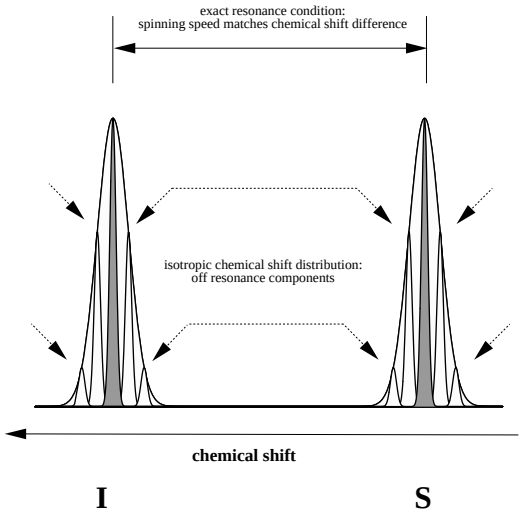

Figure D.2: The effect of inhomogeneous linebroadening has to be taken into account by analysing magnetisation exchange under rotational resonance conditions: The exact resonance condition is only fulfilled for spin pairs with chemical shifts matching the spinning speed, but spin pairs within a certain range of chemical shift distribution contribute to the exchange as well (see Fig.D.1) .

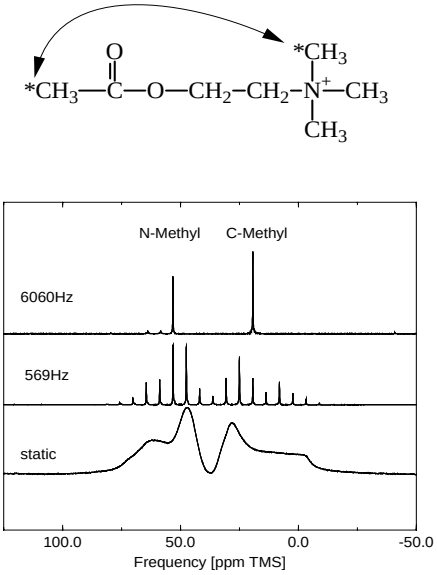

Figure D.3: Structural formula of doubly ^{13}C labelled acetylcholine. Static and CP-MAS spectra at different spinning speeds are shown below. Static and low speed spectra were used to determine the size of the chemical shift tensors.

Fig.D.3 shows static, low speed and fast spinning MAS spectra. The chemical shift anisotropies do not overlap, which is important for rotational resonance data analysis [30], but are of similar size to the chemical shift difference. All MAS resonance lines are rather narrow ($\Delta\nu_{1/2}$=18Hz), i.e. one single crystal conformation can be assumed. Both ^{13}C labels are placed in highly dynamic CH_3 groups, but since their correlation times are much faster, than the ^{13}C-NMR and magnetisation exchange timescales (^{2}H-NMR studies, unpublished results[1]), only averaged CSA tensors were measured and used for simulations. An experimental exchange curve for n=1, corresponding to a spinning speed of ω_r=3416 Hz, is shown in Fig.D.4a. The natural background signal was subtracted and the average of the first five points was used to normalise the data to 1.0. The best fit ($\chi^2 = 0.9 \times 10^{-4}$) is plotted over the data, which was obtained by optimizing the parameter T_2^{ZQ} and $b_{IS}/2\pi$. The fitted dipolar coupling of $b_{IS}/2\pi = -85 \pm 7$ Hz (0.447±0.012 nm) corresponds well to the estimated distance of 0.44 nm from

[1]P. Williamson, Oxford University, Biomembrane Structure Unit

the crystal structure obtained by X-ray diffraction [207] and $T_2^{ZQ} = 10.5 \pm 4$ ms agrees with the estimated lower value of 8.0 ms from the linewidth of both sites obtained far away from the resonance point ($T_2^{ZQ} \geq 1/(\pi(\Delta\nu_{1/2}^I + \Delta\nu_{1/2}^S))$)[30]. The unrealistic high error for T_2^{ZQ} can be explained by the relatively high correlation of both parameters ($\rho(b_{IS}/2\pi, T_2^{ZQ}) = 0.89$). The minimum predicted by the simulation at about 25 ms could not be detected experimentally. However, the magnetisation exchange curve recorded 100 Hz above the resonance spinning speed (ω_r=3516Hz) features distinct oscillations. This fact is particularly interesting, since the occurrence of oscillations can simplify the data analysis remarkably: The periodicity is directly proportional to the dipolar coupling [30], i.e. complicated multi-dimensional parameter fits would not be necessary. This near-resonance curve was simulated using Eqn.D.14 with the parameters obtained from fitting the on-resonance data. The result is shown in Fig.4b: While there is a difference in the decay rate between theory and experiment, the oscillations are well reproduced ($\chi^2 = 7.3 \times 10^{-2}$). There are various reasons for the slight discrepancy in the decay rate: Only Fourier components of the non-secular dipolar interactions where considered by deriving equation (14). However, the chemical shift difference between both labelled sites in acetylcholine is of the size as their chemical shift anisotropy, which might limit the general validity of the assumption made above. Additionally, spin diffusion and intermolecular effects could contribute as well, which are not included in the simulation.

The increase in periodicity in the off–resonance curve, can be picturized by the rotations of the pseudo magnetisation vector $\boldsymbol{\rho}^{(23)}$ about the fictitious field, which is tilted off-resonance, so that the oscillation frequency increases, but the amplitude decreases [30], i.e. the periodicity is governed to a certain extent by the resonance offset in addition to the dipolar coupling (periodicity is proportional to $\sqrt{\Delta\omega^2 + \left|\widetilde{\omega}_B^{(n)}\right|^2}$). Fig.D.5 illustrates the effect various dipolar couplings would have to the oscillations found in the 100Hz-off-resonance curve in acetylcholine. While T_2^{ZQ} does not change the periodicity (dashed lines around curve (a) in Fig.5), the periodicity slightly increases by increasing the dipolar coupling from -85Hz (a) to -185Hz (b) and -285Hz (c). This means for the data analysis and

distance determination, that the zero quantum relaxation time T_2^{ZQ}, which is difficult to measure, is replaced as parameter by the resonance offset, which is determined by the experimental setup. The dipolar coupling $b_{IS}/2\pi$ would be the only free parameter and is only determined by the periodicity. However, at least in the case presented here, the contribution of the dipolar coupling to the oscillations is relatively small compared to the resonance offset, which would require an extremely good data quality to measure the location of minima and maxima precisely..

Conclusions

We presented an analytical expression to calculate magnetisation exchange curves near the rotational resonance condition. Using this expression, the analysis of exchange trajectories requires about four times less computing time compared to matrix diagonalisations for each time step. Especially in the case of inhomogeneously broadened systems, the effect of a chemical shift distribution and near resonance contributions has to be taken into account as demonstrated by Heller et al. [172] and can be simplified using the solution presented here. In addition, we have shown for the labelled ligand acetylcholine, that in some cases the increased periodicity of magnetisation exchange trajectories under near resonance conditions can be utilised for distance measurements without the requirement of undergoing complicated multi-parameter fits.

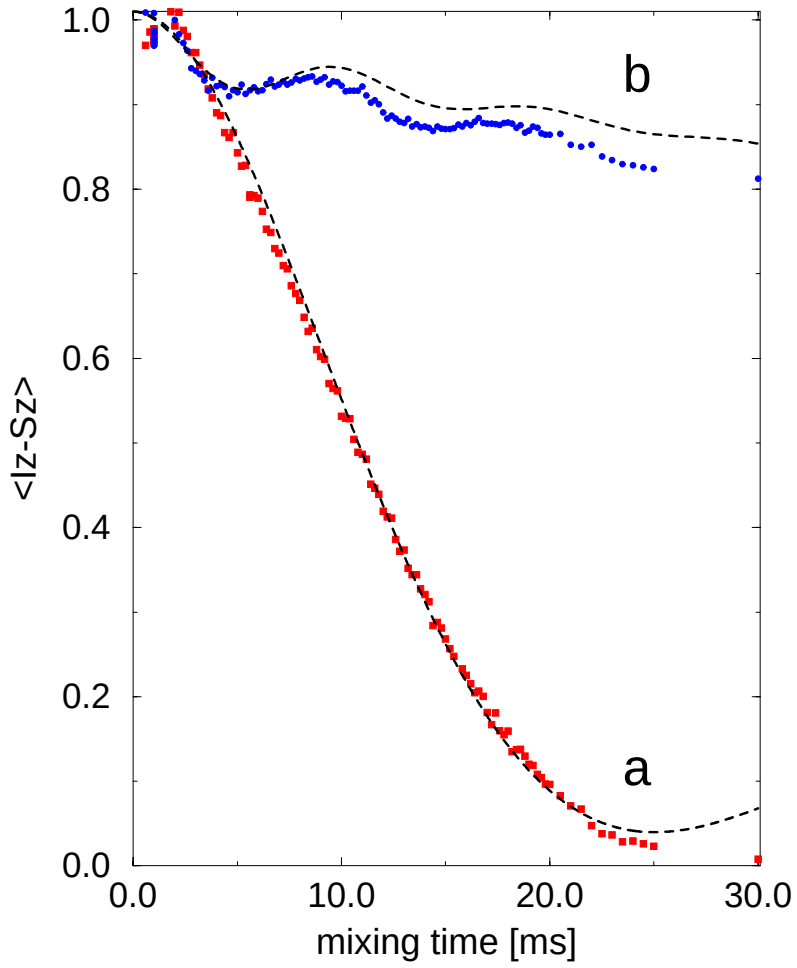

Figure D.4: Experimental and simulated on- and near resonance magnetisation exchange trajectories (n=1) for acetylcholine. For n=1 (ω_r=3416 Hz), a two dimensional parameter space (dipolar coupling $b_{IS}/2\pi$, T_2^{ZQ}) was searched for the best fit which is plotted over the experimental data **(a)**. The same parameter set was used to simulate the exchange curve obtained at ω_r=3516 Hz **(b)**.

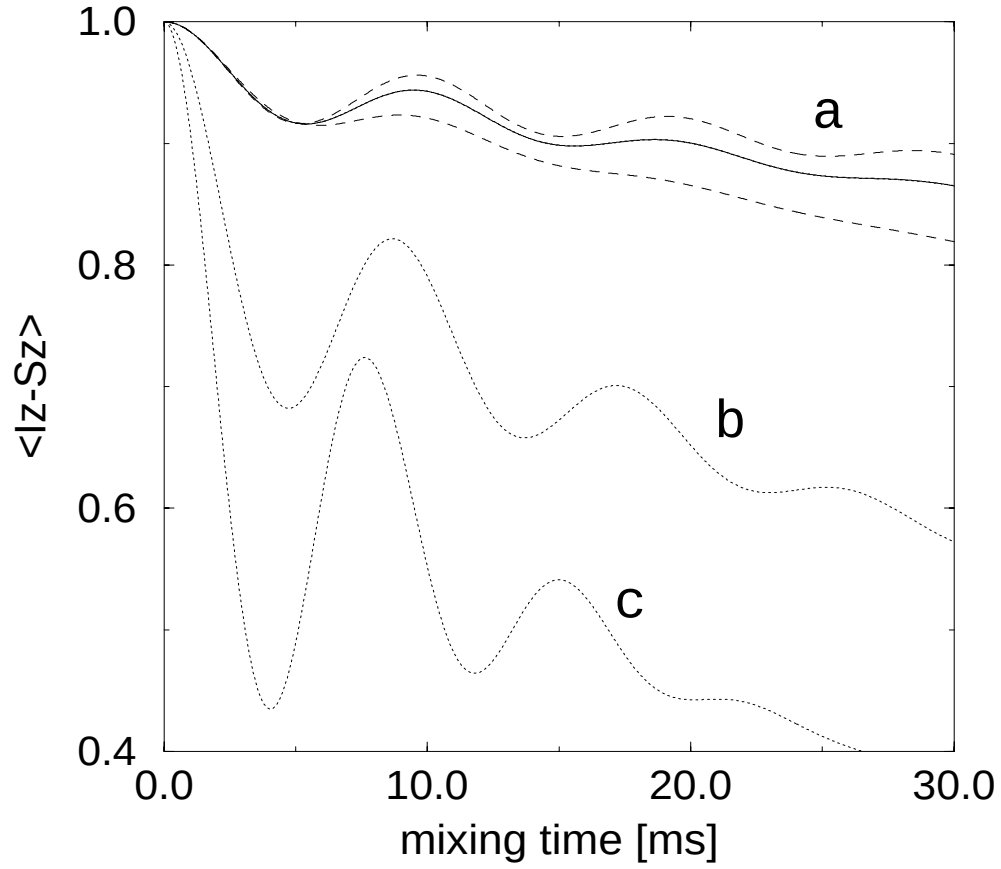

Figure D.5: The effect of T_2^{ZQ} and dipolar coupling to the periodicity of near resonance magnetisation exchange trajectories. The observed oscillations are not effected by T_2^{ZQ} **(a)**, but by the dipolar coupling as shown for $b_{IS}/2\pi$ =85Hz **(a)**, $b_{IS}/2\pi$ =185Hz **(b)** and $b_{IS}/2\pi$ =285Hz **(c)**. The resonance offset is in all cases 100 Hz, all parameters are equivalent to the simulation shown in Fig.D.4.